

EVALUATION OF HYBRID SELF-ASSEMBLED LIQUID
CRYSTAL SYSTEMS FOR POTENTIAL APPLICATION IN
SOLAR THERMOELECTRIC GENERATOR

SHAHRIR RAZEY BIN SAHAMIR

FACULTY OF ENGINEERING
UNIVERSITY OF MALAYA
KUALA LUMPUR

2018

**EVALUATION OF HYBRID SELF-ASSEMBLED
LIQUID CRYSTAL SYSTEMS FOR POTENTIAL
APPLICATION IN SOLAR THERMOELECTRIC
GENERATOR**

SHHRIR RAZEY BIN SAHAMIR

**THESIS SUBMITTED IN FULFILMENT OF THE
REQUIREMENTS FOR THE DEGREE OF DOCTOR OF
PHILOSOPHY**

**FACULTY OF ENGINEERING
UNIVERSITY OF MALAYA
KUALA LUMPUR**

2018

UNIVERSITY OF MALAYA
ORIGINAL LITERARY WORK DECLARATION

Name of Candidate: Shahrir Razey Bin Sahamir

Matric No: KHA130003

Name of Degree: Doctor of Philosophy

Title of Thesis: Evaluation of Hybrid Self-Assembled Liquid Crystal Systems
for Potential Application in Solar Thermoelectric Generator

Field of Study:

I do solemnly and sincerely declare that:

- (1) I am the sole author/writer of this Work;
- (2) This Work is original;
- (3) Any use of any work in which copyright exists was done by way of fair dealing and for permitted purposes and any excerpt or extract from, or reference to or reproduction of any copyright work has been disclosed expressly and sufficiently and the title of the Work and its authorship have been acknowledged in this Work;
- (4) I do not have any actual knowledge nor do I ought reasonably to know that the making of this work constitutes an infringement of any copyright work;
- (5) I hereby assign all and every rights in the copyright to this Work to the University of Malaya ("UM"), who henceforth shall be owner of the copyright in this Work and that any reproduction or use in any form or by any means whatsoever is prohibited without the written consent of UM having been first had and obtained;
- (6) I am fully aware that if in the course of making this Work I have infringed any copyright whether intentionally or otherwise, I may be subject to legal action or any other action as may be determined by UM.

Candidate's Signature

Date:

Subscribed and solemnly declared before,

Witness's Signature

Date:

Name:

Designation:

**EVALUATION OF HYBRID SELF-ASSEMBLED LIQUID CRYSTAL
SYSTEMS FOR POTENTIAL APPLICATION IN SOLAR
THERMOELECTRIC GENERATOR**

ABSTRACT

This research is motivated by the need to develop materials for a conceptual solar thermoelectric generator (STEG) device. Investigation on the key material parameters for STEG i.e. electrical conductivity, Seebeck coefficient and thermal conductivity was conducted. Liquid Crystal (LC) was chosen as the candidate material due to its capability for self-assembly. This work explores the two classes of LC materials with self-assembly: (1) a hybrid mixture of Polymer Electrolyte Liquid Crystal (PELC) system consisting of polyvinyl alcohol polymer (PVA), potassium iodide (KI) salt and nematic liquid crystal 4-Cyano-4'-pentylbiphenyl (5CB); and (2) a doped Discotic Liquid Crystals (DLCs) system consisting of 2,3,6,7,10,11-hexakis(hexyloxy)triphenylene (HAT6) and aluminium trichloride (AlCl_3) salt. Tuneable thermoelectric properties of PELC were achieved with addition of different concentrations of 5CB into PVA polymer-KI electrolyte mixtures in PELC studies. It was found that the self-assembly of thermotropic LCs during transition increases the electrical conductivity and Seebeck coefficient performance in PELC system, whilst increased concentration of 5CB has reduced their thermal conductivity. In DLC studies, the HAT6 DLC which possesses a quasi-one-dimensional (1D) transport property was investigated for its electrical conductivity and optical properties in order to evaluate its potential as the active material component in STEG. The stacking of columnar discs of DLCs was found to favour its electrical conductivity as the behaviour similar to conduction in 1D nanowires was observed. The study of the structural of HAT6 and its effect on the electronic and thermal properties is investigated through Raman spectral analysis, and correlated to density functional theory (DFT) simulation. The results from Raman study indicates a high core to core correlation

in the LC columnar phase, which has a ‘memory’ like effect that extends into isotropic phase at femtosecond timescale, which is supported by the electrical conductivity measurement of DLCs, in which the electrical conductivity is enhanced in the DLC phase. DFT simulation was also carried out in order to elucidate the basic properties of HAT6 such as the band gap. An interesting outcome of this simulation is that in a freely unspecified boundary model, when used to describe the core to core stacking, results in a more flexible HAT6 molecule with a reduced band gap. Thus, this work provides an understanding of relationship between columnar order and electrical conductivity of HAT6 molecule, and potential strategy for design of DLCs in electronic applications, specifically towards development of STEGs.

Keywords: Solar thermoelectric generator (STEG), liquid crystals (LCs), discotic liquid crystals (DLCs), thermoelectric, Raman spectroscopy, density functional theory (DFT)

**PENILAIAN SISTEM-SISTEM HABLUR CECAIR TERSUSUN SENDIRI
UNTUK APLIKASI BERPOTENSI DI DALAM PENJANA KUASA SURIA-
TERMOELEKTRIK**

ABSTRAK

Motivasi kajian ini adalah untuk membangunkan bahan semikonduktor dalam keadaan pepejal untuk penjana kuasa yang berkonsepkan suria-termoelektrik (STEG). Kajian ke atas parameter-parameter yang penting bagi bahan tersebut untuk penjana kuasa STEG seperti kekonduksian elektrik, koefisien Seebeck dan kekonduksian terma telah dijalankan. Hablur cecair (LC) telah dipilih sebagai calon bahan kerana kebolehannya untuk tersusun secara sendiri. Kerja ini mengkaji dua kelas bahan hablur cecair dengan kebolehan untuk tersusun sendiri: (1) campuran hibrid polimer-elektrolit-hablur cecair (PELC) yang terdiri daripada polimer polivinil alkohol (PVA), garam kalium iodida (KI) dan hablur cecair nematik 4-siano-4'-pentilbifenil (5CB); dan (2) campuran hibrid hablur cecair berbentuk diskotik (DLC) yang terdiri daripada 2,3,6,7,10,11-heksakis (heksiloksi) trifenilin (HAT6) dan garam aluminium triklorida ($AlCl_3$). Sifat-sifat termoelektrik bahan PELC boleh diubahsuai telah dicapai dengan menambahkan campuran konsentrasi 5CB yang berbeza ke dalam polimer PVA. Peningkatan ke atas kekonduksian elektrik dan koefisien Seebeck telah terbukti hasil daripada sifat termotropik hablur cecair yang boleh tersusun secara sendiri ketika peralihan fasanya, dan pada masa yang sama pertambahan konsentrasi 5CB juga didapati telah merendahkan kekonduksian terma bahan bersistem PELC. Di dalam kajian DLC, kekonduksian elektrik untuk bahan hablur cecair diskotik HAT6 yang mempunyai pengangkutan pembawa bersifat quasi-satu-dimensi (1D) telah diselidiki untuk keupayannya sebagai calon komponen bahan penjana kuasa STEG. Selain itu, penyerapan cahaya oleh HAT6 juga telah dikaji untuk tujuan yang sama. Pertindihan disk-disk telah diperhatikan dapat membantu kekonduksian elektrik kerana sifat kekonduksian 1D yang sama seperti di dalam dawai-nano. Kajian ke atas struktur

HAT6 dan kesannya terhadap sifat-sifat elektronik dan terma diselidiki dengan menganalisa spektrum-spektrum Raman, dan dihubungkan dengan simulasi menggunakan teori fungsi ketumpatan (DFT). Keputusan dari eksperimen Raman menunjukkan hubungkait yang sangat kuat diantara teras dengan teras bagi bahan LC di dalam fasa kolumnar, yang mempunyai kesan seperti 'memori' yang dipanjangkan sehingga ke fasa isotropik di dalam skala masa femtosaat. Hubungkait ini juga mengesahkan peningkatan kekonduksian elektrik di dalam fasa DLC melalui eksperimen yang dijalankan untuk menyukat kekonduksian elektrik bahan DLC. Simulasi DFT juga telah dijalankan untuk menjelaskan hubungan diantara sifat asas DLC seperti sela tenaga, menunjukkan hasil keputusan spektrum Raman. Hasil yang menarik daripada simulasi ini menunjukkan di dalam model molekul yang mempunyai ruang tanpa batasan, ianya mempunyai lebih fleksibiliti dan mengurangkan sela tenaganya. Demikian itu, kajian ini menerangkan pemahaman terhadap hubungkait diantara susunan kolumnar dan kekonduksian elektrik oleh molekul HAT6, dan strategi yang berpotensi untuk merekabentuk DLC sebagai aplikasi-aplikasi elektronik.

Kata kunci: Penjana kuasa suria termoelektrik, hablur cecair, hablur cecair diskotik, spektroskopi Raman, teori fungsi ketumpatan

ACKNOWLEDGEMENTS

I am grateful for the health and the wealth that The Almighty God has graced me through thick and thin that is the course of my PhD journey. For that, I have been able to complete this thesis in order to fulfil the requirement for this degree, a PhD.

I wish to thank everyone who has supported me throughout the years from the inception of this work, constructive criticisms that have motivated me to do better, also the kind words spoken and the grand small gestures that has stayed in my heart and kept my spirit alive. My advisor and thesis supervisor, Assoc. Prof. Dr. Suhana Mohd Said, to whom I have to thank for many reasons. Notably for encouraging me to be a better researcher, the impactful guidance at challenging times and highly sophisticated solutions for the seemingly impossible tasks. I am grateful for the ever-elegant advice, my thesis co-supervisor, Assoc. Prof. Dr. Faizul Mohd Sabri has given me and I admire his methodical approach towards problem solving. I have never felt more motivated and positively encouraged after every discussion we have had. Working with them had been a very interesting experience, as I had the opportunities to observe their dynamics, how they complemented each other. I am also indebted to my friends and some of the following academic figures; Syukri, Fahmi, Hazwan, Akmal, Ilyana, Faris, Syafie, Megat, Aminah, Fitriyani, Waqar, Ethar, Fini, Ammar K., Nakajo, Arif, Amirul, Ammar S., Badri and Dr Faiz. Many fascinating discoveries during my PhD journey have been with the help of these people, enduring these tough years have been worthwhile. I also wish to thank the institutions which have supported me during working on my thesis; KPT scholarship (MyPhD) and fundings (HIR and UMRG) I have received in the years of reading for my PhD degree. My special thanks go to Dr Malik Qassim whom have guided me when he was in the University of Cambridge, during my research visit in 2014 and also Prof. Oussama Moutanabbir of Polytechnique de Montreal whom I grateful for the research internship opportunity that he had welcomed me in 2015.

I dedicate this thesis to the memory of my late father, Sahamir Bin Mohd Hassan, and my late grandmother Bee Binti Abdullah. Finally, I would like to express my great thankfulness and appreciation to my family, especially to my mother, Rathiah Binti Shamsuddin for continuous support and encouragement.

University of Malaya

TABLE OF CONTENTS

Abstract	iii
Abstrak	v
Acknowledgements	vii
Table of Contents	ix
List of Figures	xv
List of Tables.....	xxi
List of Symbols and Abbreviations.....	xxii
CHAPTER 1: INTRODUCTION.....	1
1.1 Motivation.....	6
1.2 Problem Statement.....	9
1.3 Objectives	9
1.4 Thesis Scope and Organisation.....	10
CHAPTER 2: LITERATURE REVIEW.....	13
2.1 Overview of Thermoelectricity.....	13
2.2 Thermoelectrics: From Inorganic to Organic Semiconductors	14
2.3 Thermoelectrics: Theory behind the Phenomena	17
2.3.1 Generalised Description of Seebeck Coefficient.....	18
2.4 Thermoelectrics: Devices and Applications	19
2.5 Solar Thermoelectric Generator (STEG).....	22
2.6 STEG Device Modelling	24
2.7 Conducting Polymers and Organic Semiconductors	26
2.7.1 Electronic Properties of Conducting Polymers and Organic Semiconductors	30

2.7.2	Charge Transport Mechanisms in CP and OSC Materials and their TE Behaviours.....	31
2.7.2.1	Band Conduction.....	31
2.7.2.2	Hopping Transport.....	32
2.7.2.3	Ionic Conduction.....	33
2.7.2.4	The Effect of Temperature.....	34
2.8	Liquid Crystal Materials.....	34
2.8.1	Polymer Electrolyte Liquid Crystals (PELCs).....	36
2.8.2	DLC as Organic Semiconductors.....	37
2.8.3	Electronic and Charge Transport Properties of DLCs.....	40
2.8.3.1	Doping of DLCs.....	41
2.9	Temperature Dependent Measurement Techniques for TE Materials.....	43
2.9.1	Electrical Conductivity.....	44
2.9.2	Seebeck Coefficient.....	46
2.9.3	Thermal Conductivity.....	47
2.9.4	Raman Spectroscopy.....	48
2.10	Molecular Simulation of Organic Semiconductors.....	51
2.11	Molecular Dynamics.....	53
2.12	Quantum Modelling.....	54
2.12.1	Molecular Modelling of DLCs and Small Organic Molecules.....	56
2.13	Summary.....	58
CHAPTER 3: METHODOLOGY.....		59
3.1	Modelling of Organic STEG Device.....	60
3.1.1	Simulation of Heat Entrapment of Solar Radiation for a Graded Multilayer Solar Funnel STEG.....	60
3.1.1.1	Geometry of STEG.....	60

3.1.1.2	Material Properties	61
3.1.1.3	Governing Equations for Solar Absorbance.....	62
3.1.1.4	Boundary Conditions.....	63
3.2	Preparation of samples.....	65
3.2.1	Preparation of Polymer-Electrolyte Liquid Crystal (PELC) Samples.....	65
3.2.2	Preparation of DLCs samples.....	66
3.2.2.1	DLC materials and mixtures	66
3.2.2.2	Substrate-DLCs-Air interfaced sample	67
3.2.2.3	Ternary mixtures of liquid crystals	68
3.2.2.4	AlCl ₃ Doped HAT6	68
3.2.2.5	DLCs Cells	69
3.2.2.6	Preparation of Graphene Cells	70
3.3	Thermal Characterisation.....	70
3.4	Optical Characterisation	70
3.5	Characterisations of Various Organic Semiconductor Systems	71
3.5.1	PELC System	71
3.5.1.1	Electrical Conductivity and Seebeck Coefficient Measurements	71
3.5.1.2	Thermal Conductivity Measurement.....	72
3.5.2	DLCs system	72
3.5.2.1	Van der Pauw Electrical Conductivity Measurement	72
3.5.2.2	Seebeck Coefficient Measurement.....	73
3.5.2.3	Hall Effect	74
3.6	Temperature Dependence Raman Spectroscopy Measurement	74
3.7	MD Simulations and DFT Calculations	75
3.7.1	FORCITE MD Calculations	76

3.7.2	DMol3 DFT Calculations	77
CHAPTER 4: DISCUSSION		78
4.1	Device Specifications of Solar Thermoelectric Generator	78
4.1.1	Heat Entrapment Due to a Graded Multilayer Solar Funnel STEG	78
4.1.1.1	Convection Effect.....	80
4.1.1.2	Radiation Effect.....	81
4.1.1.3	Geometry Optimisation	83
4.1.1.4	Thermal Capturing of Single n-Type Leg Thermoelectric Column	
	84	
4.1.2	Thermoelectric Power Output of Graded Multilayer Solar Funnel STEG...	
	85
4.1.2.1	Effect of Contact Resistance	85
4.2	Temperature Dependent Properties of the Polymer-Electrolyte-Liquid Crystals (PELC) Systems	89
4.2.1	Polymer Electrolyte System (PVA+KI)	90
4.2.2	Polymer-Inorganic (additive) Electrolyte System (PVA+KI+ZnO)	90
4.2.3	Polymer Electrolyte Liquid Crystals System (PVA+KI+5CB).....	91
4.2.3.1	Differential Scanning Calorimetry, DSC	92
4.2.3.2	Electrical Conductivity.....	93
4.2.3.3	Seebeck Coefficient.....	95
4.2.3.4	Thermal Conductivity Measurement.....	96
4.2.3.5	Dimensionless Figure of Merit, ZT	97
4.3	Temperature Dependent Properties of Discotic Liquid Crystal (DLC) Systems ..	99
4.3.1	HAT10.....	99
4.3.1.1	Investigation on Mesomorphic Properties by POM.....	99
4.3.1.2	Differential Scanning Calorimetry, DSC	100

4.3.1.3	Electrical Conductivity.....	101
4.3.2	HAT6.....	105
4.3.2.1	Investigation on Mesomorphic Properties by POM.....	105
4.3.2.2	Differential Scanning Calorimetry, DSC	106
4.3.2.3	Electrical Conductivity.....	107
4.3.3	HAT6, Smectic and Ferroelectric Ternary Liquid Crystals Mixtures	108
4.3.3.1	Investigation on Mesomorphic Properties by POM.....	108
4.3.3.2	Differential Scanning Calorimetry	111
4.3.3.3	Electrical Conductivity.....	112
4.3.3.4	UV-VIS Experiment.....	115
4.3.4	HAT6 Doped AlCl ₃	116
4.3.4.1	Investigation on Mesomorphic Properties by POM.....	117
4.3.4.2	Electrical Conductivity.....	119
4.3.4.3	Mobility by Space Charge Limited Current (SCLC) Method .	121
4.3.4.4	UV-VIS Experiment.....	123
4.4	Studies on Structural Relation of Discotic Materials with Electrical, Electronic and Thermal Properties.....	124
4.4.1	Linewidth Analysis of Raman Spectra	125
4.4.1.1	C-H vibrational modes towards aliphatic chains end (1350-1420cm ⁻¹)	128
4.4.1.2	Symmetrical stretching of aromatic cores in HAT6 (1420-1460cm ⁻¹)	130
4.4.1.3	Symmetrical quinoidal vibrations of the aromatic cores of HAT6 (1600 to 1650 cm ⁻¹).....	132
4.4.2	Energy Shift in Raman Spectroscopy.....	135
4.4.3	Relaxation time.....	136

4.5	DFT Simulation	138
4.5.1	HOMO-LUMO Energies Calculations.....	138
4.5.1.1	Band Gap of HAT6	138
4.5.1.2	Relative Energy Levels of HAT6 and AlCl ₃	140
4.5.2	DFT Calculated Raman Spectra	141

CHAPTER 5: CONCLUSION AND RECOMMENDATION144

5.1	To define the specifications for an “solar funnel” based device architecture using finite element analysis modelling	144
5.2	To investigate the electrical properties and Seebeck coefficient of PELC systems	145
5.3	To characterise the electrical and optical properties of DLCs.....	145
5.4	To understand the electronic charge transport in self-assembled HAT6 discotic liquid crystals through structural and molecular vibration studies.....	147
5.5	To investigate the structural-electronic correlation of DLCs using molecular modelling.....	147
5.6	Recommendations for future works.....	148
	References.....	149
	List of Publications and Papers Presented	160

LIST OF FIGURES

Figure 1.1: Thermoelectrics as a solution for clean energy.	2
Figure 1.2: The flow of global incoming solar radiation energy shows the abundance of solar radiation received on earth (Pidwirny, 2006).	7
Figure 1.3: Multilayer thin films with gradually increasing densities to serve as thermal capacitor in STEG device.	8
Figure 2.1: Typical schematic of thermoelectric devices.	14
Figure 2.2: Nanocomposite strategy through nanoplatelet composite demonstrated by Sony et al., 2012 (a) electrical resistivity, (b) Seebeck coefficient, (c) thermal conductivity, and (d) figure of merit, ZT, (Soni et al., 2012).	16
Figure 2.3: The estimation of thermoelectrics efficiency compared to the mechanical heat engines performance as assessed by Vining C.B., 2009 (Cronin B Vining, 2009).	20
Figure 2.4: (left) Targeted TEG used for automobile, bypassing the exhaust of Ford Fusion, with 500 Watts capacity (Fairbanks, 2011). (right) The Mars Rover Curiosity with RTG operating between 100 to 125 Watts (Ritz & Peterson, 2004).	21
Figure 2.5: Structure of an STEG cell by Kraemer, 2011.	22
Figure 2.6: The architecture and boundary conditions of segmented (a) and cascaded (b) STEGs modeled by McEnany et al., 2011 (McEnaney, Kraemer, Ren, & Chen, 2011).	25
Figure 2.7: The progress in thermoelectric studies in conducting polymers and organic semiconductor materials according to their figure of merits.	28
Figure 2.8: Route map of research in the field of conducting polymers and organic semiconductor materials.	30
Figure 2.9: Different classes of liquid crystals.	35
Figure 2.10: The organization of self-assembled LCs. (left) DLCs. (right) Calamitic LCs.	35
Figure 2.11: (a) Schematic representation of a 5CB molecule. (b) Dipole mapping of the 5CB molecule. There is a strong dipole moment along the longitudinal axis of the molecule. (c) Phase transition diagram and the temperature of the 5CB, represented by each small bar.	37
Figure 2.12: Illustration of the quasi-1D and -2D of stacking DLC disc-like molecule.	38

Figure 2.13: Dependence of number of Carbon atoms on the charge mobilities of several DLC materials (HAT6= triphenylene, HBC= hexabenzocoronene).....	41
Figure 2.14: Band matching strategy between HAT6 molecule and F4TCNQ dopant molecule (Khan et al., 2016).....	42
Figure 2.15: Different contact arrangements for resistivity and Hall effect measurements: (a) contact arrangement on bar shaped sample. (b) 6-point and (c) 5-point contacts (d) resistivity measurement on non-uniform sample (Borup et al., 2015).....	45
Figure 2.16: Measurement of Seebeck coefficient on samples with different geometries. (a) 2-point setup. (b) off-axis 4-point. (c) uniaxial 4-point (Borup et al., 2015).	47
Figure 2.17: Measurement methods of thermal conductivity: (a) Thermal diffusivity measurement with the laser flashes method using IR camera to monitor the rise of temperature on the top side of the sample. (b) Steady state method (c) PPMS TTO: heat pulse transient method (Borup et al., 2015).	48
Figure 2.18: Scattering mechanism in Raman spectroscopy measurement.	49
Figure 2.19: Molecular modelling using Materials Studio software.....	52
Figure 2.20: Time versus atomic scales of different computational methods.....	53
Figure 3.1: The flow chart of research methodology.	59
Figure 3.2: Schematic of planar multilayer thin film.	61
Figure 3.3: Boundary conditions of single thermoelectric leg.	63
Figure 3.4: Mechanism of spin coating process. The uniformity of coated sample is governed by radial liquid flow and evaporation of solvent.....	68
Figure 3.5: Preparation of DLC in ITO cell.....	69
Figure 3.6: Setup of electrical conductivity and Seebeck coefficient measurements using Ozawa scientific equipment.	71
Figure 3.7: Schematic illustration of Van der Pauw measurement.....	73
Figure 3.8: Schematic of laboratory fabricated setup for measurement of Seebeck coefficient.....	73
Figure 3.9: The setup for electrical conductivity and Seebeck coefficient measurements.	74
Figure 3.10: Schematic diagram for Raman spectroscopy measurement.	75

Figure 3.11: Drawing of molecular structure of HAT6 by using Materials Studio.	76
Figure 4.1: Solar irradiance for Malaysia geographical position.	79
Figure 4.2: Effect of diffuse radiation on the temperature of thermoelectric absorber. ...	80
Figure 4.3: Plot of heat entrapment as a function of time in a 24-hour cycle, for varying convection coefficients.	81
Figure 4.4: Effect of absorber emissivity on the temperature of thermoelectric absorber.	82
Figure 4.5: Effect of multilayer thin film radiation properties on the temperature of thermoelectric absorber.	82
Figure 4.6: Inverted multilayer structure with copper electrode as the outer side part exposed to the sun.	83
Figure 4.7: Comparison of the solar entrapment behavior, based on the original set of parameters, compared against modifications in geometry, thermal conductivity and inverted structure.	84
Figure 4.8: Temperature distribution for a single leg n-type thermoelectric in Case 1. .	85
Figure 4.9: Temperature distribution for a single leg n-type thermoelectric in Case 2. .	85
Figure 4.10: Voltage output of multilayer thermoelectric device in response with contact resistance.	86
Figure 4.11: Current output of multilayer thermoelectric device in response with contact resistance.	86
Figure 4.12: Overall multilayer thermoelectric device resistance in response with contact resistance.	87
Figure 4.13: Power output of multilayer thermoelectric device in response with contact resistance.	87
Figure 4.14: Electrical conductivity measurement of PVA polymer-KI electrolyte with and without ZnO as additive.	91
Figure 4.15: DSC curves for the PELC mixtures (5CB contents are 0, 5, 10, 15, 20, and 25%). The nematic-isotropic transition temperature for each PELC mixture is also shown.	93

Figure 4.16: Electrical conductivity of the PELC mixtures (5CB contents are 0, 5, 10, 15, 20 and 25%). The nematic-isotropic transition temperatures are also shown in the figure	94
Figure 4.17: Seebeck coefficient vs temperature for the different PELC mixtures (5CB contents are 0, 5, 10, 15, 20 and 25%). The nematic-isotropic transition temperature is also shown in each figure	95
Figure 4.18: ZT value of the PELC mixtures as a function of 5CB content at the lowest and highest temperatures. Gray dotted and solid lines are guide for the eyes to show a trend of ZT at the lowest and highest temperatures, respectively	97
Figure 4.19: Optical textures of HAT10 compound under POM, Cr phase (left), planar alignment in liquid crystalline phase (middle), Iso phase (right).....	100
Figure 4.20: DSC thermogram of HAT10 compound	101
Figure 4.21: The measurement of temperature-dependent electrical conductivity of HAT10 on ITO substrate during heating and cooling cycles using Van der Pauw setup. The arrows indicated the progress sequence of the measurement which goes from room temperature to 100 and back to room temperature again	102
Figure 4.22: Electrical conductivity measurement of spin coated HAT10 on ITO substrate	103
Figure 4.23: Mobility measurement of spin coated HAT10 on ITO substrate	104
Figure 4.24: (left) Seebeck coefficient measurement of HAT6 coated on ITO substrate. (top right) The plot of absolute temperature calculated by averaging T_{Hot} and T_{Cold} against the temperature difference, ΔT . (bottom right) Determination of Seebeck coefficient from the plot of Seebeck voltage against ΔT , i.e. all the points corresponded to absolute temperature of 26 °C.	105
Figure 4.25: Optical textures of HAT6 compound under POM, Cr phase (left), D_h phase (middle), a spur of transition from D_h into Iso phase (right).	106
Figure 4.26: DSC thermogram of HAT6 compound	107
Figure 4.27: Temperature-dependent electrical conductivity of HAT6 during cooling and heating cycles	108
Figure 4.28: POM of sample with 20% of HAT6 content in LC mixtures	109
Figure 4.29: POM of sample with 40% of HAT6 in LC mixtures. Maltese cross pattern has been observed due to nucleation of crystal	110

Figure 4.30: POM of sample with 60% of HAT6 in LC mixtures. The brushes have been observed to grown in single direction.	110
Figure 4.31: POM of sample with 80% of HAT6 in LC mixtures. The brushes have been observed to interwoven each other.	111
Figure 4.32: DSC thermograms of liquid crystal mixtures.	112
Figure 4.33: Temperature-dependent electrical conductivity of DLC, Smectic A, and Ferroelectric ternary LC mixtures.	113
Figure 4.34: Electrical conductivity of different percentages of HAT6 mixtures and $AlCl_3$ doped HAT6 sandwiched in different substrates.	114
Figure 4.35: UV-Vis absorption results of HAT6 mixtures.	115
Figure 4.36: Calculated optical band gap of ternary liquid crystal mixtures at room temperature.	116
Figure 4.37: POM images during columnar phase for each mixture at different $AlCl_3$ concentrations.	118
Figure 4.38: AC and DC-electrical conductivities of $AlCl_3$ doped HAT6 DLC.	120
Figure 4.39: AC electrical conductivity of $AlCl_3$ doped HAT6 DLC in columnar phase at 70 °C	121
Figure 4.40: Mobility plot of HAT6 mixtures	122
Figure 4.41: UV-Vis absorption results of HAT6 mixtures.	123
Figure 4.42: Calculated optical band gap of various percentage of $AlCl_3$ doping concentration in HAT6 at room temperature.	124
Figure 4.43: Temperature-dependent Raman spectra of HAT6 compound using 488 nm laser.	127
Figure 4.44: Temperature-dependent Raman spectra of HAT6 compound using 514 nm laser.	128
Figure 4.45: Raman spectra of C-H tails for (a) 488 nm and (b) 514 nm laser source. (c) The modes of vibrations of C-H atoms in the alkyl chains of HAT6.	129
Figure 4.46: Raman spectra in the region between 1410 cm^{-1} to 1450 cm^{-1} for (a) 488 nm and (b) 514 nm laser lines (c) Symmetrical stretching mode of C-C atoms in aromatic rings.	131

Figure 4.47: FWHM of symmetrical stretching mode of C-C atoms from 514 nm excitation Raman curves in the range of 1440-1460 cm^{-1}	132
Figure 4.48: Quinoidal stretching of aromatic rings in HAT6 molecule.	133
Figure 4.49: Fitted profile for C=C stretching using 488nm laser source (top left), area under the curve for each temperature profile (top right), deconvolution of C=C band of aromatic ring (top left), shifting evolution in the 2 nd peak (bottom right).	133
Figure 4.50: Raman spectra bands of C=C bonds of aromatic ring (left), area under the curve for each temperature profile (right) under 514nm light source.	134
Figure 4.51: FWHM of C=C curves for both 488nm and 514nm excitations.	134
Figure 4.52: The correlation between peak position shifting with temperature for quinoidal stretching mode of C=C bond at 514nm laser source is plotted.	135
Figure 4.53: Calculated temperature-dependent relaxation time.	137
Figure 4.54: In-plane geometrically optimized view of HAT6 molecules in (a) unspecified boundary model, and (b) periodic crystal model at 80°C. Location of HOMO and LUMO orbitals is shown respectively on the right.	139
Figure 4.55: Relative energy levels of HAT6 as host material and AlCl ₃ dopant in vacuum.	141
Figure 4.56: Simulated temperature-dependent Raman spectra of HAT6 molecule at 27°C (left) and 80°C (right).	142

LIST OF TABLES

Table 2.1: General characteristics of thermoelectric materials	15
Table 2.2: Comparison of TEG modules for low power application.....	21
Table 2.3: Examples of polymer monomer which are commonly researched in various electronic applications, i.e. thermoelectrics, solar cells, OLEDs and OTFTs	29
Table 2.4: A summary of the measurement method and apparatus used in thermoelectric performance measurement for conducting polymers and organic materials with carbon particle based composites.....	44
Table 3.1: Investigated parameters in FLUENT modelling.....	64
Table 3.2: List of parameters for a single thermoelectric leg containing three layers of conducting polymers in ANSYS device modeling	65
Table 3.3: Dimensions of simulated multilayer structure of thermoelectric device	65
Table 4.1: Thermoelectric Devices Power Output.....	88
Table 4.2: Thermal conductivity of the 5CB-free and PELC mixtures at 29 °C.....	97
Table 4.3: Summary of transition temperature and enthalpies for HAT10.	101
Table 4.4: Summary of transition temperature and enthalpies for HAT6.	107
Table 4.5: Transition Temperatures of AlCl ₃ Doped HAT6 Mixtures	117
Table 4.6: Summary of DFT calculations.....	140
Table 4.7: Summary of the simulated vibration modes.	142

LIST OF SYMBOLS AND ABBREVIATIONS

∇T	:	Gradient of temperature
∇V	:	Gradient of voltage potential
1D	:	One-dimensional
2D	:	Two-dimensional
3D	:	Three-dimensional
3ω	:	Thermal conductivity measurement from 3ω voltage frequency
5CB	:	4-Cyano-4'-pentylbiphenyl
AC	:	Alternating current
$AlCl_3$:	Aluminium trichloride
Bi_2Te_3	:	Bismuth telluride
CNT	:	Carbon nanotube
CP	:	Conducting polymer
Cpi	:	Complimentary polytopic interaction
Cr	:	Crystalline phase
DA	:	Donor-Acceptor
DC	:	Direct current
DFPT	:	Density functional perturbation theory
DFT	:	Density functional theory
D_h	:	Hexagonal columnar phase
DLC	:	Discotic liquid crystal
DMSO	:	Dimethyl sulfoxide
DNP	:	Double numeric plus
DO	:	Discrete ordinate
DSC	:	Differential scanning calorimeter

DSSC	:	Dye sensitised solar cell
e	:	Electron charge
E	:	Electric field
E	:	Energy of electron
E*	:	Transport energy
E _C	:	Energy at conduction band
E _F	:	Fermi energy
E _g	:	Optical band gap
E _V	:	Energy at valence band
F4TCNQ	:	2,3,5,6-Tetrafluoro-tetracyanoquinodimethane
FcTFB	:	Ferrocenium tetrafluoroborate
FePS ₃	:	Few-layer phosphochalcogenide
FET	:	Field effect transistor
FWHM	:	Full width at half maximum
GGA	:	Generalised gradient approximation
h	:	Planck constant
HAT6	:	2,3,6,7,10,11-hexakis(hexyloxy)triphenylene
HHTT	:	2,3,6,7,10,11-Hexakis(hexylthio)triphenylene
HOMO	:	Highest occupied molecular orbital
I	:	Current
IPA	:	Isopropyl alcohol
IR	:	Infrared
Iso	:	Isotropic phase
ITO	:	Indium tin oxide
j	:	Electric current density
k _B	:	Boltzmann constant

KI	:	Potassium iodide
K_n , $n=0,1,2,\dots,n$:	Second rank tensor
L	:	Thickness
LC	:	Liquid crystal
LCAO	:	Linear combination of atomic orbital
LED	:	Light emitting diode
LUMO	:	Lowest unoccupied molecular orbital
m^*	:	Effective mass
MD	:	Molecular dynamics
MM	:	Molecular modelling
n	:	Carrier concentration
NOBF ₄	:	Nitrosonium tetrafluoroborate
OLED	:	Organic light emitting diode
OSC	:	Organic semiconductor
OTFT	:	Organic thin film transistor
p	:	Holes concentration
PBE	:	Perdew-Burke-Ernzerhof
PbTe	:	Lead telluride
PEDOT:PSS	:	Poly(3,4-ethylenedioxythiophene):Poly(styrenesulfonate)
PELC	:	Polymer electrolyte liquid crystal
PF	:	Power factor
POM	:	Polarising optical microscope
PR-TRMC	:	Pulse radiolysis-time resolve microwave conductivity
PV	:	Photovoltaic
PVA	:	Polyvinyl alcohol

q	:	Thermal current density
QENS	:	Quasi elastic neutron scattering
QM	:	Quantum mechanics
Q_{Peltier}	:	Peltier energy
Q_{Thomson}	:	Thomson energy
RTG	:	Radioisotope thermoelectric generator
S	:	Seebeck coefficient
SCF	:	Self-consistent field
SCLC	:	Space charge limited current
STEG	:	Solar thermoelectric generator
STEG	:	Solar thermoelectric device
T	:	Temperature
TE	:	Thermoelectric
TEG	:	Thermoelectric generator
TNF	:	Trinitrofluorenone
TOF	:	Time of flight
UPS	:	Ultraviolet photoelectron spectroscopy
UV	:	Ultraviolet
V	:	Applied voltage
Vis	:	Visible
v_k	:	Velocity of particle
XRD	:	X-Ray diffraction
ZnO	:	Zinc oxide
ZT	:	Figure of merit
α	:	Seebeck coefficient
ΔH	:	Enthalpy change

ΔT	:	Temperature difference
ΔV	:	Voltage potential difference
ϵ	:	Dielectric constant
κ	:	Thermal conductivity
κ_e	:	κ contribution from transported electrons and holes
κ_L	:	κ contribution from lattice phonons
μ_h	:	Holes mobility
π	:	Peltier coefficient
π^*	:	Pi bond
σ	:	Electrical conductivity
τ	:	Thomson coefficient
τ_{rel}	:	Relaxation time constant
\hbar	:	Modified Planck constant

CHAPTER 1: INTRODUCTION

There is an increasing trend of biomimicry in science, engineering and medicine practices. Drawing inspiration from nature's elegant strategies, scientists, engineers, and innovators alike has made it possible to engineer various innovations by understanding their natural mechanisms. For example, solar cells which simulate photosynthesis process in the green plants demonstrate the natural ability of the plants to convert chemical reaction into useful energy from light energy. This plays significant role in the development of solar cells architecture. Implementing this mechanism in electronic applications has led to numerous creative inventions and rapid progress in solid state technologies. In this work, the ability of the seawater to store heat in its salty bodies has inspired the conceptual work on solar thermoelectric generators (STEGs). The capacity of heat storage in saline water is evidence based on the temperature profile of seawater against its depth, where the top portion of the seawater is usually the warmest and the temperature gradually decreasing towards the bottom of the ocean. This nature inspired phenomenon is the primary motivation of this work on STEGs.

STEG is a type of thermoelectric generators (TEGs). TEGs are solid-state energy harvesting devices which convert heat into electricity. TEG device promotes a strategic path in solving thermal management problem by make use of the waste heat from various sources as illustrated in Figure 1.1. Thermal problem poses major limiting factor of scaling semiconductor technology i.e. unutilised wasted heat and undesirable heating in electronics component. Reliability of the silicon chip decreases by 10% for every 2 °C rise of temperature. More than 50% of the electronic failures are temperature related (Alam & Ramakrishna, 2013; Du, Shen, Cai, & Casey, 2012). The components comprised of solid-state semiconductors in electronics should be reliable when used against temperature for them to perform well for many years. TEG can be used to provide cooling

by absorbing excessive heat in the electronic components, whilst at the same time generate small electricity. Whilst various discoveries have shown positive outcome for TEG applications with waste heat, several others are taking the innovation further by exploiting the abundance of solar radiation heating. Here STEG is proposed as the alternative extension to the regular TEG.

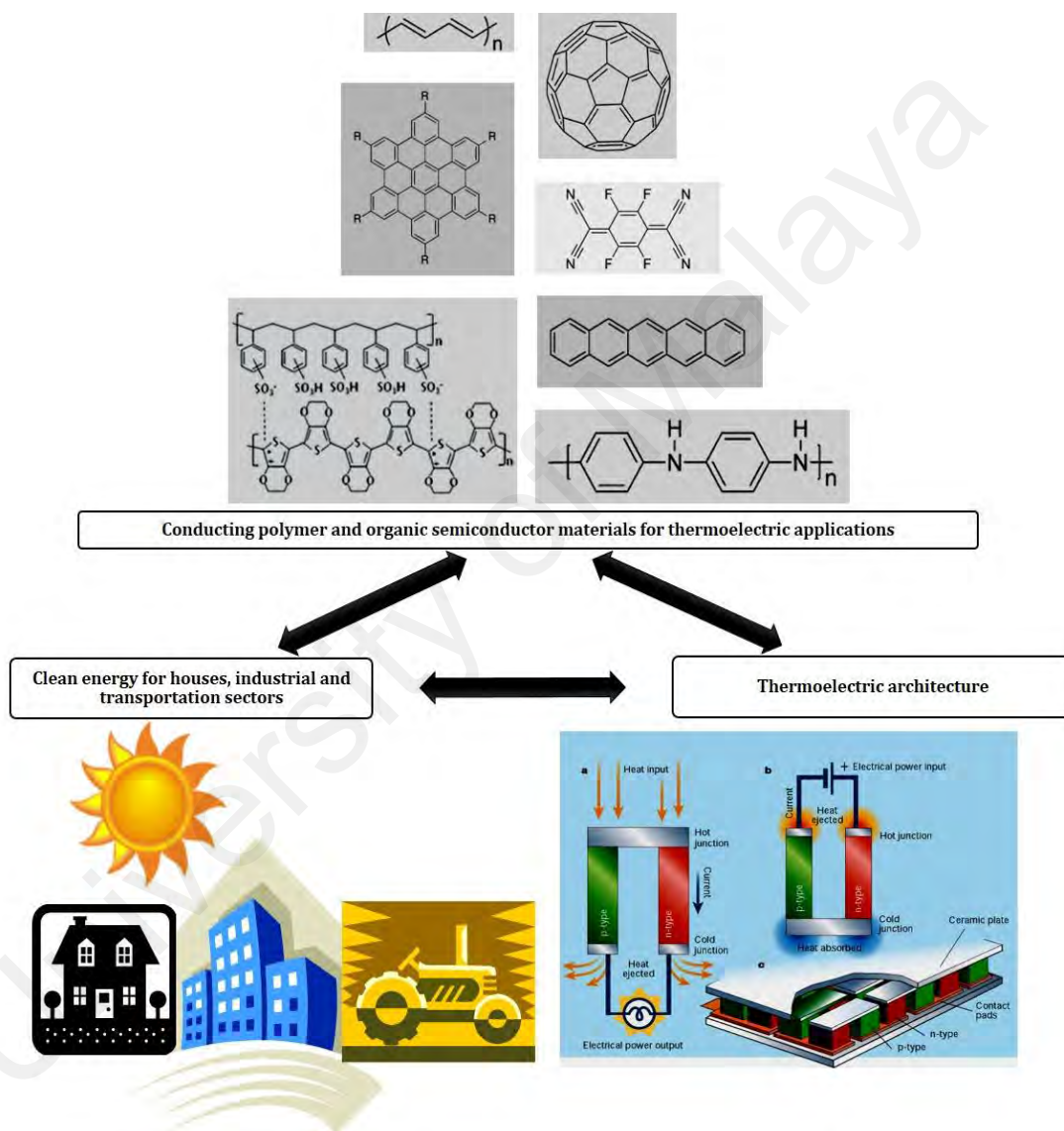


Figure 1.1: Thermoelectrics as a solution for clean energy.

Many solid-state energy conversion devices are conventionally based on inorganic semiconductors. For instance, silicon and gallium arsenide have been used as single junction crystalline materials in photovoltaics (PVs), light emitting diodes (LEDs) and field effect transistors (FETs). In the case of PVs performance, their reported power

conversion efficiencies have reached up to 30% by using these materials (Green, 2013). However, the demand was constrained due to high manufacturing costs resulting in increased price of photovoltaic cells. To fix this, lower cost of solar cells is enabled by the proposed alternative technologies such as organic based dye-sensitized solar cell (DSSC), originally invented by Michael Gratzel and Brian O'Regan in 1991. Similarly, inorganic semiconductors domination in thermoelectrics prevailed, yet the solution for a greener option remains elusive. For instance, the performance of a superlattice crystal made of inorganic bismuth telluride and antimony telluride has been reported among the highest figure of merit (ZT) of 2.4 for thermoelectric applications (Venkatasubramanian, Siivola, Colpitts, & O'Quinn, 2001). In 2014, another breakthrough was made when it was discovered by directing heat along b axis direction of orthorhombic unit cell in SnSe, ZT of 2.6 ± 0.3 at 923 K was achieved (L.-D. Zhao et al., 2014).

It is well established that inorganic semiconductors are known to have higher efficiency, however there remains a need for the use of alternative materials; conducting polymers (CPs) and organic semiconductors (OSCs) in favour of their advantages, i.e. cheaper costs for large-scale manufacturing, abundant in sources, lightweight, flexibility, heat resistivity, and biodegradability. The used of CPs and OSCs have been associated with the practice of promoting green technologies, due to their earth bound natural-like tendencies including non-toxicity. As a result, mass fabrications of electronics are more environmentally compatible when conducting polymers and organic semiconductor materials are being used. STEG device can benefit from this due to their usually large area when being produced using printing technique as an example to cover rooftops and windows.

Conductive polymers have been researched dated back as early as mid-19th century, albeit most of the works at the time were theoretical predictions. The discovery centred

on oxidized aniline polymer in acidic media by Henry Letheby serves as a precursor in the modern world for various achievements and breakthrough in electrically conducting polymer (Letheby, 1862). His work and many others in early days have inspired many physicists, chemists and engineers in the following decades and century in discovering electronically conductive polymers. In the mid-20th century, Alan J. Heeger, Alan MacDiarmid and Hideki Shirakawa reported high electrical conductivity in iodine doped polyacetylene prepared by electrochemical synthesis (Shirakawa, McDiarmid, & Heeger, 2003). Since then, the populous families of conducting polymers such as derivatives based on polypyrrole, polythiophene, polyaniline, poly (p-phenylene vinylene), poly (2,7-carbazolene vinylene), poly (2,5-dimethoxy phenylene vinylene) and many others have been introduced. The source of their conductivity is due to the mobility of the electrons between the conjugated chains of the polymer. Noting that CPs also has good optical properties, they are most likely a potential candidate for STEG.

The discoveries in conducting polymers field from decades ago are vital to today's technology, and they have since significantly revolutionized conducting electronic industries. The consumption of conducting polymers has been received well as they are potentially a solution to the world energy crisis in the future. It is imminent to see their use from rooftops to windows, pedestrian pavement, bicycle lanes and various creative directions should they be exploited in the application such as energy harvesting and myriad of other examples. Moreover, recent studies have shown that the electronic devices and applications such as solar cells, photonic sensors, electrolyte membrane in batteries, flexible supercapacitors and bioelectronics have found conducting polymers are very attractive as a replacement for inorganic semiconductor (Dubal, Ayyad, Ruiz, & Gomez-Romero, 2015; Heo et al., 2013; Knopfmacher et al., 2014; Lanzani, 2014; Russ, Glauddell, Urban, Chabinye, & Segalman, 2016; Shown, Ganguly, Chen, & Chen, 2015).

Another important class of materials is organic semiconductors. They are interesting due to their behaviour which is similar to that of inorganic materials. They can exist in the form of organic crystals. Aside from the electrochemical phenomenon which makes conducting polymers and organic semiconductors competitive in electronic applications such as batteries, fuel cells and solar cells, it is their semi crystalline ability which exhibit high ordering (alignment) that is vital in enhancing their electrical properties such as conductivity. Whilst most conducting polymers are not readily in aligned form, organic crystals do demonstrate this quality. Some organic semiconductors can behave in both crystalline-like and liquid-like manners. These materials which are identified as soft materials, which also exhibit order and mobility throughout multiphases are called Liquid Crystals (LCs). LC materials which presently represent a significant subject of organic electronic research have been studied and investigated for their potential use in electronic and opto-electronic applications. LCs have been associated with their general use in the screens of TVs, laptops and smartphones. Not many realised the very existence of beings in the universe was supported by the materials of the same class, LC molecules. Cell membranes were formed by lipids and molecular building blocks consisted of polymers and supramolecular organic molecules which are able to effectively organise themselves into various structures of DNA, proteins and enzymes. Biologically, our very own creation owed to this molecular self-assembled ability. This special ability makes LCs very attractive in number of applications especially in electronics. The ability to self-assemble is very useful property because it will add reliability to the materials over time especially when electronic devices are used in frequent manner. A study has concluded that 99.9% of the tested LC displays can last for more than 10 years, indicating their potential for long lifetimes.

LC molecules have many shape and various forms in order to serve specific function. LCs as organic semiconductors, which has building blocks that are made up of stacks of

aromatic rings consisting conjugated pi (π^*) bonds in each ring are often found in DSSCs, organic light emitting diodes (OLEDs), organic thin film transistors (OTFTs) and many other examples. These LC materials are classified as discotic liquid crystal (DLC) materials due to their disk-like geometry, i.e. porphyrin, hexabenzocoronene and triphenylene families of DLCs. Their counterparts such as nematic, smectic and ferroelectric liquid crystals are widely researched in display technologies due to their excellent electrooptic performance. DLC materials have been widely studied and researched in electronic applications due to their unique one-dimensional (1D) charge transport properties. The specific direction of charge migration along the stacking π^* bonded blocks which occurred mostly between polycyclic aromatic rings is important in delivering efficient charge transfer. This resulted in charge mobilities enhancement and high charge transfer rates as has been observed in nanowires. The nanowires-like properties make the use of DLCs attractive in electronic and optoelectronic applications and a potential candidate for STEG devices.

1.1 Motivation

Solar energy is one of the major sources of renewable energy. The earth surface has absorbed approximately 50% of incoming solar radiation as illustrated in Figure 1.2. Various types of solar energy conversion devices have been commercialized, due to the demand in energy producing industries (Chu & Majumdar, 2012; Giacoletto, 1959). To date, solar energy conversion devices include solar cells, water heaters, driers and air-conditioning have been used widely (Y.-G. Deng & Liu, 2009; Giacoletto, 1959; Heo et al., 2013; Thirugnanasambandam, Iniyan, & Goic, 2010). Recently, solar energy driven thermoelectric devices too have joined in the race, as solar energy harvesting devices. Although, their efficiencies remain being challenged when compete with existing technologies. (G. Chen, 2011; Y.-G. Deng & Liu, 2009; Salman B. Inayat, Kelly R. Rader, & Muhammad M. Hussain, 2012; Kraemer, Poudel, Feng, Caylor, Yu, Yan, Ma,

Wang, Wang, Muto, et al., 2011; Thirugnanasambandam et al., 2010; Yang, Xiao, Li, Zhai, & Zhang, 2011).

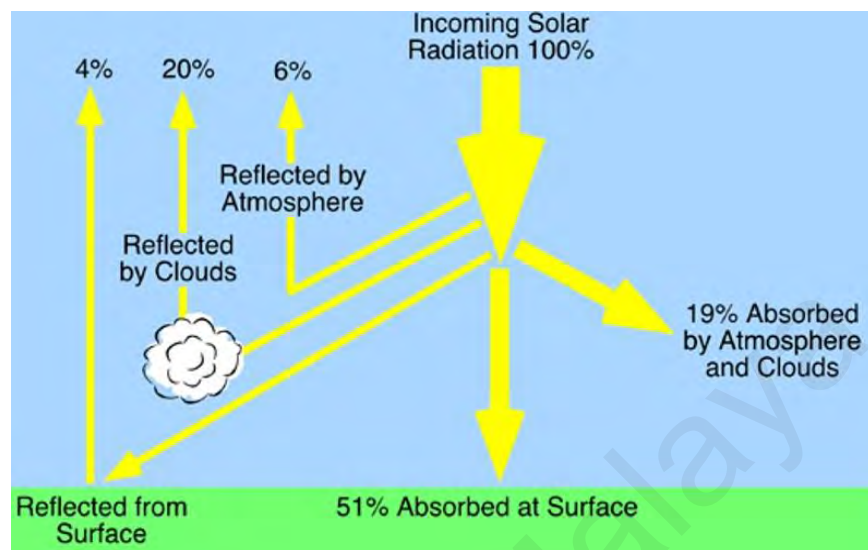


Figure 1.2: The flow of global incoming solar radiation energy shows the abundance of solar radiation received on earth (Pidwirny, 2006).

Thermoelectric devices such as TEGs produce electricity when a temperature gradient exists across semiconductor material's junction, and is thus an attractive technology for waste heat conversion, i.e. heat sources from automobile engines and combustion processes. On the other hand, solar thermoelectric generators (STEGs) utilize both light and heat from the sun to create the temperature gradient and have been studied extensively (Y.-G. Deng & Liu, 2009; Kraemer, Poudel, Feng, Caylor, Yu, Yan, Ma, Wang, Wang, Muto, et al., 2011; Yang et al., 2011). The designs which were previously studied have included external systems such as solar absorbers in order to collect heat from the sun (Kraemer, Poudel, Feng, Caylor, Yu, Yan, Ma, Wang, Wang, Muto, et al., 2011; Yang et al., 2011).

In this research, a thermoelectric device architecture which funnels heat from solar radiation as shown in Figure 1.3 is proposed, which features a built-in heat funnelling mechanism, comprising of stacks of multilayer thin film which are optically transparent and optically conductive, to form the p-n legs of the TE junction. In the proposed

architecture of the STEG, the densest layer of thin film will absorb and trap the incident solar radiation.

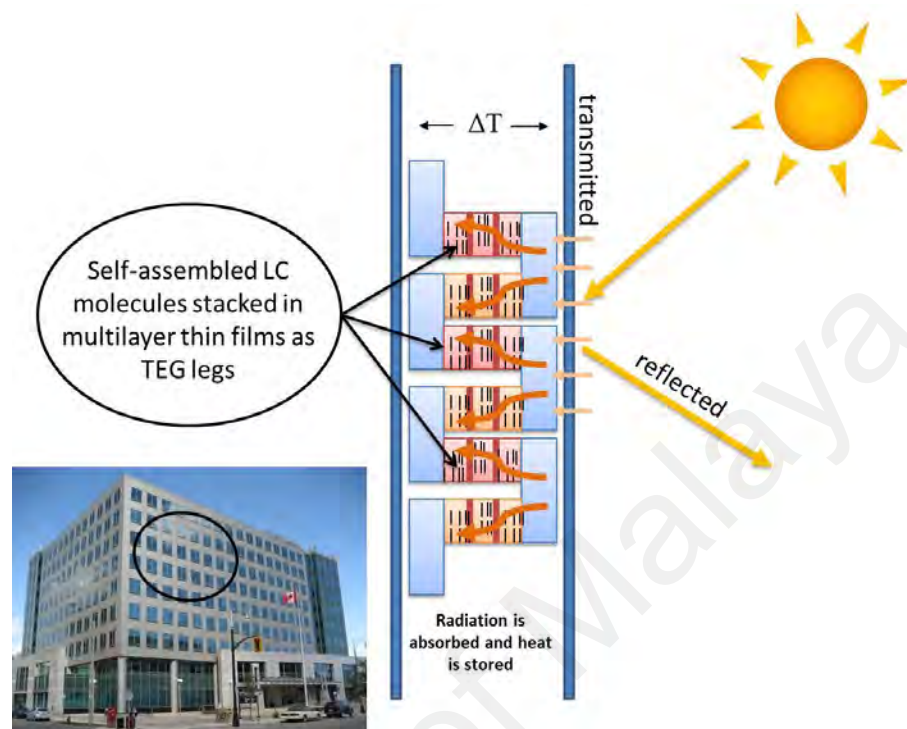


Figure 1.3: Multilayer thin films with gradually increasing densities to serve as thermal capacitor in STEG device.

The multilayer thin film consists of polymer layers of graduated densities, and corresponding graduated thermoelectric coefficients, across the layers, and serve the purpose as an effective heat absorbing and storage mechanisms. Such architecture is designed so that the multilayer thin film is able to store heat from solar radiation at the bottom layer making it possible to continuously harness the power from STEG even during night-time.

This proposed STEG architecture is proposed to be supported on the materials front by hybrid conducting polymer and self-assembled liquid crystals materials such as triphenylene based discotic liquid crystals. LCs exhibit self-assembly, which may prove to be beneficial both as a solar absorber and thermoelectric component. This work explores two LC systems: a polymer electrolyte-nematic LC system, and a column

stacked DLC system. The criteria evaluated for good STEG includes its electrical conductivity, Seebeck coefficient, thermal conductivity and optical absorption performance. Both LC systems will be evaluated based on these properties.

1.2 Problem Statement

LCs are regarded as very promising materials for various applications in organic electronic and optoelectronic devices. However, in the field of STEG, low efficiency of organic electronic material has hindered its development for this application. Recently, it has been identified that the key to a successful exploitation of electrical and electronic properties of LC materials vastly lies in their orderly molecular structure. Recent research suggests that LCs could be fashioned in orderly manner to achieve nicely organized molecular ordering, which will reflect in the performance of the devices. Thus, this research is proposed in order to investigate the LCs self-assembled ability for STEG application in this thesis. In this work, the self-assembly of LCs will be investigated in terms of its alignment, charge transfer, optical absorption, especially the thermoelectric properties and their capabilities for STEG application.

1.3 Objectives

In this thesis, an STEG device has been modelled using finite element analysis. The potential materials for the STEG are identified for this work as (1) hybrid polymer electrolyte liquid crystals and (2) discotic liquid crystals. The investigated parameters are the bulk material properties and fundamental molecular characteristics, i.e. structural order and charge transfer. The molecular level studies focus on structural-electronic correlation studies using Raman spectroscopy and Density Functional Theory. They are thus identified by the following objectives:

- i. To define the specifications for an “solar funnel” based device architecture using finite element analysis modelling

- ii. To investigate the electrical properties and Seebeck coefficient of PELC systems
- iii. To characterise the electrical and optical properties of DLCs
- iv. To correlate the electronic charge transport ability with structural order in self-assembled HAT6 discotic liquid crystals via molecular vibration studies
- v. To investigate the structural-electronic correlation of DLCs using molecular modelling

1.4 Thesis Scope and Organisation

- i. **Introduction:** In this chapter, the investigated topic is explained by introduction to the concept of STEG device. The potential working materials for STEG device is revealed. The problem statement has highlighted the existing exploration on LC materials, their properties and room for improvement. The objectives that can be used in order to systematically study and analyse the potential materials for STEG device are outlined.
- ii. **Literature review:** The theoretical and methodological contributions from previous researches and studies are compiled and briefly summarized. This includes the fundamental theories on thermoelectrics, device modelling, CPs and OSCs in thermoelectrics, liquid crystals for potential STEG application, measurement techniques and molecular simulation works.
- iii. **Methodology:** The methodologies of the research works are explained, coherent with the addressed objectives that need to be achieved. The techniques used in conducted experiments and computational works are then elaborated.
- iv. **Discussion** (This chapter is divided into 5 sub-chapters)
 - a) Sub-chapter 4.1 *Device Specifications of STEG*

This section covers a simulation on STEG structure using ambient condition in Malaysia and specified parameters such as optical, electrical and thermal properties.

b) Sub-chapter 4.2 *Temperature Dependent Properties of the Polymer-Electrolyte-Liquid Crystals (PELC) Systems*

A mixture of PVA polymer and KI electrolyte with 5CB liquid crystals is studied in the form of thin films. Their electrical conductivity is correlated with the percentage of embedded nematic liquid crystals inside the polymer matrix to identify optimal charge transfer. Thermoelectric property is discussed as well to show the Seebeck coefficient of the thin films. The figure of merit of the materials is calculated after the materials thermal conductivity was measured.

c) Sub-chapter 4.3 *Temperature Dependent Properties of Discotic Liquid Crystal Systems*

The electrical conductivities of various mixtures of DLCs were measured. The variations of the investigated mixtures include the ternary liquid crystal mixtures and Donor-Acceptor mixture containing $AlCl_3$ dopants. The results were correlated with the self-assembled properties and thermotropic properties of DLC during phase change process. The potential of DLCs to serve as working materials in STEG application is discussed.

d) Sub-chapter 4.4 *Studies on Structural Relation of Discotic Materials with Electrical, Electronic and Thermal Properties*

In earlier section, the results showed coherent correlation between molecular ordering and the electrical properties of DLCs. Raman spectroscopy technique is used in order to investigate the vibrational property, indirectly the structural order of DLCs have been linked. In this study, the interaction between the different chemical interaction of different parts of the molecule is correlated as a function of temperature.

e) Sub-Chapter 4.5 *DFT Simulation*

The highest occupied molecular orbital (HOMO) and lowest unoccupied molecular orbital (LUMO) energy of the DLC molecule were simulated using MD and DFT calculations as a function of temperature.

v. **Conclusion and Recommendation**

The investigations are finally concluded by evaluating the achievement in the works based on the accomplished objectives.

University of Malaya

CHAPTER 2: LITERATURE REVIEW

This chapter will provide a brief introduction into thermoelectricity and the sciences behind the thermoelectrics, i.e. fundamental mechanism of thermoelectric devices, an insight into potential polymeric and organic thermoelectric materials, and analysis techniques used to investigate their properties. Previous studies and researches on conducting polymers and organic semiconductors from material of LC class are compiled and critically discussed.

2.1 Overview of Thermoelectricity

Thermoelectrics phenomena was first discovered by Thomas Seebeck in 1821, when he found that an electromotive force was generated in a circuit made of two dissimilar metals which was heated at its joint. This discovery was later called Seebeck effect. Modern physics has described the phenomenon due to the movement of charge carriers (holes or electrons) in the semiconductor, creating electric current. The relationship between the electromotive force (ΔV) and the temperature difference (ΔT) can be written as $\Delta V = S\Delta T$, where S , or sometimes α , is used to denote a temperature dependent parameter called Seebeck coefficient. Peltier effect, which is the reverse of the Seebeck effect was discovered a few years later by Jean Peltier, when he observed that the heat was produced when voltage was applied. As for Peltier effect, the heat absorbed or rejected ($Q_{Peltier}$) from the surface of a semiconductor was found to be proportional to the passing electric current as follows: $Q_{Peltier} = \pi I$, where π is known as Peltier coefficient. The simultaneous actions of the two resulted in Thomson effect, described by the following equation: $Q_{Thomson} = \tau I \Delta T$, where τ is called Thomson coefficient. Heat is either absorbed or rejected ($Q_{Thomson}$) along the length of a semiconductor depending on the direction of the supplied current.

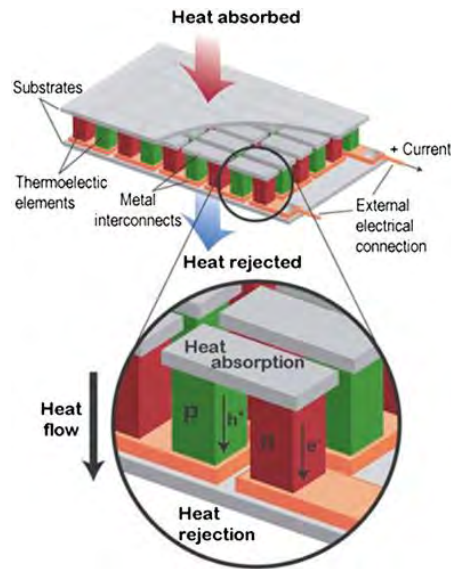


Figure 2.1: Typical schematic of thermoelectric devices.

Thermoelectricity has found its place in applications such as cooling, heating and power generation. Thermoelectric generators (TEGs) are used in power generation. They produce electricity when a temperature gradient exists across the p- and n-type junction of semiconductor materials, and is thus an attractive technology for waste heat conversion from sources such as automobile engines and combustion processes. TEGs provide an attractive premise for ‘green’ energy conversion, as they contain no moving parts and are able to directly generate electricity from waste heat. The capability of energy conversion in thermoelectric devices depends on its dimensionless figure of merit

$$\text{Dimensionless Figure of Merit, } ZT = \frac{S^2 \sigma}{\kappa} T \quad (2.1)$$

Typically, materials with a high Seebeck coefficient, S and electrical conductivity, σ , and low thermal conductivity, κ are suitable for thermoelectric devices. Figure of merit is necessary in grading the performance of thermoelectric materials and their applications (Donald, 1962).

2.2 Thermoelectrics: From Inorganic to Organic Semiconductors

The general thermoelectric characteristics of metals, insulators and semiconductors are provided in Table 2.1. Conventional inorganic thermoelectric materials which exhibited

the properties as listed in Table 2.1 such as PbTe and Bi₂Te₃ and their related compounds have demonstrated a viable thermoelectric generation potential for a diverse range of temperatures. Inorganic semiconductors from the families of PbTe and Bi₂Te₃ have made breakthroughs in thermoelectric performance due to their high power factor ($PF = S^2\sigma$). However, in term of enhancement in bulk inorganic materials, it has been found enhancing the electrical conductivity will lead to the decrease in Seebeck coefficient, and an increase in the thermal conductivity; which is the opposite of the effect that is desired, i.e. obtaining favourable ZT. Due to the interdependence of the correlation between the electrical conductivity, Seebeck coefficient and thermal conductivity, the options which are available for improving the ZT are limited.

Table 2.1: General characteristics of thermoelectric materials

Thermoelectric Properties Materials	Electrical Conductivity, S/m	Seebeck Coefficient, $\mu\text{V/K}$	Thermal Conductivity, W/m.K
Metals	Very high $\sim 10^7$	Low ~ 10	High $\sim 10^2$
Insulators	Extremely low $\sim 10^{-10}$	High	Low $\sim 10^{-4} - 10^{-2}$
Semiconductors	Moderate $\sim 10^{-3} - 10^4$	Tunable $\sim 10^2 - 10^3$	Tunable $\sim 10^{-1} - 10$

Figure 2.2 shows that, the increased in both the electrical conductivity and the Seebeck coefficient has affected the thermal conductivity by an increment over temperature (Soni et al., 2012). Different strategies have been employed in order to address the issue on simultaneous increase in thermal conductivity such as nano-structured composite blends. It started as early in 1990s, Dresselhaus, among the pioneer in thermoelectric field has discovered the effect of low dimensional materials and quantum-well structures on the figure of merit (Hicks & Dresselhaus, 1993a, 1993b). Nanostructured thermoelectric materials were designed such that the dimensionality of the materials is reduced; from 3D bulk to 2D surface to 1D structure such as nanowires or quantum dot, simplifying the mechanism of charge transport, with minimal losses via acoustic noise and any type of

energy transfer. Thus, nanostructured and low dimensional materials offer attractive prospect in thermoelectric field and widely researched nowadays (Biswas et al., 2012; L.-D. Zhao et al., 2014). Thus, from bulk to nano composite blend (i.e. nanoplatelet composites), materials dimensional manipulation (i.e. superlattices, quantum dots) and various methodologies have been implemented and have demonstrated viability in order to improve the ZT of inorganic thermoelectric materials (Biswas et al., 2012; Hsu et al., 2004; Poudel et al., 2008; Venkatasubramanian et al., 2001).

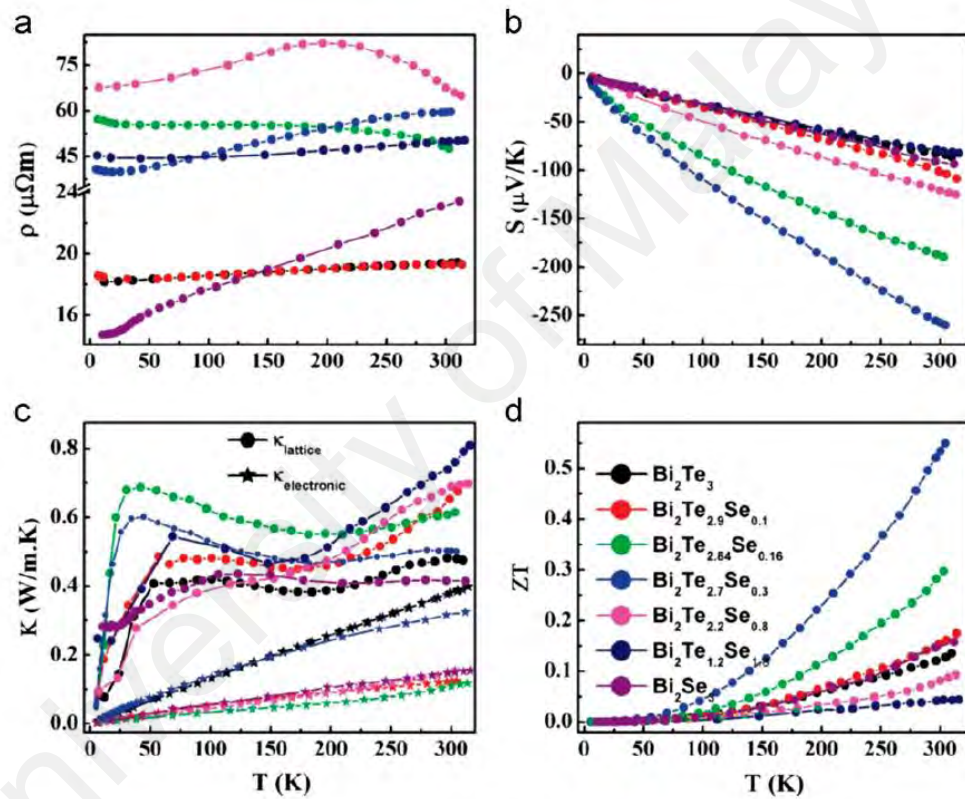


Figure 2.2: Nanocomposite strategy through nanoplatelet composite demonstrated by Sony et al., 2012 (a) electrical resistivity, (b) Seebeck coefficient, (c) thermal conductivity, and (d) figure of merit, ZT, (Soni et al., 2012).

Other methods which have been commonly used include: alloying and doping, promoting mass fluctuation strategy within bulk crystalline structure in Half Heusler materials, and, rattling strategy in complex cell structures of inorganic thermoelectric materials such as chalcogenides (Sevik & Cagin, 2011), clathrates (Nolas, Cohn, Slack, & Schujman, 1998), silicides (Cronin B. Vining, McCormack, Zoltan, & Zoltan, 1991),

and skutterudites (Jiyang et al., 2001). Some of these materials have made breakthroughs in thermoelectric performance due to the brilliantly employed strategies.

On the other hand, an alternative class of thermoelectric materials is emerging in the field of conducting polymers and organic semiconductors (OSCs) such as pentacene (Harada, Sumino, Adachi, Tanaka, & Miyazaki, 2010; K. Hayashi, T. Shinano, Y. Miyazaki, & T. Kajitani, 2011; Kei Hayashi, Takashi Shinano, Yuzuru Miyazaki, & Tsuyoshi Kajitani, 2011), poly(3-hexylthiophene) (Schilinsky, Asawapirom, Scherf, Biele, & Brabec, 2005) and poly(3,4-ethylenedioxythiophene):polystyrene sulfonate (PEDOT:PSS) systems (Günes, Neugebauer, & Sariciftci, 2007) due to their advantages in term of processability, low cost, abundance of raw materials, and flexibility. Currently, the benchmark for organic thermoelectrics was achieved by Kim et al. who reported a $ZT=0.42$ for PEDOT:PSS dedoped with a choice of solvents (G. H. Kim, L. Shao, K. Zhang, & K. P. Pipe, 2013). Nanocomposite mixtures of OSCs with either organic particles such as carbon nanotubes or ionic liquids have also been a strategy for improving the ZT value for OSCs. For example, Liu et al. has reported an enhancement in the thermoelectric performance of the PEDOT:PSS by inclusion of an ionic liquid, and achieved a maximum ZT value of 0.017 in their works (Liu, Xu, Lu, Yue, & Kong, 2012).

2.3 Thermoelectrics: Theory behind the Phenomena

The thermodynamics inequilibrium in terms of chemical potential and the gradient temperature are the main driving force in thermoelectricity. The chemical potential consists of chemical information and also an electrostatic expression. Hence, the theory of thermoelectric phenomena can be derived based on the behaviour of electrons across the periodic potential. Electrons are fermions, the particles that follow Fermi-Dirac distribution. From this interpretation, the correlation in electrical and thermal current densities can be written in term of Fermi-Dirac distribution. Lengthy derivations from the

Boltzman theory eventually lead to the famous Onsager's reciprocal relation, which is the very fundamental theorem behind thermoelectrics as follows

$$\textit{Electric current density, } \mathbf{j} = e^2 K_0 \mathbf{E} + \frac{e}{T} K_1 (-\nabla T) \quad (2.2)$$

$$\textit{Thermal current density, } \mathbf{q} = e K_1 \mathbf{E} + \frac{1}{T} K_2 (-\nabla T) \quad (2.3)$$

where ∇T is the temperature gradient, the electric field, \mathbf{E} is given as the negative gradient of potential difference, $-\nabla V$, e is the charge of the electrons, K_n is a second-rank tensor through the velocity of the wave (particles are moving with velocity, \mathbf{v}_k). The Boltzman transport equations are obtained and written as

$$\mathbf{j} = \sigma \mathbf{E} + \sigma S (-\nabla T) \quad (2.4)$$

$$\mathbf{q} = \sigma S T \mathbf{E} + \kappa (-\nabla T) \quad (2.5)$$

where the electrical conductivity, $\sigma = e^2 K_0$, the Seebeck coefficient is given as $S = \frac{1}{eT} \left(\frac{K_1}{K_0} \right)$ and the thermal conductivity, $\kappa = \frac{K_2}{T}$. A microscopic scrutiny on the derivation parts can be found elsewhere and have been described in details from relevant studies and sources (Mott, 1936; Onsager, 1931).

2.3.1 Generalised Description of Seebeck Coefficient

It has been shown earlier how, in metallic semiconductors, the Seebeck coefficient, electrical conductivity and thermal conductivity are very dependent on each other. This is due to the general Mott relation for thermopower, the expression shows how each parameter, such as Seebeck coefficient of a carrier in a freely independent scattering system is intimately related to the differential conductivity of the system. The electrical conductivity of the material is dependent on the density of states whilst the Seebeck coefficient is related to the differential conductivity, as in the following expression

$$\text{Differential conductivity, } \sigma = \int \sigma(E) dE \quad (2.6)$$

$$S = -\frac{k_B}{e} \int \left(\frac{E - E_F}{k_B T} \right) \frac{\sigma(E)}{\sigma} dE = -\frac{\pi^2 k_B^2 T}{3e} \left[\frac{d \ln \sigma(E)}{dE} \right]_{E_F} \quad (2.7)$$

where $\sigma(E)$ is called the differential conductivity with fractional contribution per electron with energy E to the total of conductivity, whilst E , E_F , and k_B is the energy of electron, Fermi level and the Boltzmann constant respectively. Mott's variable-range-hopping (VRH) model can describe thermally activated electrical transport at lower temperatures as the following

$$\frac{S}{T} = \frac{\pi^2 k_B^2 m^*}{(3\pi^2)^{2/3} \hbar^2 |e| n^{2/3}} \quad (2.8)$$

where m^* is the effective mass, n is the carrier concentration, \hbar is the modified Planck constant. Whilst electrical conductivity depends mostly on the available carriers, Seebeck coefficient is much more complicated than that. It exists as a result of the entropy due to the changes in chemical potential. By kinetic theory, Seebeck coefficient is defined as the energy difference between the average energy of mobile carrier and the Fermi energy. By increasing the carrier concentration, the average energy and Fermi energy is increased too. This eventually results in trade-off when improving the electrical conductivity of inorganic semiconductor materials through increasing carrier concentration. In conclusion, the rapid increase in Fermi energy than the average energy has caused the increased in electrical conductivity and the decrease in the Seebeck coefficient.

2.4 Thermoelectrics: Devices and Applications

To date, the commercial exploitation of thermoelectricity has only been found in the form of miniature Peltier devices for cooling which have been applied to automobiles, which cool the seats in vehicles built by luxury car manufacturers such as Rolls-Royce, Bentley, Ferrari and Lexus. Though, proven to be a success, the application to harness

thermoelectricity for use in solid state electricity generation devices are still short. On meeting realistic expectation, it has been pointed that, the ZT that has to be achieved in order to match the conventional coal or fuel based power generators ‘for at least a plausible application’ is approximately 2, as has been shown in Figure 2.3.

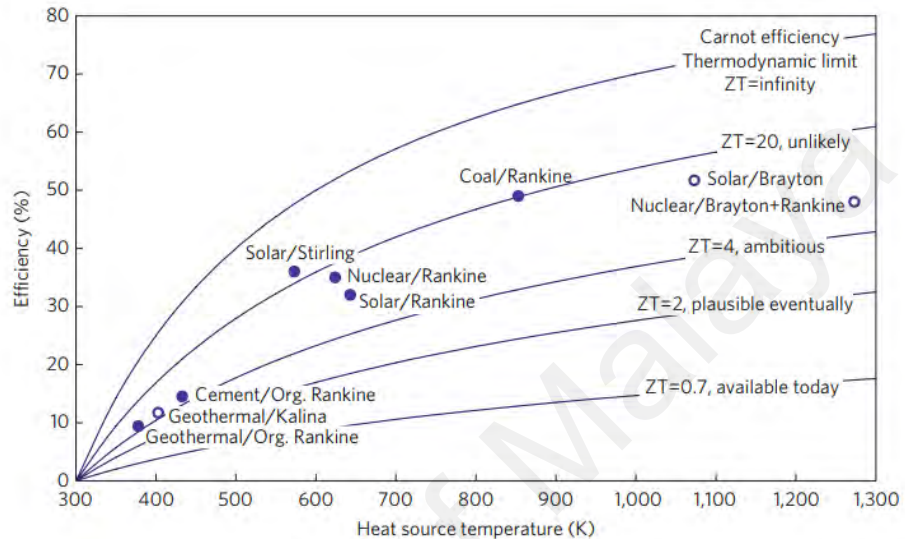


Figure 2.3: The estimation of thermoelectrics efficiency compared to the mechanical heat engines performance as assessed by Vining C.B., 2009 (Cronin B Vining, 2009).

However, this fact should not be the deterrence to stop the race altogether when the future need to be embraced optimistically. Efforts to commercialise thermoelectric generator (TEG) have been highlighted in various sectors such as automobiles and extra-terrestrial exploration as has been shown in Figure 2.4. Half-Heusler and Bi_2Te_3 segmented thermoelectric element was employed in Ford Fusion model. The typical power output of around 600 Watts for the same scale model has been demonstrated by BMW in 2011.



Figure 2.4: (left) Targeted TEG used for automobile, bypassing the exhaust of Ford Fusion, with 500 Watts capacity (Fairbanks, 2011). (right) The Mars Rover Curiosity with RTG operating between 100 to 125 Watts (Ritz & Peterson, 2004).

To cater TEG applications for a specific platform, the demand for power output from power generating solid state devices is divided in two categories; a) sub-Watts category powering up miniature, wearable and portable devices as summarised in Table 2.2, b) sub-kW category, for higher electrical requirements such as radioisotope thermoelectric generators (RTG). RTG was the largest power producer known among various thermoelectric energy conversion applications, as has been utilised by NASA in space exploration missions for over 30 years.

Table 2.2: Comparison of TEG modules for low power application

Modules	Open Circuit Voltage, mV	Load Match Optimum Power, μW	Power Density, $\mu\text{W}/\text{cm}^2$
Miniaturized thermoelectric generator for human body applications (Z. Wang, Leonov, Fiorini, & Van Hoof, 2009)	150	0.0003	≈ 0.00173
Flexible thermoelectric generator for wearable biometric sensor (Francioso et al., 2010)	160	0.00418	≈ 0.00019
Wearable headband (Leonov, Torfs, Vullers, Su, & Van Hoof, 2010)	-	2500	≈ 17
Seiko Thermic wristwatch (Paradiso & Starnier, 2005)	3000	30	≈ 26
Coin size coiled up polymer foil thermoelectric generator (Weber et al., 2006)	750	10	≈ 1.1
STEG in current work	0.0121	0.00827	≈ 5.5

2.5 Solar Thermoelectric Generator (STEG)

Solar radiation heating has been studied and applied in various applications, i.e. water heaters, driers, and air-conditioning. Recently, solar thermoelectric generators (STEGs) have been studied in order to utilize the energies, both light and heat from the sun (Chu & Majumdar, 2012; Y.-G. Deng & Liu, 2009; Giacoletto, 1959; Salman B. Inayat et al., 2012; Kraemer, Poudel, Feng, Caylor, Yu, Yan, Ma, Wang, Wang, Muto, et al., 2011; Thirugnanasambandam et al., 2010; Yang et al., 2011). This technology could potentially further enhance the efficiency of existing stand-alone solar based energy conversion devices by working in tandem (Y. Deng, Zhu, Wang, & Shi, 2013; Narducci & Lorenzi, 2016; Sweet et al., 2016).

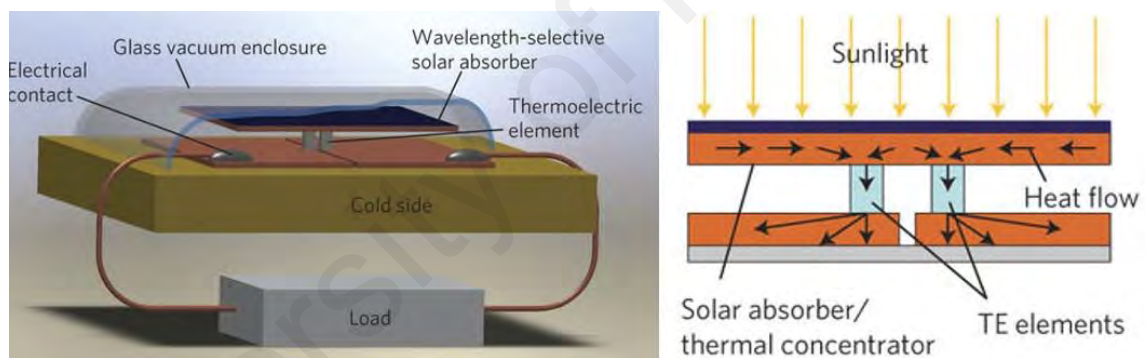


Figure 2.5: Structure of an STEG cell by Kraemer, 2011.

There are many different types of solar energy driven devices. Some of them are used to capture and store heat in the fluids which are then used in heat exchangers to provide hot water or in boilers to produce steam and get the turbines running. While some of them are used directly to harvest energy from the sun such as solar cells and STEGs. In devices such as flat plate collectors and solar concentrator, the sun radiation is used to heat up water or molten salt for water heating system or molten salt reactor, to store heat from the sun. Solar cells are used to generate electricity from the light energy which caused chemical reaction in photovoltaic devices. On the other hand, STEGs exploit the temperature difference generated between the indoor and outdoor building temperatures

on transparent glass walls and windows in order to generate electricity. To the author knowledge, none of the discussed STEGs in the literature was found to exhibit the ability of storing up heat for continuous use when night time has arrived. In this thesis, the author is trying to produce a conceptual work that the STEGs possessed such attribute that they are able to store heat and able to run continuously.

In the development of solar energy driven devices, the design and specifications are among the challenges facing by many engineers and researchers. In principle, the production of the devices should be a relatively easy and brief series of processes in order to prevent complex procedures whilst at the same time reduces cost. However, this was found to be difficult to achieve. For specific application such as STEGs, in order to maximise the absorption of heat radiation, the STEGs' design must include a certain mobility function to reroute the exposed surface of the STEGs facing directly to the sun; maximising the performance output of the devices. Thus, the STEGs must be placed on a moveable panel like device with solar tracking system that has been widely demonstrated in solar cell panels. This specific function adds an order of complexity in the design process of STEGs. The designs which were previously studied have included external systems such as solar absorbers in order to collect heat from the sun to run STEGs (Kraemer, Poudel, Feng, Caylor, Yu, Yan, Ma, Wang, Wang, Muto, et al., 2011; Yang et al., 2011).

In another design, to maximise the exposed surface area of STEGs, it was suggested that the STEGs to be mounted on the glass walls and windows of the buildings. This is to allow heat on the external and cooling on the internal sides. For this purpose, the materials selected for the whole STEGs architecture should comprise of either fully- or semi-transparent materials to prevent an obstructed sunlight path. Likewise, transparent electrodes need to be employed in a large area architecture for STEG application such as

atomically thin sized layer made of gold and graphene. The active materials of the devices are usually made of thin films structure which is then cut and etched onto to form multi junctions. Thin films are easily fabricated by using sputtering, printing and vapour deposition growth technique to produce thin film material which serve as the multi junctions in the devices. As part of the improvement in the properties of the materials, Inayat et al. has designed thermoelectric pillars to integrate with the thin film matrix by embedding the nano-structured components into them (Salman B Inayat, Kelly R Rader, & Muhammad M Hussain, 2012). This is an interesting approach for boosting the performance of inorganic materials.

2.6 STEG Device Modelling

A number of models have been proposed in order to simulate the performance of the thermoelectric devices. The performance of the device which includes the current distribution or potential difference, and heat transfer analysis are among the parameters that are taken into consideration when subjected to modeling works. Heat transfer analysis is important because thermoelectric studies usually dealt with materials with temperature dependent properties. In simulation works, neglecting this in mind could potentially overestimating the performance of the simulated devices. The studies showed that the effect of implementing coupling of temperature field and electric potential field in 3D numerical modeling to the performance of thermoelectric coolers produced significant difference compared to the thermally independent model. The simulated device with constant properties of the materials over varying temperatures has overestimated the cooling capacity of the device. Studies by X.-D. Wang et al. has shown that the predicted result contained significant error when the simulated model with temperature dependent properties was not applied. In addition, the interconnector properties were also taken into account to produce realistic results.

Comparison between modeling in zero-dimensional model and model with greater dimension than one, the computation of the 3D model is more accurate as the solver are able to evaluate the required calculation at different points along the dimensional hierarchy as opposed to zero dimensional model which only treats the calculation at equilibrium basis and simplifying assumption. Such as, in zero-dimension models, the calculation is only performed at both hot and cold ends of the thermoelectric junction analytically without taking consideration the differential distribution activities in between.

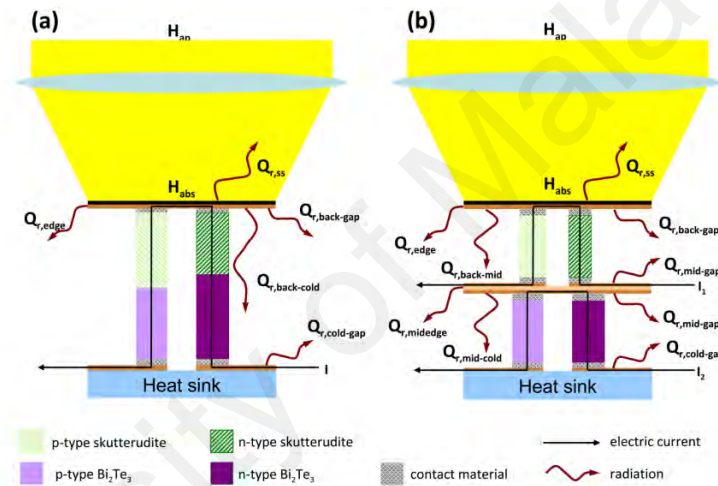


Figure 2.6: The architecture and boundary conditions of segmented (a) and cascaded (b) STEGs modeled by McEnany et al., 2011(McEnaney, Kraemer, Ren, & Chen, 2011).

Various solar thermoelectric generator models have been developed over the years, through a range of approach. Thermodynamic studies were conducted by Chen, numerical model for skutterudite based materials was modeled by Scherrer et al, Omer and Infield performed computation with improved theoretical model that considered all aspects of heat transfer's parameters that influencing the computation results. Yang et al developed a model of similar device foundation by these theoretical studies in order to optimize further the solar thermoelectric device. In the improved model, heat losses to surrounding due to conduction, natural convection and radiation were also considered. At the position

where the insulated boundary condition was applied, it was found that the heat loss could still pass through the insulation, but with very minimal loss as opposed to model with no insulation. This model predicted that the best solar thermoelectric device (STED) design should consist of insulation compartment to prevent losses from conduction and convection, and also low emissivity coating cover to prevent radiation losses. Contact resistance was also found to inversely affect the model's output power.

Seetawan et al. and Kraemer et al. have demonstrated TEG device modeling and optimization studies (Kraemer, Poudel, Feng, Caylor, Yu, Yan, Ma, Wang, Wang, & Muto, 2011; Seetawan et al., 2012). They found that the increased length of TEG legs produced higher power output, until an optimum length has been reached and the power diminished. In both studies, the surface area and volume have been fixed whilst the length is varied. Kraemer et al. highlighted that the power output is independent of the volume of the TEG legs. This high-performance power output is associated with the ability of the TEG junction to retain heat at the hot side longer whilst slowly being transmitted to the cold side. Therefore, proving the role of thermal conductivity in enhancing the power output. This also means, in miniaturized devices, when the length of TEG legs is constrained to a fixed small value, selection of materials with low thermal conductivity is a necessity.

2.7 Conducting Polymers and Organic Semiconductors

Conducting polymers and organic semiconductors are explored in this work as candidates for STEG application due to their tuneable thermoelectric properties. The emerged trend in improvement of the figure of merit, ZT as shown in Figure 2.7 was primarily due to understanding how different approaches could improve the thermoelectric properties. In maximising ZT , an increase in both electrical conductivities and Seebeck coefficients of the materials, and at the same time a reduction or constant

thermal conductivities are required. An important note on this, due to the weak correlation between electrical conductivities and Seebeck coefficients in polymer materials and organic semiconductors, most CPs and OSCs will not obey Wiedemann-Franz law.

Early works have found that the electrical conductivity could be significantly increased by using iodine as the dopant (Hiroshige, Ookawa, & Toshima, 2007). Electrochemical dopant has also been used by mixing or soaking polymeric materials in salt solutions or electrolytes (Datta et al., 2015). Another technique has demonstrated that by using different solvents in subsequent order when preparing the polymer materials, has also been found to increase the Seebeck coefficient whilst sacrificing the electrical conductivity, this technique is called dedoping (H. Park et al., 2014). This technique is used in order to remove potentially non-ionised dopants to improve the carrier mobility. The optimisation approach by Kim et al. in their works have resulted in organic thermoelectric materials with ZT of 0.42 (G. Kim, L. Shao, K. Zhang, & K. Pipe, 2013). Hybrid materials which focusing in embedding nanostructured materials such as nanorods and nanowires have created various composite materials including semi-metallic polymer composites which not only strengthening their mechanical properties, at the same time improving their electrical conductivities. Similar trend of additives mixing has been found to work in some of inorganic materials, but for inorganic materials, optimum thermoelectric properties is difficult to achieve. As they follow such that an increase in electrical conductivity will tend to decrease its Seebeck coefficient and increase its thermal conductivity, which is not the combination that is desired in order to obtain optimum ZT in thermoelectric applications.

On the other hand, tailoring thermoelectric properties in polymer materials was found to be easier. Whilst the thermal conductivity is readily low to begin with, an effort to increase their electrical conductivity or Seebeck coefficient has been proven rather

hopeful due to the weak correlation between the electrical conductivity, the Seebeck coefficient and the thermal conductivity. The fundamental theory behind this will be described in the latter section.

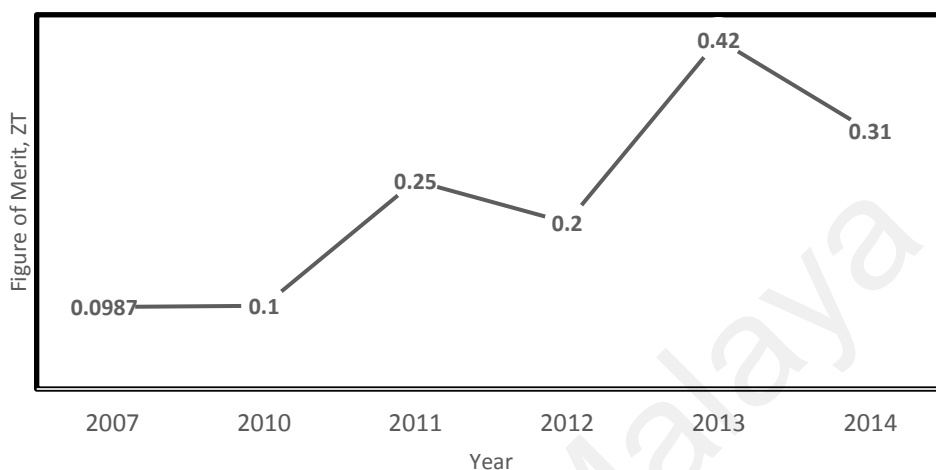
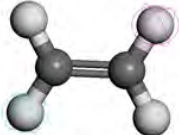

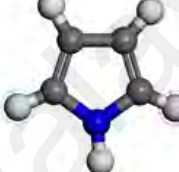
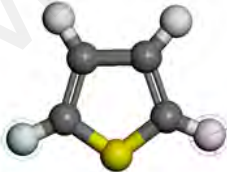

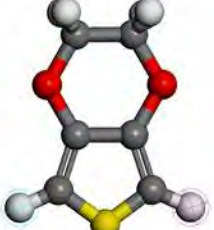


Figure 2.7: The progress in thermoelectric studies in conducting polymers and organic semiconductor materials according to their figure of merits.

As examples, the following polymers have been used in thermoelectric investigations; polyaniline (PANI)(Li, Tang, Li, Yan, & Zhang, 2010; Yoon, Reghu, Moses, Cao, & Heeger, 1995), poly(*p*-phenylenevinylene) (PPV) (Maddison, Unsworth, & Roberts, 1988; Sato, Yamaura, Hagiwara, Murata, & Tokumoto, 1991), polyacetylene (PA) (Kaneko, Ishiguro, Takahashi, & Tsukamoto, 1993; Y. W. Park et al., 1989), poly(2,7-carbazolenevinylene) (Lévesque et al., 2007; Lévesque et al., 2005), and poly(2,5-dimethoxyphenylenevinylene) (PMeOPV) (Hiroshige, Ookawa, & Toshima, 2006). Some of these polymers are shown in Table 2.3. These polymers are chosen due to their conductive nature. Different types of polymers show different electrical conductivities, thermal conductivities, figure of merits and exhibit various TE performances. The frontrunner in the conductivity performance of conducting polymers are poly(3,4-ethylenedioxythiophene) (PEDOT), which, when doped with polystyrenesulphonate (PSS) or tosylate (Tos) may achieve conductivities of up to 3000 S/cm(Xia, Sun, & Ouyang, 2012).

Table 2.3: Examples of polymer monomer which are commonly researched in various electronic applications, i.e. thermoelectrics, solar cells, OLEDs and OTFTs

Name	Structure
Polyacetylene	
Polyaniline	
Polypyrrole	
Polythiophene	
Poly(3-methylthiophene)	
Poly(3,4-ethylenedioxythiophene) PEDOT	

2.7.1 Electronic Properties of Conducting Polymers and Organic Semiconductors

Synthesis and fabrication methods of CPs and OSCs is very important in order to deliver materials that can perform for specific applications such as STEG. The yield and the basic functionality of the materials depends on the method used, solvent, pH and temperature during synthesis as shown in Figure 2.8.

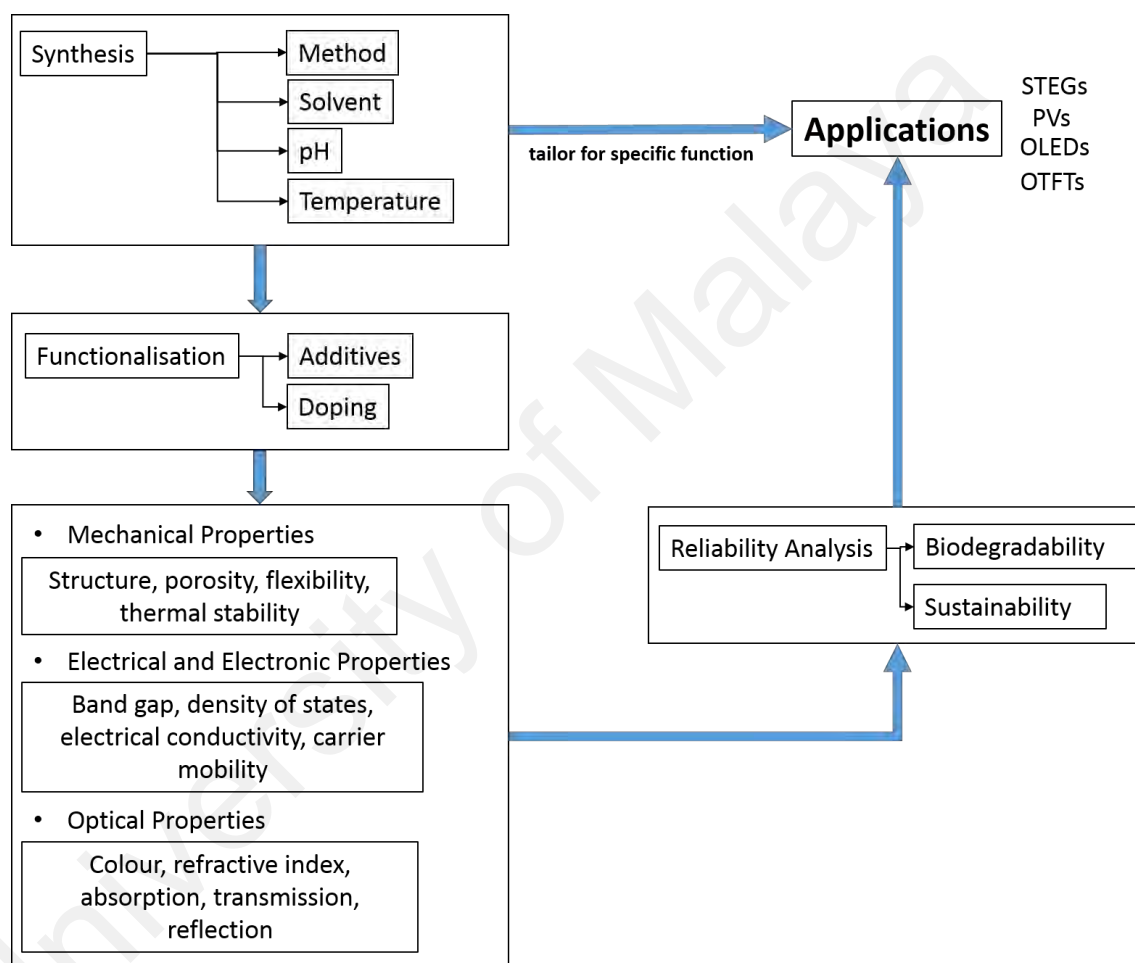


Figure 2.8: Route map of research in the field of conducting polymers and organic semiconductor materials.

Functionalisation of the synthesised polymers and organic materials is important for enhanced mechanical, electrical and electronic, and optical properties. Doping can be used to enhance intrinsic electrical conductivity and also to create semiconductors of different types (n and p). Doping is performed by introducing very small amount of conductive materials (dopants) into polymer or organic materials blends. Additives are

largely used in order to improve thermal and optical properties. The amount of dopants and additives are usually tuned to desired functionality for specific application.

2.7.2 Charge Transport Mechanisms in CP and OSC Materials and their TE Behaviours

2.7.2.1 Band Conduction

In semiconducting polymers and small monomers/oligomers type of molecules, the mechanism of charge transport may be facilitated by band conduction, charge hopping and ionic transport. Band conduction and charge hopping is normally occurred in the doping system particularly in organic-inorganic systems, in which the shifting in potential energy will lower the fermi level to assist the jump or transfer of electrons or holes from a localised orbital. Insulators are typically separated by a large gap from the conduction band. This is the reason for very low electrical conductivity in insulators. In metals, the valence and band and the conduction band are overlapped, thus the electrons in valence band can move freely in metals. This also explains the reason for lower Seebeck coefficient in metals, as the difference in the carrier energy and the Fermi energy is very small. Band conduction is emphasised in metallic semiconductors due to tunable thermoelectric properties by optimising the concentration of the dopant in order to tune the difference in the carrier energy and the Fermi energy, maximising Seebeck coefficient and thermoelectric power. Thermal and optical excitations are the driving force to bridge the gap between the valence and conduction bands in semiconductor materials.

The Seebeck coefficient expression which has been derived from Mott relation indicated the dependency of Seebeck coefficient to the electrical conductivity as follows

$$S = -\frac{k_B}{e} \left[\frac{E_C - E_F}{k_B T} + A_C \right], n - type semiconductor \quad (2.9)$$

$$S = \frac{k_B}{e} \left[\frac{E_F - E_V}{k_B T} + A_V \right], p - \text{type semiconductor} \quad (2.10)$$

The dimensionless parameters denoted as A_C and A_V are constants that account for the asymmetric distribution in energies of charge carriers around the conduction and valence bands. These expressions represent the correlation for Seebeck coefficient when metallic or band conduction occurred.

2.7.2.2 Hopping Transport

The polarons or bipolarons localised from one pi orbital to another due to the interaction with phonons-assisted carrier hopping have been responsible for charge transport in CP and OSC materials. The charge site which consist either a polaron or bipolaron interacted elastically with phonons, so that they can delocalised along the conjugated double bond in the backbone of the long chain polymers or the ring of the aromatic molecules. Various hopping theories have been described and the concept of transport energy, E^* , has been introduced. In CP and OSC materials, it was found that this transport energy level within the disordered density of states that has enabled conduction within the materials. The following expression is derived from Boltzman transport equation

$$S = -\frac{k_B}{e} \int \left(\frac{E - E_F}{k_B T} \right) \frac{\sigma(E)}{\sigma} dE = \frac{k_B}{e} \left(\frac{E_F - E^*}{k_B T} \right) \quad (2.11)$$

The independency of the above expression to any energy level beyond or below of the conduction and the valence bands has indicated that by tuning the carriers edge band level (Fermi and electron energy level) via doping of CP and OSC materials, the tuning of these energy levels will not affect the Seebeck coefficient in a negative way.

Another factor that was found to affect hopping transport in CP and OSC materials is the molecular weights of the polymers. Kline et al. (Kline, McGehee, Kadnikova, Liu, & Fréchet, 2003) found that an increase in chain length and molecular weight leads to the increase in electron mobility due to the fundamental mechanism of electrical conduction in polymers, through electron hopping along the polymer backbone. A high molecular weight polymer will promote the charge carriers to move through longer distances before hopping to another chain. The decrease in the hopping could result in an increased mobility. Also, longer chains give carriers more opportunities for hopping to neighbouring chains. Thus, the polymer samples and their molecular weights can be correlated with their electron mobility. Also, the thermal conductivity of polymer increases with the increase of polymer chain length as has been shown by Zhao et al (J. Zhao, Jiang, Wei, Zhang, & Rabczuk, 2013; J. Zhao, Nagao, & Zhang, 2010).

2.7.2.3 Ionic Conduction

Another possible strategy in order to increase the electrical conductivity of CP and OSC materials is by adding solvent into them to change their morphology. This addition is enhanced by the addition of ionic thermodiffusion molecules (electrolyte solution) to produce mixed ionic-electronic conductors. Electrolyte is normally prepared by adding macromolecular sized solvent dissolving low molar mass ions will assist ionic conductivity due to loosely bond ions, i.e. in electrochemical system and electrochemically conducting polymer. Seebeck coefficient from several hundreds up to few mV K^{-1} were produced through conduction transport of ionic type as demonstrated by Jiao et al. (Jiao et al., 2017). The ZT of a polyelectrolyte mixed with composite made of nanofibrillated cellulose were found to be 0.025 at room temperature. The mixture produced Seebeck coefficient higher than the pristine composite, whilst maintaining its electrical conductivity. This study opens up possibilities for ionic thermoelectric field in term of mass fabrication for large area production of ionic thermoelectric materials.

2.7.2.4 The Effect of Temperature

As a semiconducting polymer, the electrical conductivity increases with increasing temperature (Bubnova et al., 2011; Hewitt et al., 2013; Yue et al., 2012). This is because when the temperature increases, the electron that are charge carriers in the conductor will gain energy and jump up into higher energy levels. However, these energy levels are all still in the valence band. Thus, the number of charge carriers will not change for a conductor with an increase in temperature. On the other hand, the charge on each carrier and the electric field strength are independent of the temperature. Different types of polymers have known to demonstrate temperature-dependent electrical conductivity.

2.8 Liquid Crystal Materials

Crystals, consists of highly ordered atoms, liquids, consists of less ordered molecules, liquid crystals, a semi state between the two condensed matter phases. Liquid crystal materials are consisted of molecules which exhibit positional and orientation order in crystals, however they diffuse randomly in liquids when isotropic or melting temperature is reached. LC is categorised as a type of organic semiconductor (OSC) materials. It has many different structures and further classified under different names, such as nematic, smectic, ferroelectric and discotic liquid crystals as classified in Figure 2.9. Nematic, smectic and ferroelectric liquid crystals are categorised as Calamitic LCs. They are rod like molecules with elongated shape in their length, which the size is significantly greater than the molecules breadth. Alignment control techniques for calamitic liquid crystals are required. This is to optimise the performance of LC devices by controlling the orientational position of LCs. Among the techniques used to control the alignment of LCs are mechanical rubbing, external field effects, and phot-alignment techniques.

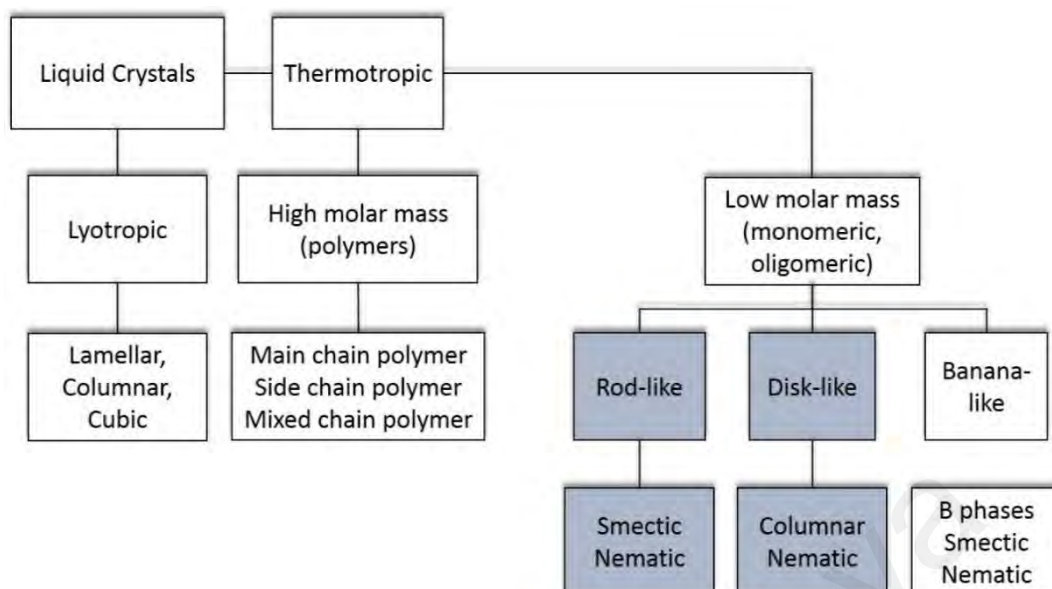


Figure 2.9: Different classes of liquid crystals.

Depending on the structures and functionalisation, they are used in different applications. Calamitic liquid crystals as shown in Figure 2.10 are commonly used in display technologies. Meanwhile, a subcategory of aromatic organic molecule such as discotic liquid crystals are used in OLEDs, OFETs and solar cells where efficient charge transfer is required in such applications. The mesogens of liquid crystals can be further classified into two; enantiotropic: forming thermodynamically stable mesophases during both cooling and heating, monotropic: metastable mesophase due to mesophase transition occurrence during cooling cycle from isotropic liquid phase (below the melting point). Driving force parameters for mesophase formation are geometric anisotropy, interaction anisotropy, self-assembly, self-organisation and microsegregation (Kumar, 2016).

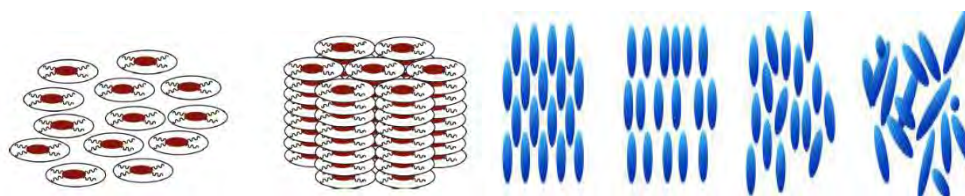


Figure 2.10: The organization of self-assembled LCs. (left) DLCs. (right) Calamitic LCs.

The self-assembly alignment in thermotropic liquid crystals is achieved intrinsically during transition phase as feedback response to temperature. The thermotropic liquid crystals organised themselves into various liquid crystalline phases when the temperatures of the molecules are being manipulated. This intrinsic behaviour is superior when compared with polymers with long chains of backbones. The polymers tend to orientating themselves randomly in order to fill in the space with their long chains, although realignment is possible through manufacturing efforts.

2.8.1 Polymer Electrolyte Liquid Crystals (PELCs)

In the past, polymer electrolytes have long been used in applications such as lithium ion batteries, fuel cells, and dye sensitized solar cells (DSSC) (K. F. Chen, Liou, Lee, & Chen, 2010; Gottesfeld & Zawodzinski, 2008; Manuel Stephan, 2006). A few works have explored the use of liquid crystals as a plasticizer in polymer electrolyte systems for DSSCs (M. Wang et al., 2011). However, an effect of the liquid crystal on the electrical conduction mechanism of the PELC mixture has not been elucidated in prior investigations. In this thesis, polyvinyl alcohol (PVA) was used as the polymer matrix. The liquid crystal doped to PVA was 4-Cyano-4'-pentylbiphenyl (5CB), a rod-like polar molecule as shown in Figure 2.11 (a).

The 5CB was selected due to its function as a plasticizer, typically, favored to be a highly polar molecule. As shown in Figure 2.11 (b), the 5CB has a dipole moment along the longitudinal axis. The polarization within the 5CB can induce electron-hole pairs in the PVA close to the 5CB, and electron and/or hole carriers may transport in the PELC mixture. The general phase transition diagram of 5CB is illustrated in Figure 2.11 (c) (Singh, 2000). Below the crystalline transition temperature of 18 °C, the 5CB acts like a normal crystalline solid. It only possesses one liquid crystal subphase, which is the nematic phase between 18 °C and 35 °C.

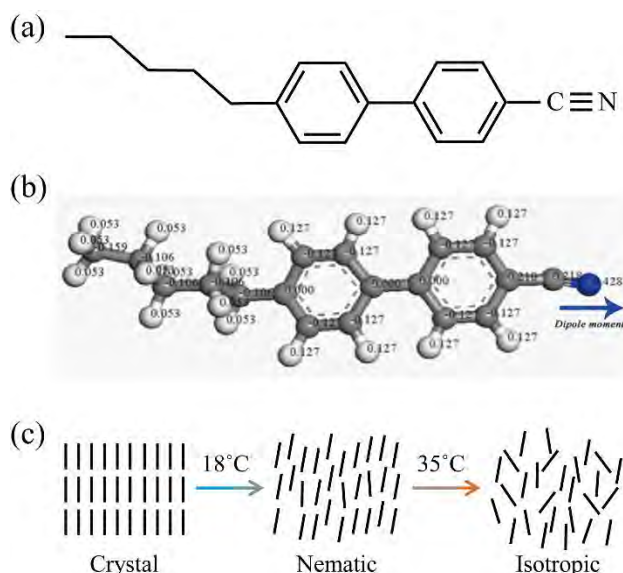


Figure 2.11: (a) Schematic representation of a 5CB molecule. (b) Dipole mapping of the 5CB molecule. There is a strong dipole moment along the longitudinal axis of the molecule. (c) Phase transition diagram and the temperature of the 5CB, represented by each small bar.

In the nematic phase, the liquid crystal shows a high degree of orientational order. Above the transition temperature of 35 °C, it enters the isotropic phase and loses its orientational order. Thus, embedded nematic LCs in polymer matrix is supposed to be able to guide the charge transport efficiently along the backbones of the polymer besides at some extent provide better alignment. It is believed that the strategy of maximizing the performance of electrically conducting organic semiconductors such as LCs and polymers depends on the organization of the materials structure. This can be done through enhancing their crystallinity (Du et al., 2012; G. H. Kim et al., 2013).

2.8.2 DLC as Organic Semiconductors

Discotic liquid crystals (DLCs) are relatively a new generation of organic semiconductors which are promising in various electronic and optoelectronic applications such as optical lasers, light emitting diodes, field effect transistors, and photovoltaics (Kaafarani, 2010; Schmidt-Mende et al., 2001; Sergeyev, Pisula, & Geerts, 2007). The growing interest in DLCs studies is associated with the advantages of the material's self-

healing ability to self-assemble into 1D- or 2D-positional and/or orientational order which can significantly enhance their electronic properties. DLCs typically stack to form columnar structures, and the π conjugation in the DLC's aromatic core allows π electrons transfer along the column's longitudinal axis. Thus, the charge transfer in DLCs can be considered as in 1D-nanowires. This quasi-1D transport property is exploited in many electronic and optoelectronic applications (N Boden et al., 1995; Chandrasekhar & Balagurusamy, 2002; Lemaure et al., 2004).

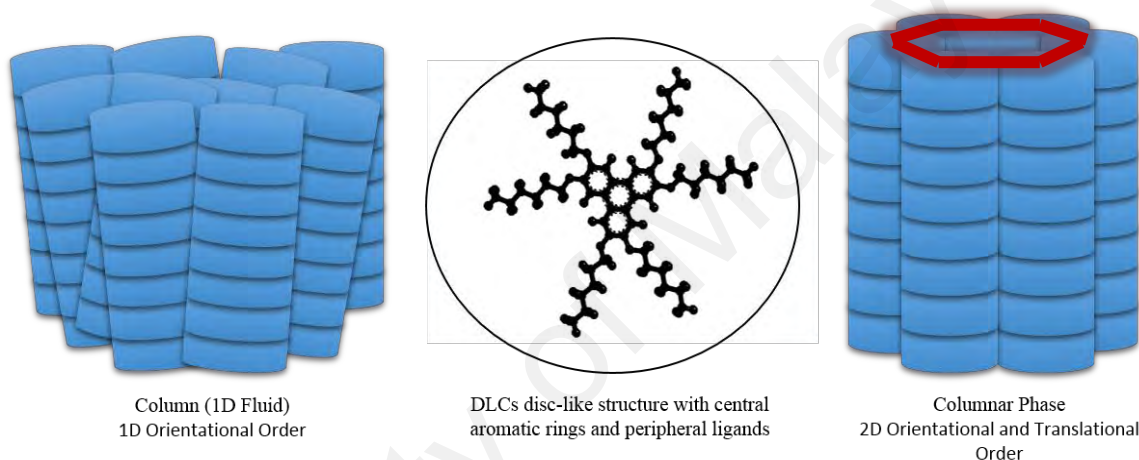


Figure 2.12: Illustration of the quasi-1D and -2D of stacking DLC disc-like molecule.

Molecular structure of DLCs comprises of rigid aromatic core and flexible peripheral chains as shown in Figure 2.12. These structures govern the physical properties of the materials such as the temperature of the phase transition. The transition temperature of DLCs from crystalline (Cr) phase to columnar liquid crystalline (D_h) phase and columnar liquid crystalline phase to isotropic (Iso) phase is lowered with longer alkyl chains. The phase transition of DLCs is widely studied by using digital scanning calorimeter (DSC) and polarizing optical microscope (POM). A fan shaped structure is observed under POM by using cross polarizer when hexagonal columnar structure is formed. This optical pattern is the result of the interlayer movement of the stacking molecules (Nandi, Singh, Singh, & Singh, 2013).

Generally, larger polyaromatic cores give rise to more stable stacking of the discs in stable columns. Due to the relative rigidity of the columnar stacks, the carrier mobility in D_h phase is enhanced compared to the Cr and Iso phases as a result of overlapping and interacting π^* orbitals (N Boden et al., 1995). Aromatic cores of triphenylene molecules provide a flexible platform from which DLCs can rearrange themselves into hexagonal columnar mesophase (π^* - π^* stacking configuration with cofacial distance of 3.5 Å) between 70 °C and 100 °C (Haverkate et al., 2014; Mulder et al., 2003). Extensive studies of charge mobility measurement are carried out by time of flight (TOF) or pulse radiolysis-time resolve microwave conductivity (PR-TRMC) experiments. Time of flight method utilises photoconductivity as a measure of charge mobility when the samples are irradiated with laser. This will induce a charge separation. The charge transit is measured in the function of photocurrent detected from electrons and holes. In PR-TRMC measurement, a nanosecond ionizing laser pulse is irradiated on the DLC samples with known uniformed concentration to induce the charge separation. However, PR-TRMC has disadvantage on overestimating the measured charge mobility as the measurement is insensitive to the type of charge during measurement (Said, Mahmood, Daud, Mohd Sabri, & Sairi, 2016; Sergeyev et al., 2007). It has been shown that the carrier mobility of 2,3,6,7,10,11-hexakis(hexyloxy)triphenylene (HAT6) increases over the materials transition in the D_h phase up to $7 \times 10^{-4} \text{ cm}^2 \text{V}^{-1} \text{s}^{-1}$ (Neville Boden et al., 1995; Kreouzis et al., 2000). An even higher mobility measured by TOF in the order of $10^{-1} \text{ cm}^2 \text{V}^{-1} \text{s}^{-1}$ was seen in larger polyaromatic hydrocarbon such as hexabenzocoronene and phtalocyanine was also reported (Sergeyev et al., 2007). In addition, ultraviolet photoelectron spectroscopy (UPS) has been used in order to investigate the energy gap and molecular orbital of DLCs. Characteristics of structural order or disorder that improve the electronic properties of DLCs have been studied by using wide angle X-ray diffraction, XRD.

Columnar stacks arrangement in DLC system allows the 1D charge migration which lead to quasi 1D electrical conductivity. The order of electrical conductivity varies from molecule to molecule. This attribute depends on the size and the type of atom located in the molecule. Electrical conductivity in the range of 10^{-10} - 10^{-14} S/cm have been reported in phthalocyanine discotic liquid crystal derivatives (Kumar, 2016). Significantly higher order of electrical conductivity has also been reported in triphenylene discotic liquid crystal derivatives in the range of 10^{-3} - 10^{-9} S/cm (Kumar, 2016). Higher electrical conductivity of discotic liquid crystals is achieved by heat treatment, doping the sample with molecules containing acceptor or donor atom such as TNF, AlCl_3 , F_4TCNQ , NOBF_4 , and strategic mixing of binary mixtures to promote a complementary polytopic interaction (cpi) in DLC systems (Kumar, 2016).

2.8.3 Electronic and Charge Transport Properties of DLCs

As shown in Figure 2.13, the stacks on discotic liquid crystal materials such as triphenylene, hexaazatriphenylene, hexaazatrinaphthylene, hexabenzocoronene was known to facilitate the inter-molecules charge transport so that high charge mobility can be established in these materials. Improving electrical and electronic properties of these materials could help broadened the utilisation and application of organic materials inspired electronic devices. There are number of factors known to help improving charge mobility in discotic liquid crystals for instance the size of the cores of the molecules, binary polytopic mixtures and strategic doping. These strategies are helping to increase the charge mobility of discotic liquid crystal materials by ensuring the stability of columnar stacking structure of the materials and systematically enhancing the charge transport among appropriate donor and acceptor molecules and π^* orbitals in the aromatic cores.

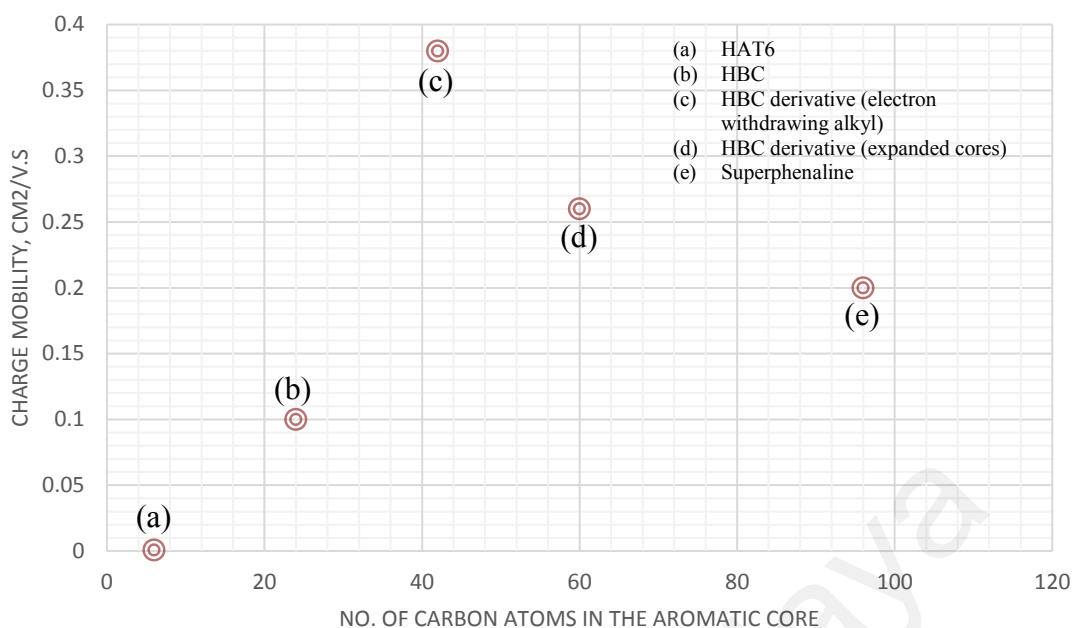


Figure 2.13: Dependence of number of Carbon atoms on the charge mobilities of several DLC materials (HAT6= triphenylene, HBC= hexabenzocoronene).

2.8.3.1 Doping of DLCs

Discotic liquid crystals exhibit a quasi-one-dimensional conductivity when the disc-like molecules stacking on top of each other, the pile behaving like a nanowires conductor, transporting electrons through pi orbitals. As in organic semiconductors and polymers, the conductivity property can significantly be enhanced by doping method with donor or acceptor materials. Band matching strategy by employing the Donor molecules (DLC) and Acceptor molecules (salt) of matched energy levels can improve doping efficiency as shown in Figure 2.14.

The electrical conductivity and charge mobility of various discotic liquid crystals such as hexabenzocoronene, phthalocyanine and triphenylene based discotic liquid crystals have been studied widely. Hexaalkoxytriphenylene doped with NOBF₄ has shown an increase in electrical conductivity from the transfer of rich electron molecules to the acceptor molecule. Hexabenzocoronene was oxidized by NOBF₄ and functionalized with electron acceptor molecule such as TNF was observed to exhibit similar improvement.

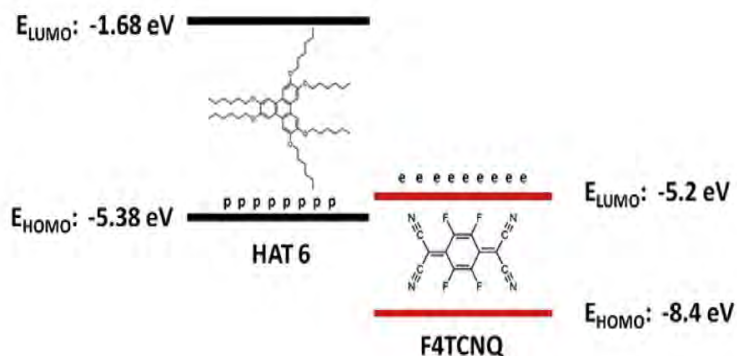


Figure 2.14: Band matching strategy between HAT6 molecule and F4TCNQ dopant molecule (Khan et al., 2016).

Increase in photoinduced charge mobility in HHTT by doping with iodine or TNF was observed. With addition of small amount of TNF, the electrical conductivity of HHTT was observed to increase by a factor of 10^7 . Ferrocenium cation from FcTFB combined with ferrocene ion uniquely formed a donor-acceptor (DA) system which strengthened the molecular stability and allowing the electron to be transported not only in the column but interacting with another column, thus increase the electrical conductivity of the materials. Balagurusamy et al., has doped HHTT samples with TNF. From their observation, large amount of dopant was required in order to observe dramatic increase in electrical conductivity measurement. The measured electrical conductivity reaches 10^{-2} S/m (Balagurusamy et al., 1999). Vaughan et al., conducted DC conductivity measurement of HHTT, doped iodine (saturated) (Vaughan, Heiney, McCauley Jr, & Smith III, 1992). The electrical conductivity was found to be increased, four to five orders of magnitude. It was discovered that non-planar dopant occupied spaces between columns, the aliphatic chains will give some room to adjust the position of the dopants. The charge transfer also occurs between columns due to the inter-columnar position of the dopants. This structural observation could provide better strategies when selecting the type of dopants so that they are compatible with the host materials.

The formation of charge transfer complex with the addition of ferrocene and ferrocenium cation, an electron donor and electron acceptor molecules, was evident by

the shifting of the peak observed in the UV-Vis spectrum in the visible range. In addition, the difference in ionic conductivity and electronic conductivity was identified by two different electrical conductivity measurements; namely AC and DC electrical conductivity measurement (Boden, Bushby, & Clements, 1993, 1994). AC conductivity measurement corresponds to the ionic charge transport whilst DC conductivity corresponds to the electron hopping transport. Boden et al., measured the frequency dependent AC conductivity, HAT6 doped AlCl_3 , the conductivity was independent of frequency at low frequencies, however was found dependent at high frequency. The conductivity was also increase 10^3 times greater when measured parallel to the column axis compared to perpendicular axis, due to the nature of hopping behaviour of charge carriers along overlapping orbitals.

2.9 Temperature Dependent Measurement Techniques for TE Materials

In this section, several commonly used temperature dependent measurement techniques are reviewed and discussed. Table 2.4 has tabulated several relevant references; a) (Zhang, Zhang, & Wang, 2013), b) (Kim, Hwang, & Woo, 2012), c) (Lu, Song, & Wang, 2013), d) (L. Wang, Wang, Zhu, Li, & Pan, 2011), e) (Moriarty et al., 2013). This aspect of knowledge is important in order for one to select which technique is suitable for characterisation of different types of samples: (i) understanding the fundamentals and procedures of measurement techniques, and the limitations for each measurement method. (ii) the forms, geometries and sizing for a particular measurement technique. (iii) how error is affecting the analysis and determine where the error is originated from. It has been proven difficult to achieve low error in measurement due to the radiative and convective losses. These effects has been discussed in some measurements (Borup et al., 2015; D. Zhao, Qian, Gu, Jajja, & Yang, 2016).

Table 2.4: A summary of the measurement method and apparatus used in thermoelectric performance measurement for conducting polymers and organic materials with carbon particle based composites

Polymer	Additive	Nanofiller	Preparation Method	Electrical Conductivity (S cm ⁻¹)	Seebeck Coefficient (μV K ⁻¹)	Power Factor (μW m ⁻¹ K ⁻²)	Thermal Conductivity (W m ⁻¹ K ⁻¹)	ZT
PEDOT [a]	PSS	rGO (21 wt %)	Mixing	715.03 4-point probe Keithley 2400 and 2182A Nanovoltmeter	22.9 Derived from the slope of V-T curve	32.4	~0.2 Netzsch LFA 447	0.067 at 300 K
PEDOT [b]	PSS	Graphene (2 wt%)	Solution spin coating	32.13 HMS-3000 Hall Effect Measurement System	58.77 Apparatus fabricated by Fraunhofer IPM	11.09	~0.14 Modified transient plane source technique (C-Therm TCi thermal conductivity analyser)	0.021 at 300 K
PANI [c]	HCl	GNs (30 wt %)	In situ chemical polymerisation	38 ZEM-3	26 ZEM-3	2.6	0.6 Netzsch LFA 457	1.95x10 ⁻³ at 453 K
PANI [d]	HClO ₄	Graphite (50 wt%)	Mechanical ball milling and cold pressing	120 ZEM-2	18.66 ZEM-2	4.18	1.2 Thermal conductivity tester KY-DRX-RW	1.37x10 ⁻³ at 393 K
PEDOT [e]	PSS	SWCNT	Liquid-phase exfoliation/film	4000 at 95 wt% 4-point probe Keithley 2000 Multimeter	14-26 Derived from the slope V-T curve Keithley 2000 Multimeter	140 at 85 wt%	0.4-0.7 Netzsch LFA 447	0.03 at 300K

2.9.1 Electrical Conductivity

Electrical conductivity is formulated from the resistivity of the materials; it inversely correlated to the resistivity. Resistivity depends on the free electrons or holes densities and their mobilities respectively. The most commonly method used to measure the semiconductor resistivity is by using four-point probe. As shown in Figure 2.15, normally the four-point probe measurement is considered as the absolute measurement when the resource for standard calibration is not available, for example measuring resistivity of new materials in confidence. Four-point probe method is always used in comparison to the two-point probe method. In comparison, although two-point probe is rather easy to implement, the interpretation of the measured data is more difficult. The measurement by

using two-point probe is lacking in term of its accuracy due to the parasitic voltage that exist due to wire resistance and contact resistance.

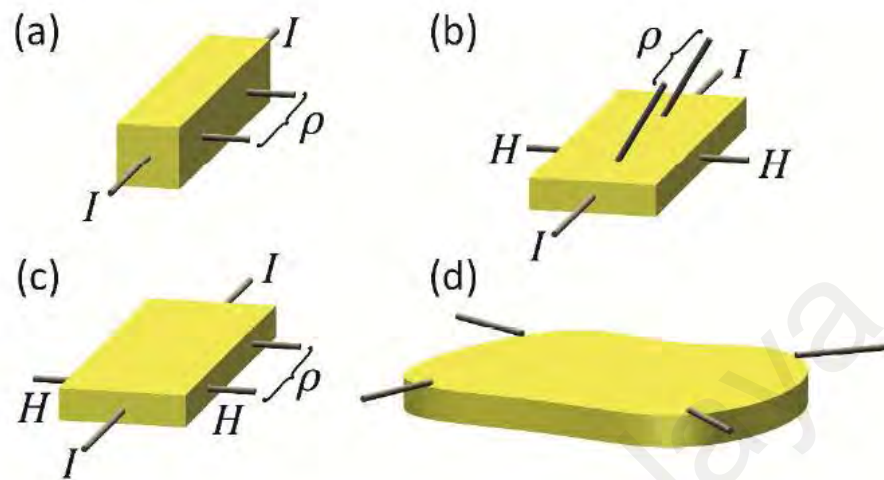


Figure 2.15: Different contact arrangements for resistivity and Hall effect measurements: (a) contact arrangement on bar shaped sample. (b) 6-point and (c) 5-point contacts (d) resistivity measurement on non-uniform sample (Borup et al., 2015).

By using four-point probe method, the parasitic voltage is eliminated due to the voltage drop within the circuit of voltage path is considered very low. This is caused by the high input impedance which is around 10^{12} ohms or higher (higher especially when measuring highly resistive samples). The probes for four-point probe measurement can be arranged in collinear position, or, equal distance to the periphery of the samples as normally practiced in Van der Pauw measurement, or, any other configurations are also possible but which then will be subjected to complexity in determining the correction factors. These various configurations are made possible due to the calculated correction factors for each different configuration and also the type of sample when the resistivity is obtained. The correction factors have been calculated by the method of images, complex variable theory, the method of Corbino sources, Poisson's equation, Green's function and conformal mapping. For instance, the correction factor of the thin film resistivity

measurement with equal spacing, collinear probes arrangement of 4.532 has been determined.

In addition to geometry arrangement, the thermal stability of the sample must be taken into consideration as well. In a temperature dependent resistivity measurement, a precaution must be taken in order to ensure the temperature across the sample is distributed uniformly. The temperature gradient will introduce unnecessary thermoelectric voltages. The source of temperature fluctuation during measurement may be caused by the ambient effect if the measurement is not performed in a controlled environment. However, the ambient effect is not the only reason for temperature gradient. Temperature gradient also can be induced by current heating on the tips of the probes especially when measuring low resistivity samples because the current supplied is too high.

2.9.2 Seebeck Coefficient

Seebeck coefficient is one of the temperature dependent property of interest in thermoelectric characterisations, next to electrical and thermal conductivities. Seebeck coefficient is measured by employing either integral method or differential method. Integral method is suitable for sample with longer heating axial direction, enable the temperature on one side to be fixed and maintained long enough for Seebeck coefficient measurement, whilst the temperature on the other end is increased invariably to create higher temperature difference. Normally integral method is served as an approximation as a more sophisticated method is achieved by using a differential method. In differential method, the mean temperature is kept constant although the temperature on either end of the sample is varied to some extent. Differential method can be applied under steady state, quasi-steady state or transient conditions depending on the setup and the ability of the

instrument used. Generally, the measurement under steady state condition is more accurate but in comparison it will consume longer time than transient measurement.

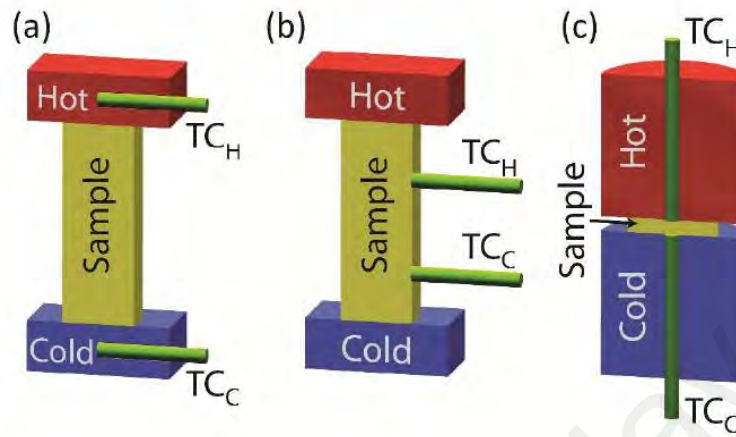


Figure 2.16: Measurement of Seebeck coefficient on samples with different geometries. (a) 2-point setup. (b) off-axis 4-point. (c) uniaxial 4-point (Borup et al., 2015).

Measurement of Seebeck coefficient on bulk materials is usually performed with commercially available equipment such as ULVAC ZEM-3, MMR SB-100, and Linseis LSR-3. Self-fabricated setup is preferred when measuring thin film, structurally challenging samples and also device with complete set of pair of junctions. The simplest self-fabricated setup will mostly consist of a couple of heater-cooler element, or simply a peltier device to control the temperature on one side of the sample. The temperature is measured by using a pair of thermocouples on both ends of the sample as illustrated in Figure 2.16. The temperature on the other side is raised and simultaneously the Seebeck voltage is measured by using voltmeter. The Seebeck voltage is plotted against the temperature difference. The Seebeck coefficient is computed as the slope in the plot or the ratio of the Seebeck voltage to the temperature difference.

2.9.3 Thermal Conductivity

Thermal conductivity ($\kappa = \kappa_e + \kappa_L$) of materials are contributed by heat from mobilised charges (κ_e) and the phonons carried through lattice (κ_L). The accepted error

for most thermal conductivity measurement is within 5%. Thermal conductivity measurements are performed over a broad temperature range, due to different requirements in specific application. Figure 2.17 shows different methods which have been used in thermal conductivity measurement. Similar to the measurement of the electrical conductivity and Seebeck coefficient, in the thermal conductivity measurement setup, the probe connecting the thermocouples to the surface at which the measurement is taken place must be fully insulated from surrounding to reduce errors which are influenced by environment.

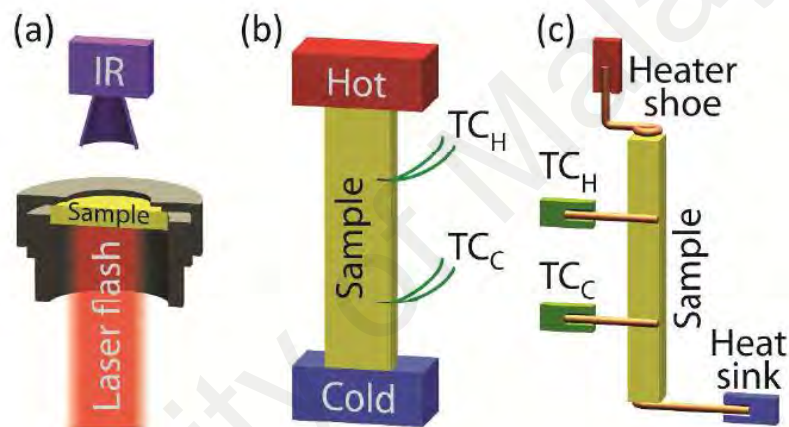


Figure 2.17: Measurement methods of thermal conductivity: (a) Thermal diffusivity measurement with the laser flashes method using IR camera to monitor the rise of temperature on the top side of the sample. (b) Steady state method (c) PPMS TTO: heat pulse transient method (Borup et al., 2015).

2.9.4 Raman Spectroscopy

It is well established that Raman spectroscopy is a very useful technique in identifying the characteristics of the materials based on the interaction between the incident radiation and the studied materials as illustrated in Figure 2.18 (Bhattacharjee, Alapati, & Verma, 2001; Haverkate et al., 2014; Schrader, 2008). Studies from literatures have compared Raman bands with similar type and functional group of molecules and have shown that each bond in the molecules interact uniquely with Raman incident radiation. Each of the bond in the molecule is vibrating at specific frequency when interacting with the light

source and this unique characteristic leads to the bond's and molecule's own set of band they corresponded in the spectrum (Bhattacharjee et al., 2001; Haverkate et al., 2014).

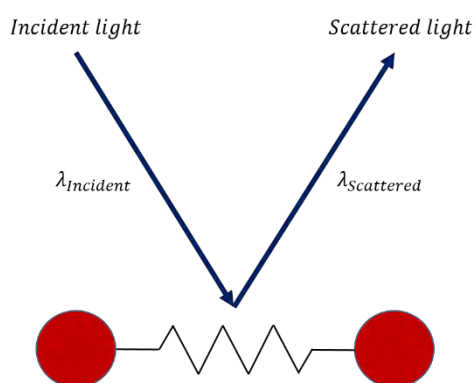


Figure 2.18: Scattering mechanism in Raman spectroscopy measurement.

Thus, the observed bands can be thought as a molecular fingerprint for various molecular structures of materials. Raman spectrum is the product of interaction between incident visible or near infra-red light source which possess certain energy, frequency and wavelength with the vibrating molecules. When incident radiation collides with the molecules in the sample, there is an instantaneous interaction involving energy transfer as the molecules reoriented from a relaxed state into polarized state (Bhattacharjee et al., 2001). Most radiation will be scattered by the molecules, but a fraction will be absorbed and excite the ground level electron from the molecules jumping to higher energy level (virtual vibrational energy states). The changes detected in energy level between the incident and scattered photon is then translated into a Raman spectrum.

Recent breakthrough in materials sciences has demonstrated the use of Raman spectroscopy in proving the theory on phase transition in Ising-type magnetic spin ordering in single and multilayers 2D-FePS₃. From the observation, it was concluded that the interaction between layers of 2D materials has little effect on the magnetic ordering. In addition, experimental study was successful in proving the transition from ordered magnetic spin to disordered paramagnetic spin during phase transition (Lee et al., 2016).

The Raman technique is also very useful in studying mechanical strength of -micro and -nano size materials and thermal characterisation such as thermal conductivity due to the dynamic information provided subtly by molecules during scattering process (Balandin et al., 2008; Huang, Ruan, Zou, Fu, & Yang, 2009; Lee, Yoon, Kim, Lee, & Cheong, 2011). Besides elemental and bonding information extracted from Raman spectra, the rigidity of the bond also could be determined by the broadening of the Raman curve due to the thermal expansion and softening of the strength modulus of the materials. This can be useful for studying crystallinity of carbon based compound such as diamond, graphene and graphite (Cançado et al., 2011; Ferrari & Robertson, 2000). A degenerate band of sp and sp^3 carbon is identified and compared with strongly active sp^2 carbon peak in order to quantitatively analyse the crystallinity of carbon based compound. This occurs when interatomic distance between atoms becomes larger as the temperature becomes higher and the molecules vibration getting stronger at increased frequency.

Analysis on Raman profile frequently involves the correlation between changes in the area, the full width at half maximum linewidth (FWHM) and the peak shift of the curve with physical structure and chemistry of the molecules (Haverkate et al., 2014). The area of the peak consists of information such as the concentration of Raman active species with coherent vibrational motions such as in C-C and C-H bonds. The area of the final peak profile will depend on the multitude of similar interaction of all the individual vibrational interactions. Thus, high activity of molecular interactions will give rise to a Raman peak with sharp intensity and large curve area. Consequently, the FWHM linewidth or broadening of the peak could provide an indicator such as the interaction of the bonds with the impurities presence in the materials or disordered structure. The FWHM linewidth can be estimated by taking the distance between two extreme values at half the peak of the measured dependent variable from the curve. Thus, any structural changes within the system can be interpreted by the changes in FWHM. Finally, the peak

shift will consist of information such as the difference in energy level of the materials before and after irradiation due to spontaneous polarizability which will cause the radiation to scatter either to higher or lower energy level. For example, upon spontaneous polarization of the radiated molecule with laser beam, the distortion of the electron clouds around the bond in the molecule will cause the bond to develop an induced dipole that will scatter the radiation differently. The strength of distorted electrons will cause the bond to either attract or repel each atom at the either end of the bond. The strength of this attractive or repulsive force will determine the shift of Raman peak to either higher or lower in wavenumber and frequency (Bhattacharjee et al., 2001).

2.10 Molecular Simulation of Organic Semiconductors

Simulation technique is a great tool in accomplishing what was considered difficult or not feasible during experimental research. Especially at the initial stage of research, predicting the behaviours of materials and for the purpose of designing a molecule for specific function. During simulation, various materials properties such as electronic, thermal and mechanical are identified. It is useful to be able to understand these behaviours before commencing experimental work. The results might deviate from the conducted experiment results, but further optimisations have been shown being able to bring the results closer to an actual one, or at the very least is able to provide an idea by exhibiting certain trends that could be interpreted as how the materials will perform. In some cases, theoretical prediction was used alongside conducted experiment as a reiteration method.

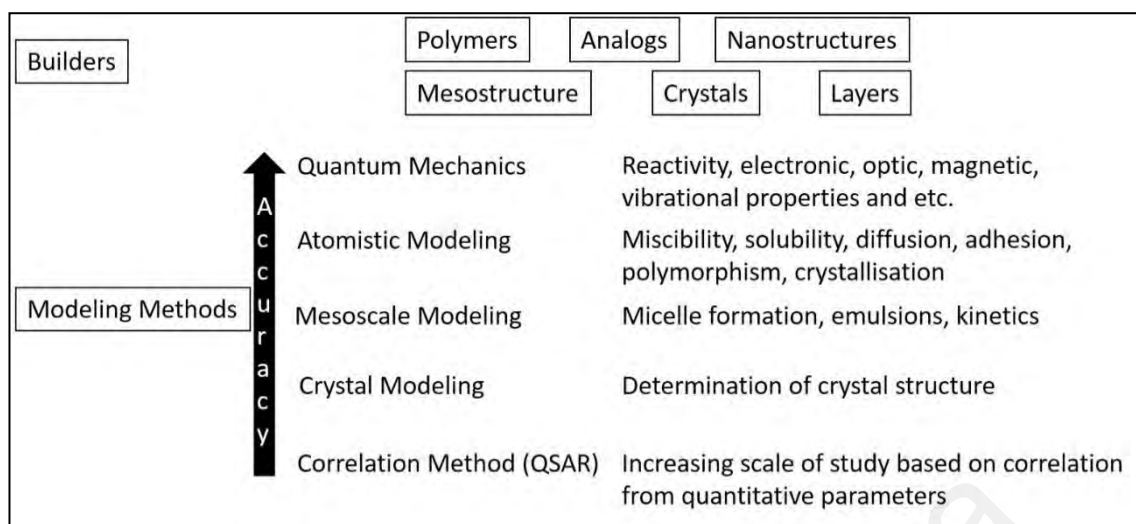


Figure 2.19: Molecular modelling using Materials Studio software.

In molecular modelling, the framework for simulation need to be setup. The types of modelling and the available analysis have to be predetermined as shown in Figure 2.19. First, the choice of the modelling method depends on (a) class of material, i.e. crystalline OSCs or amorphous polymers, (b) parameters to be studied, i.e. charge transport, vibrational properties and bond length. Then, an appropriate boundary conditions were applied i.e. choosing an amorphous space or crystalline periodicity block including the correct space group (especially for organic crystals). Secondly, selection of program, i.e. FORCITE from Molecular Dynamics method and DFT from Quantum modelling method.

The regular computational methods used in molecular studies are atomistic and quantum modelling. Both have their own advantages and disadvantages. The advantage of using atomistic calculation is that bigger systems can be modelled at satisfied approximation, such as dynamic processes i.e. phase transition. The limitations are 1) the type of forcefields available nowadays are still limited to certain type of material. 2) Investigation on chemical reaction is not possible, they involved bond breaking and forming. 3) Size of system would be approximately up to 10^4 atoms and a few nanoseconds as illustrated in Figure 2.20.

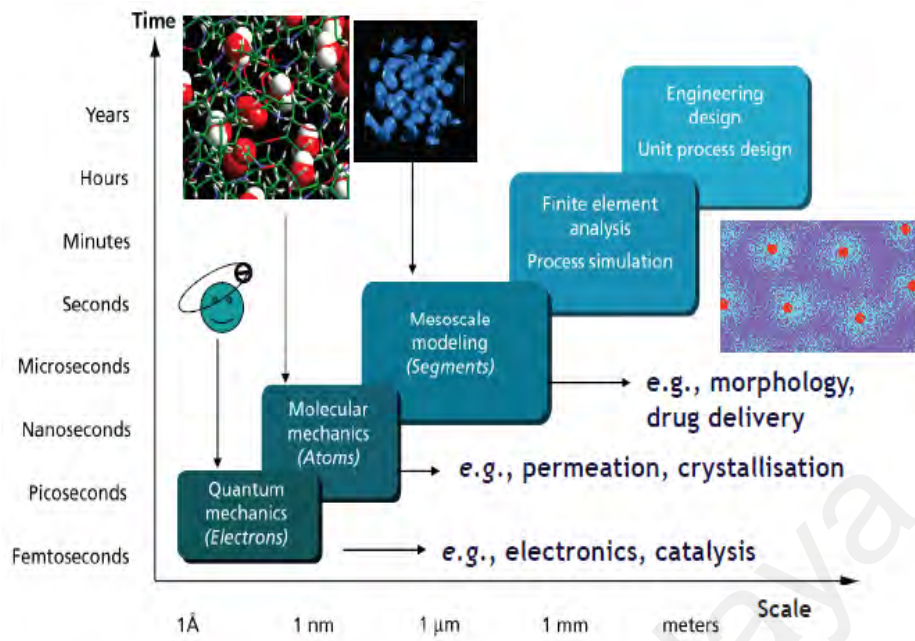


Figure 2.20: Time versus atomic scales of different computational methods.

2.11 Molecular Dynamics

Molecular Dynamics (MD) framework is based on the atomistic computation, motion for each atom is calculated by Newton's equation of motion

$$\mathbf{f}_i = m_i a_i = m_i \frac{\partial^2 \mathbf{r}_i}{\partial t^2} \quad (2.12)$$

The deterministic behaviour of classical equations of motion will allow the molecular study in the function of time, temperature and pressure to be investigated. In Molecular Mechanics, a molecule is described as a series of charged points (atoms) linked by springs (bonds) namely 'forcefield'.

$$\text{Potential Energy, } E_{total} = E_{valence} + E_{crossterm} + E_{non-bond} \quad (2.13)$$

$$\text{Valence Interactions, } E_{valence}$$

$$= E_{bond} + E_{angle} + E_{torsion} + E_{oop} + E_{UB} \quad (2.14)$$

$$\text{Non - bond Interactions, } E_{non-bond}$$

$$= E_{vdW} + E_{Coulomb} + E_{hbond} \quad (2.15)$$

Discover, GULP and Forcite are amongst the modules that are available in the commercial software which are based on atomistic computation. For instance, FORCITE MD calculation is performed in order to equilibrate the temperature and the molecule geometry at specific energy level for each temperature point. Forcite is an advanced classical molecular mechanics tool that allows fast energy calculations and reliable geometry optimization of molecules and periodic systems. Forcite calculates single point energies and performs geometry optimization (i.e. energy minimization) of molecules and periodic systems. COMPASS II (an extended and an advance version of COMPASS) is the most often forcefield type used in MM due to various extension of materials it has covered especially polymers and organic molecules (Sun, H., et al. (2016). COMPASS is able to predict various solid-state properties: unit cell structures, lattice energies, elastic constants, and vibrational frequencies. The combination of parameters for organics and inorganics makes possible the study of interfacial and mixed systems.

The two summation methods are (1) Electrostatic: Atom based (amorphous), Ewald (periodic system) and (2) Van der Waals (vdW): Atom based for both amorphous and periodic system have been used in parametrization of the materials. The parameterization which govern the non-bond interactions within the simulated system. The Ewald electrostatic option is widely used for periodic system, in the amorphous case, atomistic based models were used for both electrostatic and vdW. The properties calculated includes molecular structures, vibrational frequencies, conformation energies, dipole moments, liquid structures, crystal structures, equations of state, and cohesive energy densities.

2.12 Quantum Modelling

Ab-initio, semi-empirical Hartree-Fock and Density Functional Theory (DFT) calculations are performed in order to compute the geometries, electronic structure and

energies of molecules. Their frameworks are based on Quantum Mechanics modelling method. QM modelling method is considered as the closest approximation to the chemistries of the materials at molecular level. The behavior of the electrons is predicted by the equations derived from Schrodinger equation. Hohenberg, Kohn and Sham have applied the original equation and developed a numerical function and plane wave function in order to solve different problems in QM modelling. DMol3 numerical function is derived by Hohenberg-Kohn in equation 2.17. Meanwhile, Kohn-Sham developed plane wave function in equation 2.18 is used in CASTEP program.

$$\textit{Schrodinger equation}, \mathbf{H}\Psi = \mathbf{E}\Psi \quad (2.16)$$

$$\textit{Hohenberg - Kohn}, E_{total} = T[\rho] + U[\rho] + E_{xc}[\rho] \quad (2.17)$$

$$\textit{Kohn - Sham}, \left\{ \frac{\hbar}{2m} \nabla^2 + V(\{\mathbf{r}_i\}) \right\} \Psi(\{\mathbf{r}_i\}) = \mathbf{E}\Psi(\{\mathbf{r}_i\}) \quad (2.18)$$

QM calculation is more expensive compared to MD calculation. Quantum mechanics can be used to calculate reactivity, electronic, optic, magnetic and vibrational properties of molecular systems of the size hundred atoms. During computation, there are few considerations that have to be taken into calculation as well. Firstly, the exchange correlation energy, E_{xc} , i.e. Perdew-Burke-Ernzerhof (PBE) and generalized gradient approximation (GGA) non-local functionals have been used most often. Basis set is introduced, such as double numeric plus (DNP) polarization basis set 4 or 4.4. The DNP function describes the numerical orbitals for the basis functions of the system which is also corresponding to an atomic orbital. Greater variational freedom is obtained by providing larger basis set. DNP also includes polarization on all hydrogen atoms where the hydrogen bonding consideration is important in the calculation. It has the highest accuracy but at a high cost. In addition, the SCF calculation consists of basis set as one of its function. SCF tolerance under electronic tab specify the threshold for SCF density convergence. The density convergence criteria have to meet the specified SCF parameter

during the iteration for converging the calculation. The accuracy is increasing with smaller SCF parameter at a high cost, compared to larger SCF parameter which will shorten the calculation time sacrificing the accuracy. To specify the value used in mixing the charge density between the current and previous iteration in the SCF opt procedure. For example, a value of 0.2 would construct a charge density using 20% of the current density and 80% from various previous iterations. Otherwise the charge calculation will be estimated incorrectly during SCF iteration.

2.12.1 Molecular Modelling of DLCs and Small Organic Molecules

Molecular simulations have been conducted in order to investigate various aspects of DLC materials in terms of structural, dynamics, charge transfer, and electronic orbitals properties. Simulation of electronic properties in organic semiconductors is very helpful in assisting one to understand, for instance, the effect of charge carriers on band gap and the materials density of states. Therefore, simulation also enable one to optimize the device which are operated with organic semiconducting materials as its active materials. In theory, the behaviour of organic semiconducting materials predicted by simulation are correlated with charge transport of the materials as suggested earlier. Although physical attributes also quite important especially in modeling of liquid crystal materials. In liquid crystal materials simulation, it is very important to specify the correct structural input during simulation, this will give a very structural order or alignment dependence results.

MD studies have been conducted on HAT5 molecules by Cinacchi et al. the purpose of the studies include (i) molecular conformation, (ii) structural order and (iii) translational dynamics (Cinacchi, Colle, & Tani, 2004). Modeling program used in this study was AMBER, with parametrization of OPLS forcefield. The results of this investigation were found in agreement with ^{13}C and ^2H NMR experiment which suggested the diablo-like configuration in the intermediate state, and alternating out with respect to

the alkyl chains of the triphenylene's core plane. The structural order of HAT5 molecules in a packing was also investigated by introducing 80 HAT5 molecules in liquid crystalline state. Again, the results showed coherent findings with experimental studies; co-facial distance of 3.55 Å and twist angle of 36 ° between adjacent molecules. Haverkate et al. have also demonstrated similar nature of studies, and found the correlations was satisfactorily in agreement with experimental works (Haverkate et al., 2011). The results were compared with powder diffraction, absorption, infrared and also Raman spectroscopy experiments.

Due to the transitioning behaviours of DLC materials, a dynamics method is a must in the studies of DLCs. The dynamics of the core and tails of DLC molecules have been investigated by Mulder et al. by integrating experimental QENS and MD simulations results (Mulder et al., 2003). From these studies, one may correlate the structural order of the DLC materials with their electronic behaviours. For example, the charge transfer process along stacking columns and formation of donor-acceptor in charge transfer complex systems can be microscopically investigated in order to enhance our understanding on the processes. Thus, modelling of charge transfer in DLCs can be improved when too often the underlying mechanisms when one will not able to observe from experimental studies.

Various commercial applications have found the use of simulation as very useful, for example in designing molecules that could work in compliance to the function. In medicine and pharmacy industry, modeling has helped the designer to design molecules which could make drug delivery process efficiently. Molecules used in biosensing devices were to have specific group that adhere to stimulus/i and respond accordingly. In electronic devices, a wide range of applications such as OLEDs, OTFTs, PVs and many others have been realized with the assistant of molecular modeling, in order to understand

at molecular level how each material for specific application can be better enhanced. From this simulation, one also could recognize the limit of charge transport, especially with combination of structural order that play very important role in maximizing the capacity of charge transport in organic semiconducting materials.

2.13 Summary

The literature surveys in the relevant topics are intended to bridging the research gap in thermoelectrics and organic semiconductors research. The studies on the device design of thermoelectric generators have highlighted the importance of selecting the materials with the best thermoelectric properties, especially the ones with low thermal conductivity. Furthermore, the studies have indicated how interdependence of the thermoelectric properties in metallic based thermoelectric materials has limited the efforts in order to improve them. However, significant progress was found in polymer and organic thermoelectric materials. The exploration on the emerging organic semiconductor has just begun, and is an encouraging field to work in. In addition, the appropriate techniques used to investigate organic materials should be carefully studied and considered. Recent findings have indicated the potential of organic materials to be the materials of the future due to numerous advantages associated with organic materials.

CHAPTER 3: METHODOLOGY

The methodology for the completion of the thesis has been proposed according to the Figure 3.1. Firstly, a design of solar thermoelectric generator (STEG) device that has the ability to retain heat was proposed. The STEG device was modelled and simulated by using two different modules from ANSYS software. This investigation leads further studies into the material's aspect of the conceptualised STEG device.

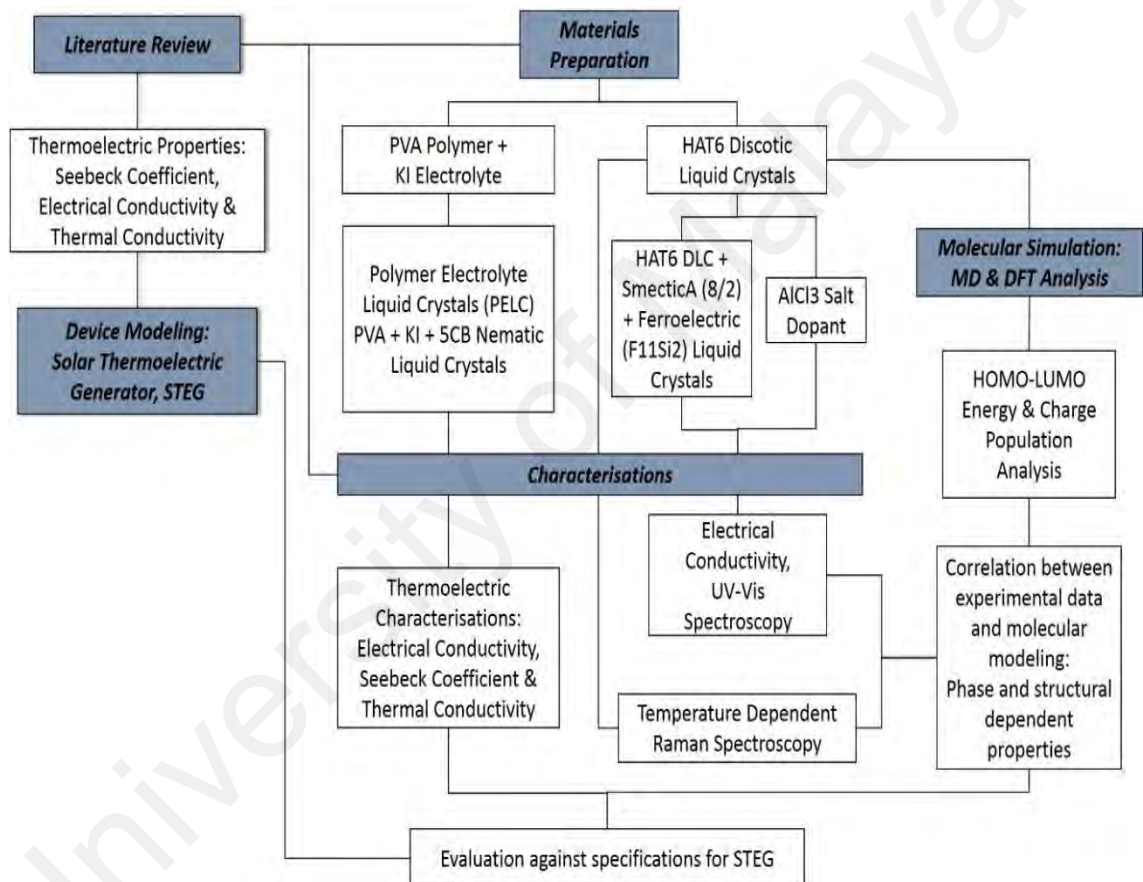


Figure 3.1: The flow chart of research methodology.

For that purpose, two different types of organic materials of liquid crystal classes are selected as candidate for active materials in STEG: (1) Nematic liquid crystals was used in the mixtures of PELC system. Thermoelectric characterisations were performed in order to measure the mixture electrical conductivity, Seebeck coefficient and thermal conductivity. (2) HAT6 discotic liquid crystals and their various mixtures with smectic

and ferroelectric liquid crystals, and AlCl_3 dopant were prepared. Electrical conductivity for all mixtures were measured. Temperature dependent Raman spectroscopy and molecular simulation were performed on HAT6 sample. The correlation between experimental data and molecular modeling was deduced in order to investigate the effect of phase changes and structural properties on electrical and electronic properties.

3.1 Modelling of Organic STEG Device

3.1.1 Simulation of Heat Entrapment of Solar Radiation for a Graded Multilayer Solar Funnel STEG

3.1.1.1 Geometry of STEG

Multilayers of thermoelectric material were constructed using the ANSYS finite element modeler. A structure containing planar multilayers of thermoelectric material was proposed, with the densest layer on the bottom of the structure, whilst the least dense structure lies uppermost on the structure as shown in Figure 3.2. A junction of thermoelectric device composed of multilayer stack is designed and simulated, in order to understand the heat distribution and voltage generation inside the structure. In each subsequent layer of polymer film, the used of materials with tuned composition of nanoparticles (CNT) have been used, in increasing order from the bottom to the top. CNTs are selected as dopants for these polymer layers due to their remarkable electrical, physical and mechanical properties. Consequently, this will result in a gradual variation of the thermoelectric properties (Seebeck coefficient, electrical conductivity and thermal conductivity) from layer to layer in the geometry of STEG architecture (Dubey & Leclerc, 2011; Meincke et al., 2004; Yu, Kim, Kim, & Grunlan, 2008). The objective of this simulation project will be to provide a set of specifications for the material parameters and device dimensions which will provide a good thermoelectric power output. The heat retaining properties of this structure and also optimised geometry (by adjusting the length of the leg whilst maintaining the radiation area) will also be discussed.

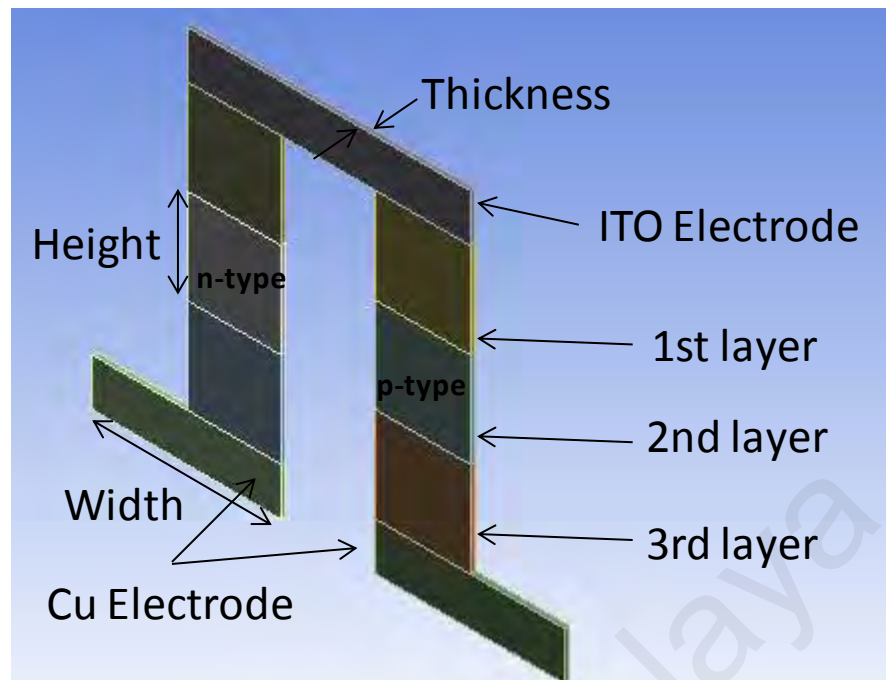


Figure 3.2: Schematic of planar multilayer thin film.

3.1.1.2 Material Properties

This simulation work is divided into two parts: the first being the solar heat absorption by the polymer-CNT layers. The parameters that are being investigated are listed in Table 3.1; and the second being the thermoelectric voltage generation from a single thermoelectric junction containing a single p-n junction of the graded multilayers of materials investigated in this work. The properties of the materials are listed in Table 3.2.

For the first part simulation, an idealized polymer-based thermoelectric material was chosen for this work because of the advantages of the polymer being flexible and easy to process. For good STEG performance, high transmissivity of the polymer layer and high absorptivity of electrodes are essential. As a realistic starting point, combinations of typical thermoelectric constants were selected. The Seebeck coefficient and electrical conductivity was referenced from a reasonably performing organic thermoelectric material, a poly (2,7-carbazole) derivative containing a benzothiadiazole, and containing CNT of 5%, 10% and 20% concentrations (Dubey & Leclerc, 2011). The low percentage

of CNT dopant was selected to ensure that the material remained relatively optically transparent.

3.1.1.3 Governing Equations for Solar Absorbance

The ANSYS FLUENT module is used to simulate a temperature distribution across the material under exposure to the sun. FLUENT simulates heat and optical transmission, absorption and reflection of solar energy in the graded multilayer. The relationship between solar absorption and TE generated can be generally described as follows

$$\rho C_p \frac{\partial T}{\partial t} = \frac{\partial}{\partial x} \left(k \frac{\partial T}{\partial x} \right) + E(x, t) \quad (3.1)$$

On the left hand side, the equation describes the rate of change of the energy content of the element of solar absorber and thermoelectric junction, equation on the right hand side describes the rate of heat conduction, with surface convection and radiation on the boundaries of the calculated element, and also the heat generation that is absorbed by the element. $E(x, t)$ represents the rate of solar energy absorption by the layer per unit volume as follows

$$E(x, t) = -\frac{\partial I_x}{\partial x} \quad (3.2)$$

The transient heat distribution across simulated thin film is solved by FLUENT from the equation above. The increase of energy when subjected to energy input such as solar radiation, $\frac{\partial I_x}{\partial x}$, can also be interpreted as below in equation 3.3 when calculating the efficiency of the STEG device

Solar Heat Input

$$\begin{aligned} &= \text{Harvested Thermoelectric Energy} \\ &+ \text{Radiative Loss} + \text{Convective Loss} \end{aligned} \quad (3.3)$$

3.1.1.4 Boundary Conditions

The radiation boundary condition was set up as an initial response to the ambient solar flux available during daylight hours. For simplicity of the study, perfect insulation was assumed on the sides and the bottom part during operation. This condition is ideal to avoid heat loss from the system and maintaining heat storage on the lower part of the thin film. The convection boundary condition was assigned on the top surface of the multilayer thin film. The boundary conditions of the simulated thermoelectric leg are illustrated in Figure 3.3.

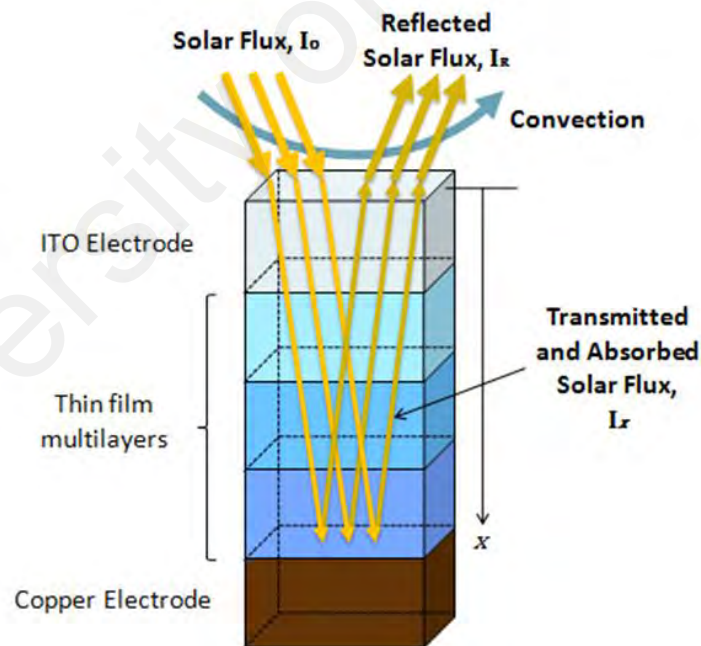


Figure 3.3: Boundary conditions of single thermoelectric leg.

The solar calculator and Discrete Ordinate (DO) irradiation were used simultaneously to simulate solar load which was applied to the system. Solar irradiation flux density (and ambient temperature of 27°C) were applied to the mode as initial conditions. The

dimension of the geometries of the simulated model in Figure 3.3 are tabulated in Table 3.3.

Table 3.1: Investigated parameters in FLUENT modelling

Convection Losses (W/m ² K)	0
	25
	35
Diffused Radiation (W/m ²)	0
	100
	200
Radiation Losses	Emissivity= 0.1
	Emissivity= 0.1, Absorptivity= 0.1, Transmissivity= 0.8
	Emissivity= 0.1, Absorptivity= 0.2, Transmissivity= 0.7
	Emissivity = 0.2
	Emissivity = 0.3
Length of the thermoelectric leg (μm)	3000
	1500
Thermal conductivity (W/mK)	Case I (low κ)
	Case II (high κ)

Table 3.2: List of parameters for a single thermoelectric leg containing three layers of conducting polymers in ANSYS device modeling

	Seebeck Coefficient, $\mu\text{V/K}$	Resistivity, $\Omega\cdot\text{m}$	Thermal Conductivity, $\text{W/m}\cdot\text{K}$	
			Case I	Case II
Upper Electrode		Indium Tin Oxide		
1st Layer	± 40	2.45E-05	0.10	0.21
2nd Layer	± 42	2.38E-05	0.12	0.22
3rd Layer	± 43	2.27E-05	0.14	0.23
Lower Electrode		Copper		
ΔT min between upper electrode and lower electrode, $^{\circ}\text{C}$			7.3	4.66
ΔT max between upper electrode and lower electrode, $^{\circ}\text{C}$			12.4	7.9

Table 3.3: Dimensions of simulated multilayer structure of thermoelectric device

Components	Height (μm)	Thickness (μm)	Width (μm)
ITO Electrodes	500	50	3000
1st Layer	1000	50	1000
2nd Layer	1000	50	1000
3rd Layer	1000	50	1000
Cu Electrode	500	50	2000

3.2 Preparation of samples

3.2.1 Preparation of Polymer-Electrolyte Liquid Crystal (PELC) Samples

PELC mixtures were prepared by using PVA (Sigma Aldrich, $M_w=89,000-98,000$), potassium iodide (KI; Merck), 5CB (Sigma Aldrich), and dimethyl sulfoxide (DMSO; Merck). The 5CB was drop-wise added to the DMSO solvent and stirred at room

temperature for one hour. Next, the KI, which provided the electrical conductance to the PVA matrix, was added and stirred for a further hour until it was fully dissolved. Then, the PVA was added to the resultant homogenous mixture, and stirred at 100 °C until the mixture turned transparent, i.e., the PELC viscous solution was prepared. Finally, the viscous solution was cast into a petri dish to form a thin film, and was dried at room temperature for a few days until the DMSO solvent was fully volatilized. The film thickness was in the range of 131-327 μm. The obtained thin film was then cut into 1cm×1cm square film for characterization. The ratio of components in the PELC mixtures were PVA:KI:5CB=100:60: x ($x=0, 5, 10, 15, 20, 25$). In this paper, the correlation between subphases of 5CB in the PELC mixtures and thermoelectric properties is explored.

In addition, mixtures of polymer electrolyte consisting of PVA and KI with Zinc Oxide (ZnO) were also prepared. ZnO powder was purchased from Sigma Aldrich. ZnO powder was added into DMSO solution. The mixture was stirred and heated at 100 °C for. Next, KI was added into the mixture of ZnO and DMSO solution. The mixture was further stirred at 100°C whilst PVA was added simultaneously. The ratio of components in the mixtures were ZnO:PVA:KI=1:100- x : x ($x=20, 30, 40, 50$).

3.2.2 Preparation of DLCs samples

3.2.2.1 DLC materials and mixtures

2,3,6,7,10,11-hexakis(*n*-alkoxy)triphenylene (HAT6 and HAT10) in the powder form were purchased from Synthon chemicals. Aluminium trichloride (AlCl₃) salt was purchased from Sigma Aldrich. 8/2 Smectic A and F11Si2 ferroelectric liquid crystals used in the preparation of ternary mixtures were synthesised by a project collaborator in CMMPE, University of Cambridge, United Kingdom. All the materials were used without

any chemical modification. The liquid crystal properties were confirmed by using polarising optical microscope and differential scanning calorimeter.

3.2.2.2 Substrate-DLCs-Air interfaced sample

HAT10 powder was mixed with ethanol solvent and the solution was stirred at 120°C. Indium tin oxide (ITO) coated glass substrates were cleaned by a sequence of Isopropyl alcohol (IPA) rub, IPA wash, Acetone dip, sonication with IPA solution followed by distilled water sonication, and air gun dried. Solution processable materials can be fabricated by using spin coating process. Spin coating is prevalently used in semiconductor fabrication technique. Spin coated materials are further decorated with electrodes and many electrical connections for device function using additional sputtering or lithography processes or metallic paste such as silver to make probe contact between narrow probe pins and thin coated film. In this experiment, gold paste was used in Hall mobility experiment, whilst silver paste was used in laboratory fabricated setup tests.

Spin coating comprises two major processes which take place simultaneously, firstly, radial liquid flow, which is a consequence of the centrifugal force and secondly, evaporation of the solvent, as shown in Figure 3.4. Both these two processes result in a decrease of the thickness of liquid film. Assuming the initial liquid film has uniform thickness over the substrate, and the liquid behaves Newtonian, upon rotation will result in increased concentration of solute, and upon evaporation the solvent will evaporate and leave the solute on the substrate. In this experiment, the solution on ITO substrate was spun for 30 seconds at 1000 rpm.

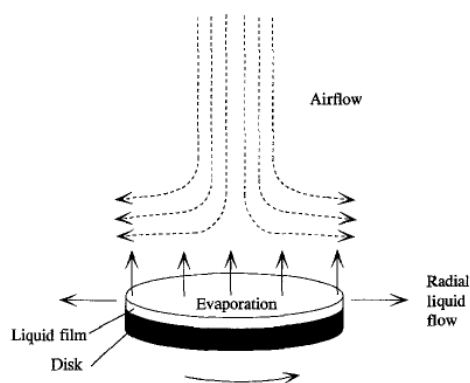


Figure 3.4: Mechanism of spin coating process. The uniformity of coated sample is governed by radial liquid flow and evaporation of solvent.

3.2.2.3 Ternary mixtures of liquid crystals

Ternary mixtures consisted of discotic (HAT6), smectic (8/2) and ferroelectric (F11Si2) liquid crystals were prepared. Firstly, 15 wt% of F11Si2 was mixed with 85 wt% of 8/2 smectic liquid crystals and the mixture was stirred thoroughly at 100 °C during preparation. Then, the HAT6 was added to the mixture in the following ratio (X:1-X, X= 20, 40, 60, 80 and 100), with X being the HAT6 component, whilst 1-X constituents were the F11Si2 and 8/2 liquid crystal mixture. The samples were cooled slowly to room temperature.

3.2.2.4 AlCl₃ Doped HAT6

HAT6 DLCs has been doped with different mole percentages of AlCl₃ salt. AlCl₃ was added to HAT6 powder in the following percentages: 0, 2.5, 5.0, 7.5, 12.5 and 15.0 mole percents. The mixtures were heated in the furnace for an hour at constant temperature of 110 °C, and cooled down to room temperature at the rate of 5 °C per minute. The prepared cell was then placed on a heater at the isotropic temperature of the sample, the AlCl₃ doped HAT6 was placed on the opening of the cell. The melted mixture was then allowed to fill in the cell and occupy the space between the sandwiched substrates. To ensure proper crystallisation of the sample, the cell was then cooled down at the rate of 5 °C per minute.

3.2.2.5 DLCs Cells

ITO coated glass substrates were cleaned by cleaning sequence described earlier. A pair of ITO cells were used to create a single liquid crystal cell. The fabricated cells were glued by using epoxy glue which has been mixed with microbead spacer of approximately $10\ \mu\text{m}$ in diameter as illustrated in Figure 3.5. The cells were then used to carry out mesophase investigation under polarising optical microscope and electrical conductivity measurements. The method of substrates cleaning as described earlier will modify the surface property of the substrates to become more hydrophilic. This allows liquid crystals to flow into the cell due to hydrophilic capillary mechanism. As previously noted these molecules self-assembled into columnar stacks in a two-dimensional lattice. Charge transport is enabled along the columnar axis through significant overlap of π^* - π^* orbitals of adjacent aromatic rings of the discotic molecules creating a conducting pathway. The columnar stack of discotic liquid crystal molecules is established by raising the temperature of the materials into its transition phase. The properties of discotic liquid crystals are tested on the fabricated discotic liquid crystals cell. Discotic liquid crystals cell is fabricated by inserting the materials into the heated cell (beyond isotropic phase). Through capillary mechanism the discotic molecules will flow into the cell.

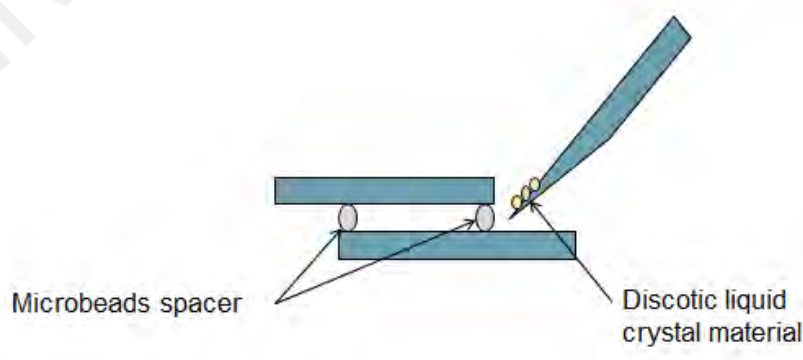


Figure 3.5: Preparation of DLC in ITO cell.

3.2.2.6 Preparation of Graphene Cells

Graphene was synthesised on thin copper foils by chemical vapour deposition method. Poly(methyl methacrylate) (PMMA) was coated on the top surface of graphene. The graphene and thin copper foils were separated by ferric chloride (FeCl_3) in etching process. Graphene on PMMA coating remained at the end of the process. The graphene film on PMMA was then transferred on the cleaned glass substrate. Glass substrate was cleaned using water, detergent and alcohol sequence. PMMA coating was removed by using UV light. Nickel was sputtered on the graphene in order to create the electrodes. The ready-made graphene substrates with nickel electrodes were then sandwiched together using epoxy glue and micro bead spacers.

3.3 Thermal Characterisation

The thermal characteristic of the 5CB-free and PELC mixtures was measured using differential scanning calorimetry (DSC; Labsys EVO, SETARAM). The mixture was placed in an aluminum crucible, and heat flow was induced between the mixture and reference. The mixture was heated from 20 to 50 °C at the rate of 1 °C /min under Ar gas at a flow rate of 20 cm³ min⁻¹.

Phase transition and enthalpy reaction of HAT6 and ternary mixtures was determined from DSC thermogram in heating and cooling cycle scan by using Mettler Toledo differential scanning calorimeter at the rate of 2 °C per minute.

3.4 Optical Characterisation

Olympus BX51 polarizing optical microscope was used to identify the mesophase type of the HAT6 compound. The microscope was installed with Linkam T95 hot stage with temperature controller to scan the sample in heating and cooling cycle at the rate of 5°C/minute.

3.5 Characterisations of Various Organic Semiconductor Systems

3.5.1 PELC System

3.5.1.1 Electrical Conductivity and Seebeck Coefficient Measurements

The electrical conductivity and the Seebeck coefficient were measured in vacuum in the temperature range of 27 – 45°C as shown in Figure 3.6 (RZ2001i, Ozawa Science). The pressure was 5×10^{-5} Torr. The mixture clamped on a ceramic block with two Ni electrodes was mounted horizontally between two Pt electrodes. Platinum wires were also fixed by the Ni electrodes. The electrical conductivity was measured by means of the two-probe method, where a DC current passed through the mixture using one side of the thermocouples attached to the Pt electrodes and the corresponding voltage between the contact points of Pt wires was measured. By varying the current from -1 to 1 μA , the voltage was repeatedly measured. Using a linear current-voltage curve, the resistance was determined.

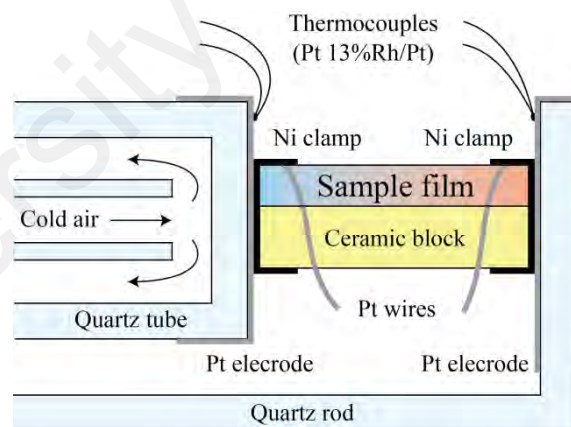


Figure 3.6: Setup of electrical conductivity and Seebeck coefficient measurements using Ozawa scientific equipment.

For the Seebeck coefficient measurement, a temperature gradient was generated by cooling the one end of the mixture with cold air inside a double walled quartz tube. The different temperature gradients were generated by controlling the flow rate of cold air. The temperature gradients and corresponding voltages were measured simultaneously. The Seebeck coefficient was evaluated from a linear temperature gradient-voltage curve.

The reliability of the electrical conductivity and Seebeck coefficient was ensured by the linearity over 90%.

3.5.1.2 Thermal Conductivity Measurement

The thermal conductivity of the 5CB-free and PELC mixtures was measured at room temperature (29 °C) using the fully automated laser flash method (TC-7000, ULVAC-RIKO). A laser pulse was used to heat the sample. Temperature profiles as a function of time after heated by the laser pulse were obtained by using an infrared camera behind the mixture and a Pt-13%Rh/Pt thermocouple of 0.05 mm diameter attached to the mixture. These measurements gave the thermal diffusivity, a , and specific heat, C_p . The thermal conductivity was then calculated by using the relation, $k=a \cdot C_p \cdot r$, where r is the density of the mixture.

3.5.2 DLCs system

3.5.2.1 Van der Pauw Electrical Conductivity Measurement

The temperature dependence of electrical conductivity was measured by a four-point Van der Pauw measurement technique for square-shaped thin film samples. Van der Pauw technique was used in electrical conductivity measurement of thin film and spin coated sample. Typical Van der Pauw measurement arrangement will consist of 4 micropositioner with very thin probes at each corner of the sample forming a square or rectangular shape as shown in Figure 3.7. The ratio of the distance of the probe at opposite end will be used to estimate the correction factor in optimising the measurement. When constant DC current was applied between the electrodes placed in both edges of a sample across the length, potential drop was detected between the other electrodes on opposite edge. Tungsten carbide probes were used as electrodes to supply the current measure the potential difference in electrical conductivity measurement. Conductive silver paste was

used to improve the ohmic contact and prevent Shottky barrier between probes and the samples.

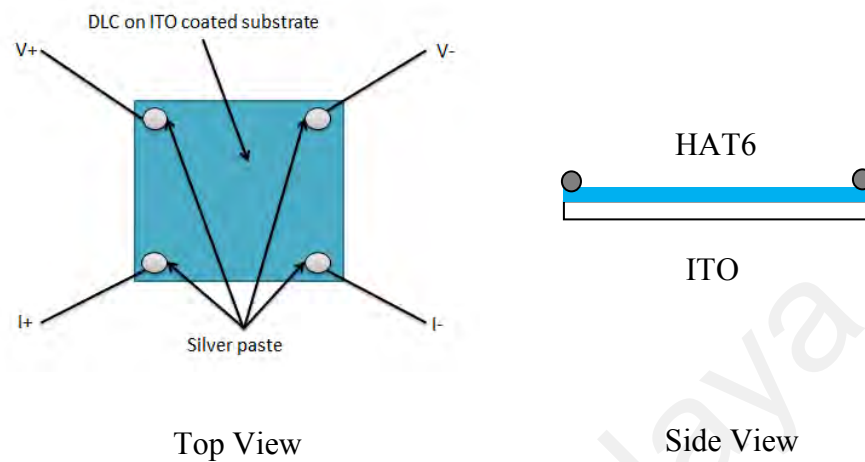


Figure 3.7: Schematic illustration of Van der Pauw measurement.

Electrical conductivity was determined from the measured potential drop and the applied current to obtain the resistance values. The resistance values and sample dimensions information were collected to calculate the electrical conductivity. The thickness was measured by KLA Tencor P-6 surface profiler.

3.5.2.2 Seebeck Coefficient Measurement

For seebeck voltage measurement, sample was heated on one side and naturally cooled on the opposite side by releasing heat to the copper block which acted as the heat sink. Referring to Figure 3.8, two probes were used and located at each side of sample (hot and cold side) to measure the seebeck voltage produced as a result of temperature gradient.

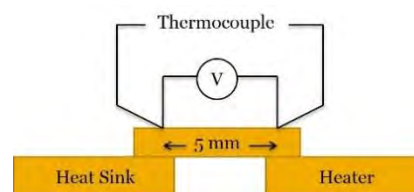


Figure 3.8: Schematic of laboratory fabricated setup for measurement of Seebeck coefficient

Keithley 2400 Sourcemeter was used to measure the Seebeck Voltage as shown in Figure 3.9. To ensure good ohmic contact between probes and sample, silver paste was used. The K-type thermocouples were used to measure the temperature for seebeck voltage measurement. Seebeck coefficient was obtained from the slope of the produced thermoelectric voltage as a function of the temperature difference along the length of the sample.

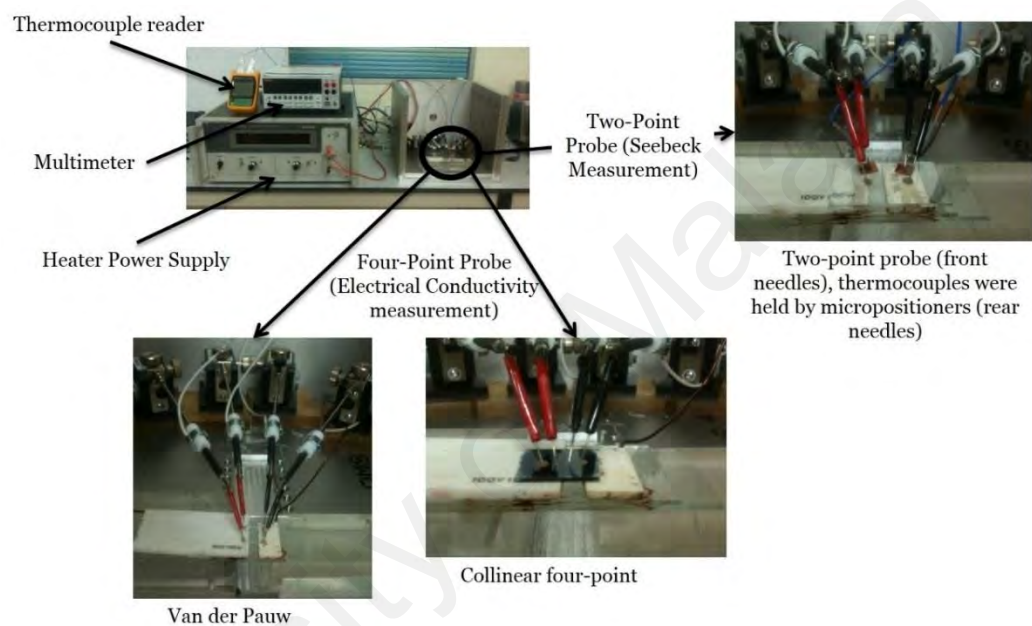


Figure 3.9: The setup for electrical conductivity and Seebeck coefficient measurements.

3.5.2.3 Hall Effect

Temperature dependent Hall Effect measurement was performed by using Ecopia HMS 5300 from room temperature up to 75 °C. The gold coated electrodes were used for Hall Effect measurement.

3.6 Temperature Dependence Raman Spectroscopy Measurement

Molecular vibration in HAT6 DLCs sample is investigated by using Raman spectroscopy. Raman spectra of HAT6 compound were collected with a Renishaw Raman InVia microscope operating in backscattering geometry with two different visible laser

lines (488 nm and 514 nm). The schematic of Raman spectroscopy setup is displayed in Figure 3.10. The light was focused using a 20x-magnification 0.75N/A lens, of varying intensity (500 μ W to 1 mW) laser power until fluorescence signal running the interference was sufficiently subtracted from the signal. The temperature of the sample was controlled by a Linkam hotstage, as shown by the schematic in Figure 3.10 and the Raman spectra were recorded in the cooling and heating cycles of liquid crystals. The range of wavenumbers plotted in the recorded spectra was in between 1300 to 1700 cm^{-1} . This range is the focus of the study due to the similarity of Raman profile with those hydrocarbons based materials with aromatic ring and ligand structures. In order to obtain a high signal-to-noise ratio, each Raman spectrum is an average over 40 spectra recorded at 15 s exposure time.

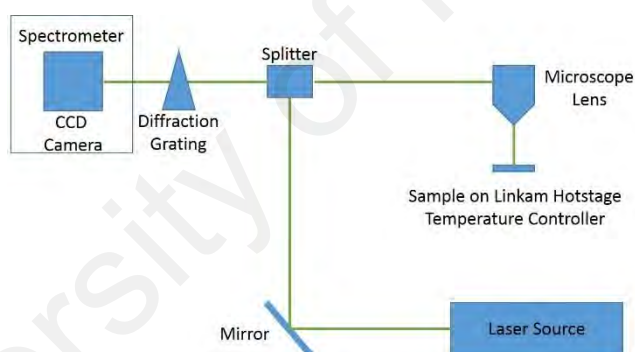


Figure 3.10: Schematic diagram for Raman spectroscopy measurement.

3.7 MD Simulations and DFT Calculations

Molecular dynamic (MD) and DFT calculations were carried out on HAT6 molecules using the Materials Studio simulation package. The initial geometry of the HAT6 molecule containing 144 atoms is represented by a planar central core, surrounded by ligands which are out of plane with respect to the central as shown in Figure 3.11. 3 cases were explored to analyse the molecule's electronic interactions: single molecule system, two molecule systems and a periodically stacked (1D) system. In all these cases, the

molecular symmetry of the point group planar D_{3h} structure was selected to provide a simplified representation and also to boost the speed of computing time.

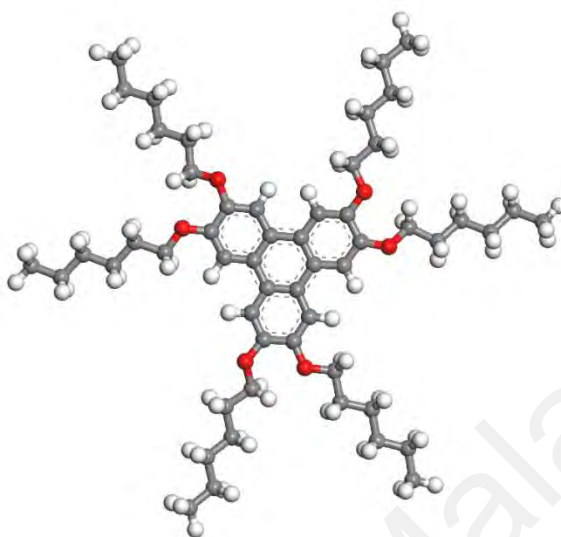


Figure 3.11: Drawing of molecular structure of HAT6 by using Materials Studio.

3.7.1 FORCITE MD Calculations

To initiate the simulation, the FORCITE MD module was used to stabilise and equilibrate the optimal molecular geometry at a given temperature. The reference force field used was COMPASSII which was based on the improved version of London dispersion energy approach by Lennard-Jones function. The convergence tolerance of the force, energy and displacement used were 2×10^{-5} kcal/mol, 0.001 kcal/mol/Å and 1×10^{-5} Å respectively. A standard atom based summation method was applied for single molecule calculation, whilst the Ewald method was applied for periodic crystal model calculation in non-bond energy calculation. The temperatures of interest used in this simulation were 27°C, 80°C and 130°C. This was carried out using NVT canonical (N= Number of particles, V= Volume, T= Temperature). The Berendsen thermostat was used for the temperature setting, and was applied for time step of 1 fs for a total simulation

time of 50 ps. This routine revises the kinetic energy with external thermal bath to keep the temperature of interest constant and minimizes error.

3.7.2 DMol3 DFT Calculations

Then the next step was to further optimize the geometry of the molecule using DMol3 module. The density functional spin polarized calculation was performed by adopting the Generalized Gradient Approximation (GGA) and Perdew-Burke-Ernzerhof (PBE) functional combination with basis set of DNP 4.4 set file. The DFT calculations also were assigned with a semi-core pseudo-potential for all the electrons. Raman spectra and temperature dependent HOMO-LUMO energies are predicted from this calculation.

University of Malaya

CHAPTER 4: DISCUSSION

4.1 Device Specifications of Solar Thermoelectric Generator

A junction of STEG device consisted of multilayers structure has been designed and modelled by using ANSYS software. The purpose of this simulation is to proof a concept of STEG device that can convert heat to electricity with small temperature difference. This focus is to fit the current trend of studies in polymer and organic thermoelectrics which can only operate at low temperature. Thermoelectric performance was evaluated by incorporating ANSYS Thermal-Electric module onto the designed structure, after their heat storing capabilities and temperature distribution along the STEG legs have been simulated by using FLUENT. For a single thermoelectric junction, the thermal transfer and continuity of electric charge equations are described by the coupled thermoelectric field equations 3.4 and 3.5 to solve for generated power output. For proof of concept, a three-layer graded multilayer structure forming an overall n-type thermoelectric leg was constructed as illustrated in the Methodology chapter.

4.1.1 Heat Entrapment Due to a Graded Multilayer Solar Funnel STEG

Figure 4.1 shows a plot of solar irradiance for Kuala Lumpur, Malaysia as a function of time in a 24-hour cycle. For an initial condition, the solar irradiance is taken to be the direct radiation from the sun. In addition, a constant value of diffuse radiation, defined as the sunlight that has been scattered by particles in the atmosphere, was added at a constant value throughout the 24-hour cycle – where 0 W/m², 100 W/m² and 200 W/m², resulting an addition of 0, 41% and 58% respectively of diffuse radiation to direct radiation as shown in Figure 4.2.

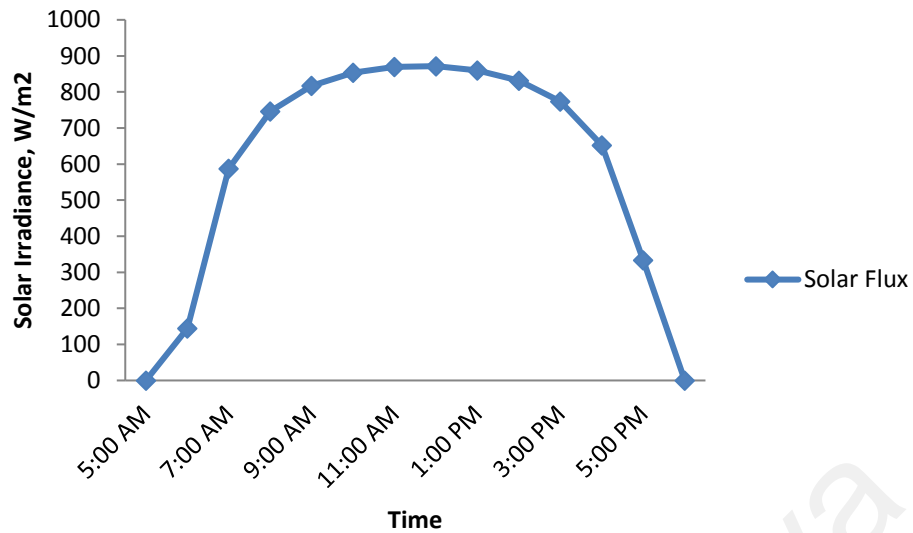


Figure 4.1: Solar irradiance for Malaysia geographical position.

Correspondingly, a plot of heat entrapment as a function of diffuse radiation within this 24-hour period is shown. Using the initial ambient temperature of 300 K, the temperature of the hot side was successfully elevated to approximately 313 K during the daylight hours, and dropped to approximately 307 K during the night hours, which is still consistently higher than the ambient. Thus, it is demonstrated that the graded multilayer STEG structure acts as both a solar funnel and heat bank, which is then able to provide a consistent temperature gradient for thermoelectric operation, even in the absence of solar radiation. The solar funnelling effect is seen to be an analogy to the concept of the macroscopic solar pond, where salts of different densities are stacked in a gradient of increasing density in order to channel heat from solar irradiation into the base of the solar pond. The heat entrapment is seen to increase directly as a function of diffuse radiation, but the profile of the heat entrapment does not seem to vary significantly as a function of diffuse radiation. Figure 4.2 plot of solar irradiation, diffuse radiation and heat entrapment as a function of time (hourly in a 24-hour cycle).

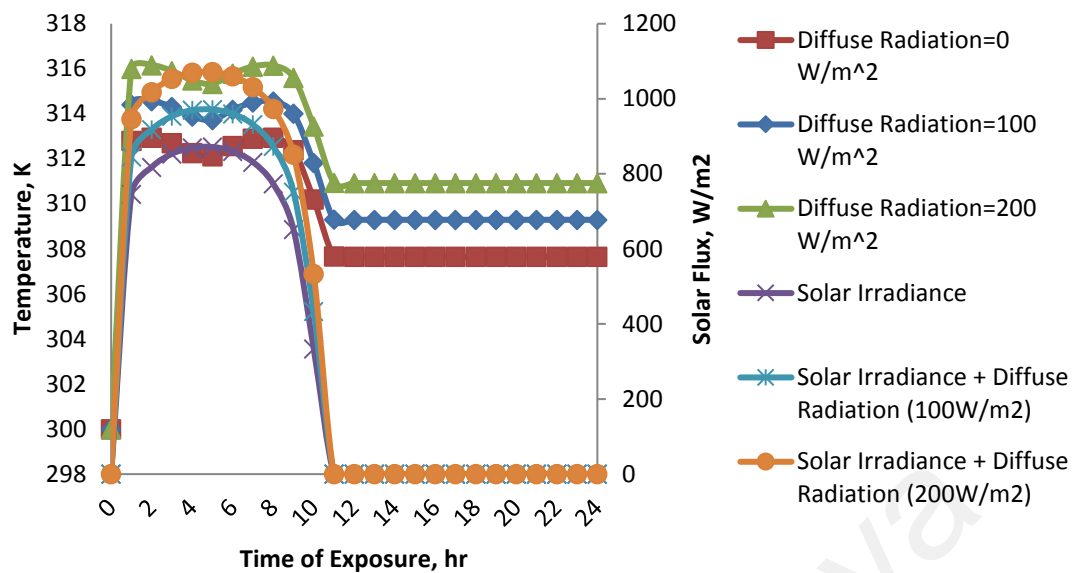


Figure 4.2: Effect of diffuse radiation on the temperature of thermoelectric absorber.

4.1.1.1 Convection Effect

Figure 4.3 shows a plot of heat entrapment for varying convection coefficients. Given the definition of convection coefficient as $25 \text{ W m}^{-2} \text{ K}^{-1}$ and $35 \text{ W m}^{-2} \text{ K}^{-1}$ was used in this simulation, which is typical of ambient condition at calm weather and windy respectively. It can be seen that the profile and magnitude of the heat entrapment shows almost negligible difference, and thus the effect of the convection coefficient is not considered as a significant contributing parameter to the heat entrapment behaviour of the graded multilayer solar funnel STEG.

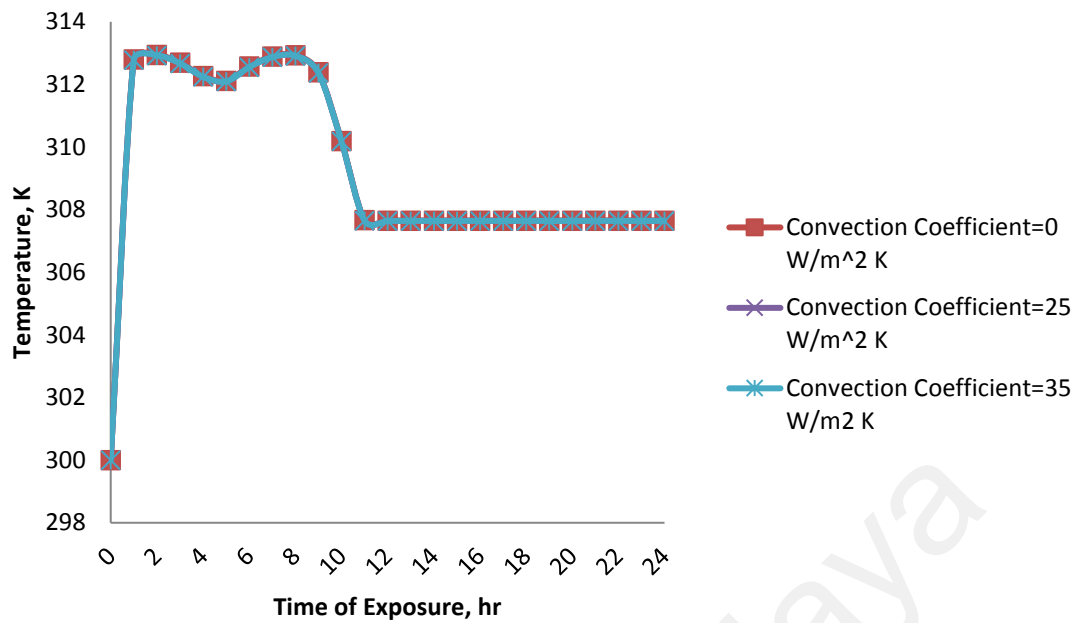


Figure 4.3: Plot of heat entrapment as a function of time in a 24-hour cycle, for varying convection coefficients.

4.1.1.2 Radiation Effect

Next, the function of the absorber layer of a fixed dimension (height= 1000 μm , width= 1000 μm , thickness= 50 μm) of the copper electrode was simulated. Given that an ideal absorber layer should have a low emissivity and high absorptivity, emissivity values in the range of 0.1-0.3 was simulated, where a small effect of the emissivity value was seen on the overall heat entrapment temperature in Figure 4.4. Conversely, in Figure 4.5, the absorptivity and transmissivity of the (polymer) graded multilayer structure was simulated, assuming a constant value of reflectivity=0.1 and a combination of absorptivity = 0.1 and transmissivity =0.8; and absorptivity =0.2 and transmissivity = 0.7. Interestingly, whilst using the original set of parameters there was a marked temperature drop in the absence of solar irradiation (in the evening hours), the use of a low absorptivity material results in a highly stabilized temperature entrapment, where hot junction was maintained very close to the maximum achievable temperature, in this case 313 K, even during the night. As such, the use of a polymer-nanoparticle hybrid with a low

absorptivity value may result in an effective thermal bank, where the temperature gradient is successfully maintained at a consistently higher temperature compared to the ambient.

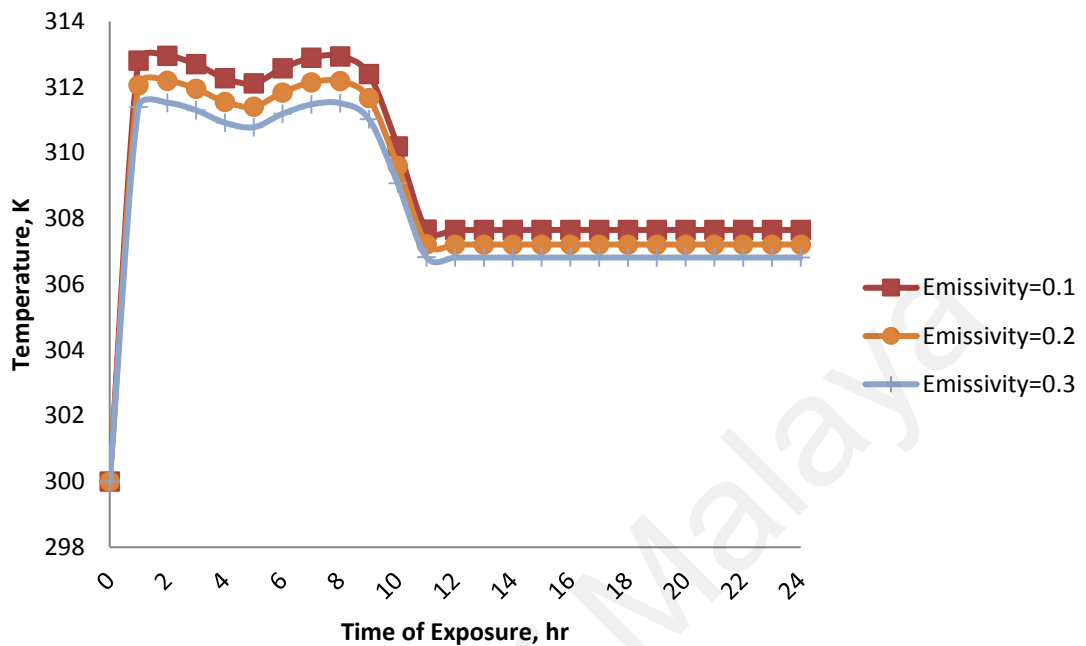


Figure 4.4: Effect of absorber emissivity on the temperature of thermoelectric absorber.

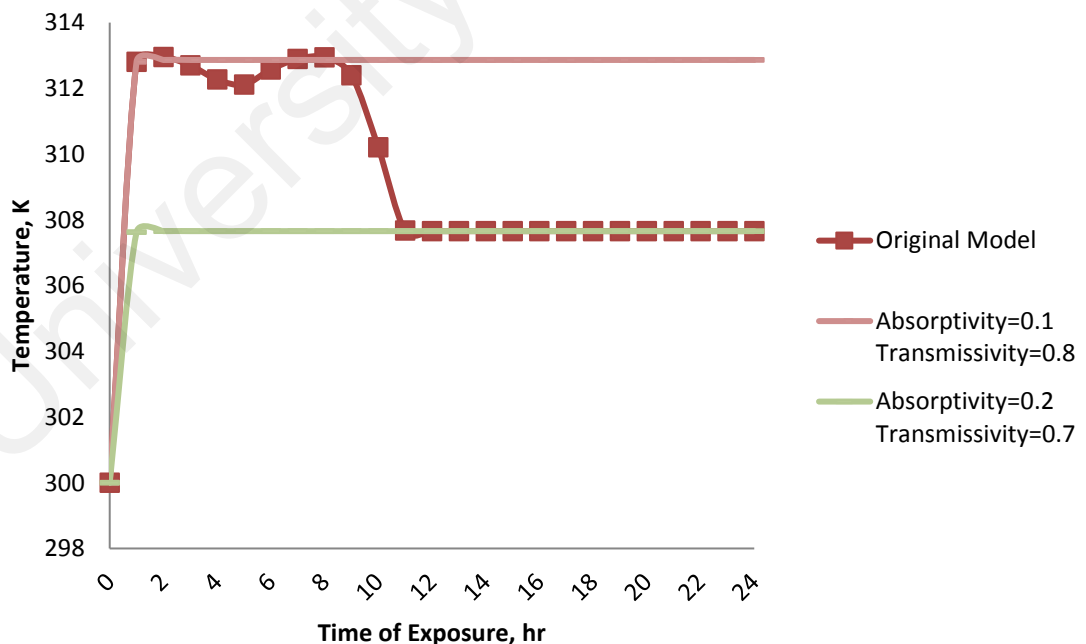


Figure 4.5: Effect of multilayer thin film radiation properties on the temperature of thermoelectric absorber.

4.1.1.3 Geometry Optimisation

Finally, a comparison of the solar entrapment behaviours under different conditions has been shown in Figure 4.7. In terms of geometry modification, it can be expected that the heat entrapment effect is directly dependent on the mass of the graded multilayer material, and thus a reduction in the height of the thermoelectric legs correspondingly results in a decrease in heat entrapment. Similarly, an increase in thermal conductivity (case 1 and case 2 from table Table 3.1) has resulted in a decrease in the maximum temperature by about 33.3%. Most significantly, heat retention performance of a conventional STEG structure, but containing the same graded polymer multilayer as the solar funnel device, but ‘inverted’ (Figure 4.6) compared to the original solar funnel design, was simulated. In the ‘inverted’ multilayer structure, where the hot terminal is uppermost in receiving solar radiation, it can be seen that the maximum temperature of the solar funnel is 300% higher compared to the ‘inverted’ multilayer, where the maximum temperature of a conventional STEG is only less than 3 K higher than the ambient temperature.

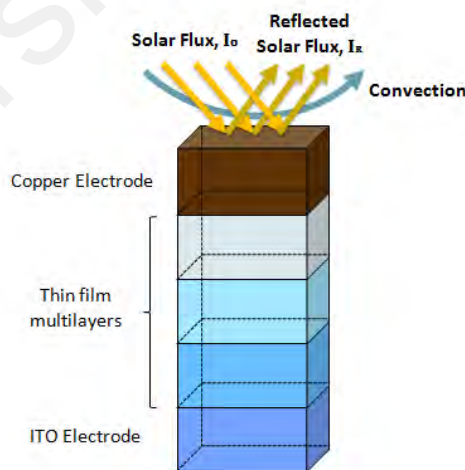


Figure 4.6: Inverted multilayer structure with copper electrode as the outer side part exposed to the sun.

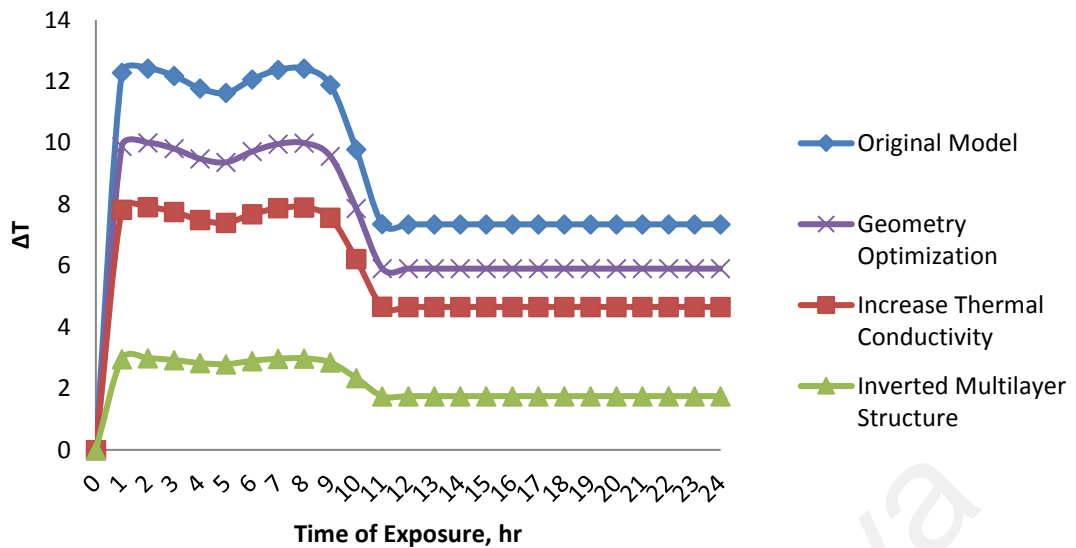


Figure 4.7: Comparison of the solar entrapment behavior, based on the original set of parameters, compared against modifications in geometry, thermal conductivity and inverted structure.

4.1.1.4 Thermal Capturing of Single n-Type Leg Thermoelectric Column

For a single n-type leg of the graded multilayer solar funnel STEG material, referring to Table 3.1, Cases 1 and 2 denote different sets of material parameters, the primary difference between them being Case 1 is for a set of low thermal conductivity polymers, whilst Case 2 is for a set of high thermal conductivity polymers. The polymer gradient established by heat entrapment through the heat funneling effect in Case 1 and 2 is defined as 30 °C and 35 °C, as the cold and hot temperature terminals in the thermoelectric column, respectively. The heat distribution through the column is compared for Case 1 in Figure 4.8 and Case 2 in Figure 4.9. Referring to the ‘red’ zone in each diagram, which has the hottest temperature in the structure, it can be seen that for Case 1, this temperature range is retained across only approximately one third of the thickness of the first layer of thermoelectric film. In contrast, for case 2, the same temperature is retained across almost all of the thickness of the first layer of thermoelectric film, thus demonstrating the correlation between the heat capturing capabilities and the thermal conductivity.

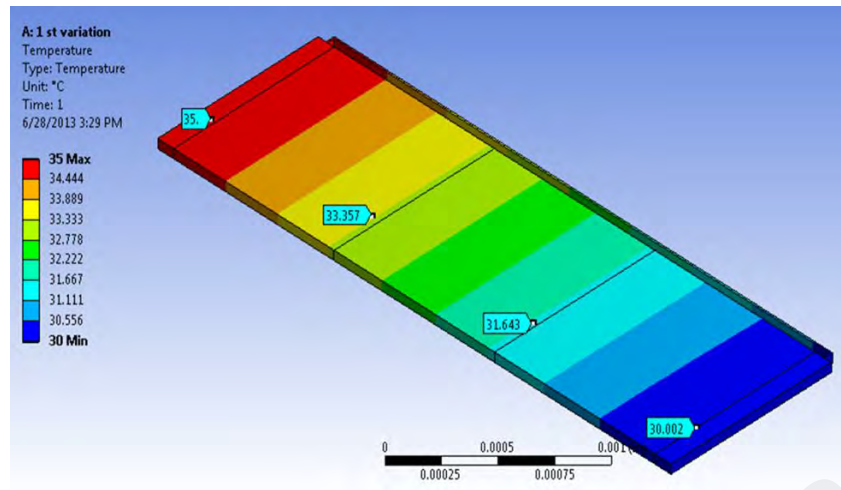


Figure 4.8: Temperature distribution for a single leg n-type thermoelectric in Case 1.

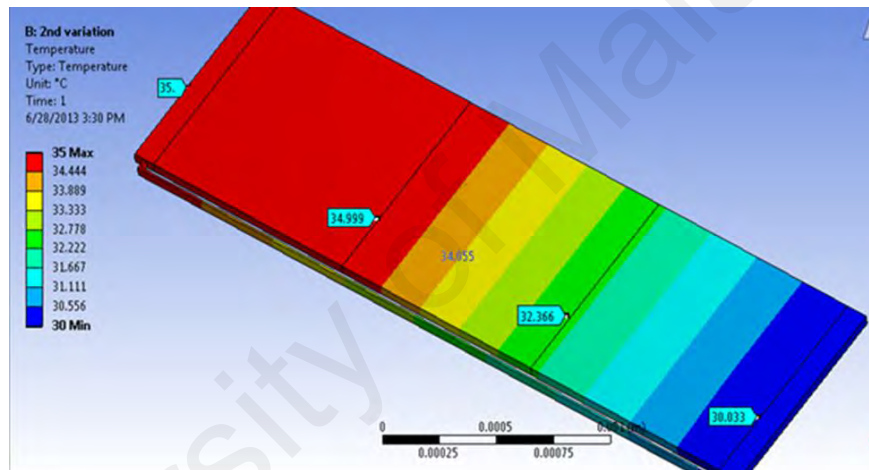


Figure 4.9: Temperature distribution for a single leg n-type thermoelectric in Case 2.

4.1.2 Thermoelectric Power Output of Graded Multilayer Solar Funnel STEG

4.1.2.1 Effect of Contact Resistance

The thermoelectric performance for a single thermoelectric junction, p and n-type columns for a graded multilayer containing parameters listed in Table 3.2. The Seebeck coefficients for the p- and n-type columns are assigned as equal but opposite signs. The contact resistance between the thermoelectric material and the electrodes are taken to be 5% of the resistance of the thermoelectric legs, as Kraemer et al (Kraemer, Poudel, Feng, Caylor, Yu, Yan, Ma, Wang, Wang, Muto, et al., 2011) have shown that the contact

resistance of 5% degrades the system efficiency by 0.23%. The variation of Seebeck voltage, resistance, current and thermoelectric device power output are shown in Figure 4.10-13, where a plot of these respective parameters as a function of contact resistance percentage indicates the losses due to the contact resistance. Performance of Case 1 and Case 2 are also compared against a standard bismuth telluride junction, as shown in the table 4.1.

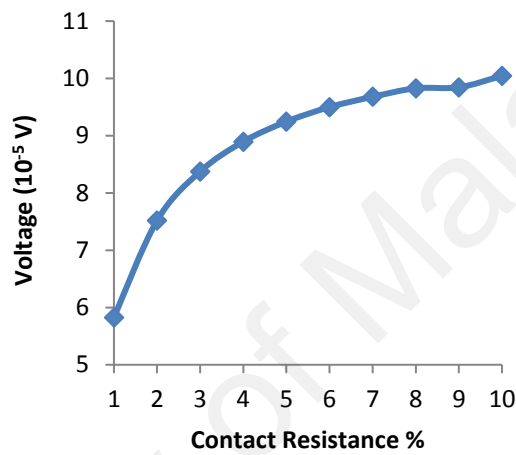


Figure 4.10: Voltage output of multilayer thermoelectric device in response with contact resistance.

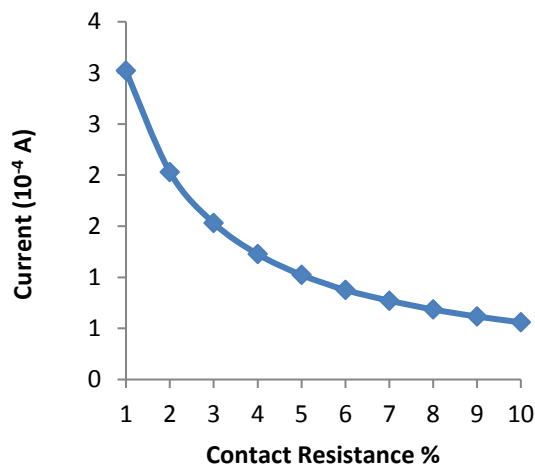


Figure 4.11: Current output of multilayer thermoelectric device in response with contact resistance.

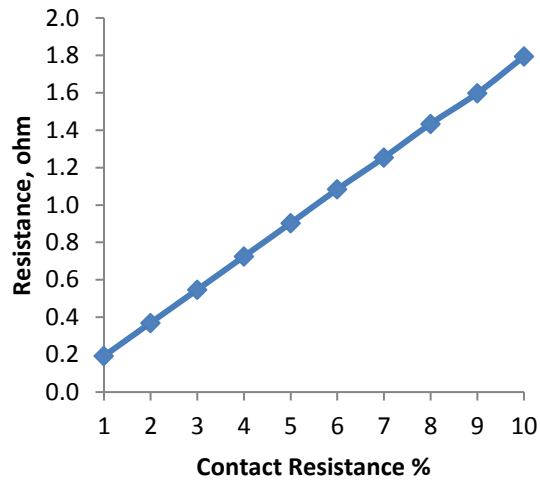


Figure 4.12: Overall multilayer thermoelectric device resistance in response with contact resistance.

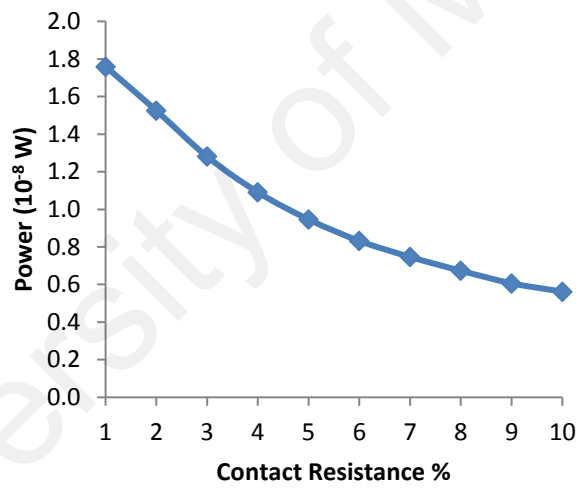


Figure 4.13: Power output of multilayer thermoelectric device in response with contact resistance.

Table 4.1: Thermoelectric Devices Power Output

	Voltage (V)	Current (A)	Power (W)
Case 1	1.21E-05	6.82E-04	8.27E-09
Case 2	8.20E-06	4.56E-04	3.74E-09
BiTe	1.30E-05	8.76E-03	1.14E-07

For a single thermoelectric junction, using parameters listed in Table 4.1, the obtained voltage for the best power output was 1.21×10^{-5} V and the current output was 6.82×10^{-4} A. Given that the cross-sectional area for the junction is 0.05 mm x 3 mm, the calculated power density for a single junction of this design is $5.5 \mu\text{W}/\text{cm}^2$. Comparison of the performance of this design against the performance of other low power TEGs application obtained from literature is as listed in Table 2.2 in section 2.4.

From this section, it has been identified that the minimum requirement for a power density of $5.5 \mu\text{W}/\text{cm}^2$ will require approximate Seebeck coefficient of $\sim 40 \mu\text{V}/\text{K}$, electrical conductivity in the range of hundreds to kilos S/cm, and thermal conductivity of the order $10^{-1} \text{ W}/\text{m.K}$ the very least. The next section will discuss on thermoelectric properties of different types of hybrid-polymer-LCs and DLCs as potential candidates for STEG application. Firstly a PELC and secondly variations of DLCs' mixtures. The electrical conductivity and Seebeck coefficient were tuned by different types and concentrations of LCs. The optical band gap will be studied in term of addition of different types of LCs at different concentrations.

4.2 Temperature Dependent Properties of the Polymer-Electrolyte-Liquid Crystals (PELC) Systems

In this section, the temperature dependent properties of a new concept of hybrid materials is discussed. As can be seen from earlier section, the power density of a thermoelectric device for miniaturised application requires at least $1 \times 10^{-2} \text{ W/m}^2$. The thermoelectric materials that is capable to deliver such capacity of power density are being explored widely. Polymer materials such as carbazole which has been selected in the previous studies is the testament to the feasibility of employing semiconductor of organic and polymeric class for TEG. However, the exploration should be expanded to a new class of materials, i.e. hybrid polymer liquid crystals, it is essential for them to be able to compete with conventional semiconductors in order to power up thermoelectric devices at the required specifications.

Regular polymer electrolytes consist of polymer and ionic salts solution which are able to conduct electricity due to free ions. Polymer electrolytes materials have been used in batteries, capacitors and photovoltaics cells. A new study by Jiao et al. have even introduced a new 'thermoelectric paper' which are able to function as flexible thermoelectric generator. Ionic thermoelectric Seebeck coefficient of mV order has been observed, with improved electrical conductivity which are rarely seen in the trend for ionic compounds.

In this study, nematic liquid crystal is used as plasticiser to enhance electrical conductivity of non-conducting PVA polymer. 5CB liquid crystal is added to the polymer electrolyte mixture to fabricate polymer electrolyte liquid crystal (PELC) mixtures. It has been observed the role of added nematic LC to the PVA-KI compound is much more than that. The electrical conductivity and Seebeck coefficient have been shown to correspond to the phase dependent nematic LC.

4.2.1 Polymer Electrolyte System (PVA+KI)

The concept of a polymer electrolyte is revisited as a starting point. Polymers as a host for ionic salts have been known for many years now due to their advantages in energy conversion devices, fuel cell, batteries and many others. They have high electrical conductivity and excellent stability. In this work, before the LC behaviour is studied, a baseline prior to the PELC study was created. The first measurement on PVA-KI system provides a baseline for the investigation on PELC: the room temperature electrical conductivity of non-conducting PVA polymer with KI electrolytes served as standard measurement in comparison with the electrical conductivity of PELC.

The maximum electrical conductivity has been observed in PVA-KI sample when the PVA percentage is at 60% and KI percentage is around 40% in Figure 4.14. At lower percentage of KI electrolyte, the activation energy required to overcome the band gap and become free to conduct is still low in comparison with the energy that has been acquired when the mixture of ample percentage of KI electrolyte has been added. Over 40% KI electrolyte percentage, the mobility pathway has been obstructed due to the scattering of carrier as observed in most cases involving high concentration dopants, hence decreasing its electrical conductivity.

4.2.2 Polymer-Inorganic (additive) Electrolyte System (PVA+KI+ZnO)

PVA served as the host materials for various concentration of KI electrolyte in four samples with the following ratio ZnO:PVA:KI=1:100-x: x ($x=20, 30, 40, 50$) has been prepared. Zinc Oxide (ZnO) powder as additive has been added to the polymer and electrolyte mixtures. The ZnO was found to be aggregated in the mixture with PVA concentration lower than 50%. ZnO particles are expected to provide the conducting pathway alongside the electrolyte. In Figure 4.14, the electrical conductivity

measurement has indicated that the ZnO additive added is not an effective charge carrier enabler.

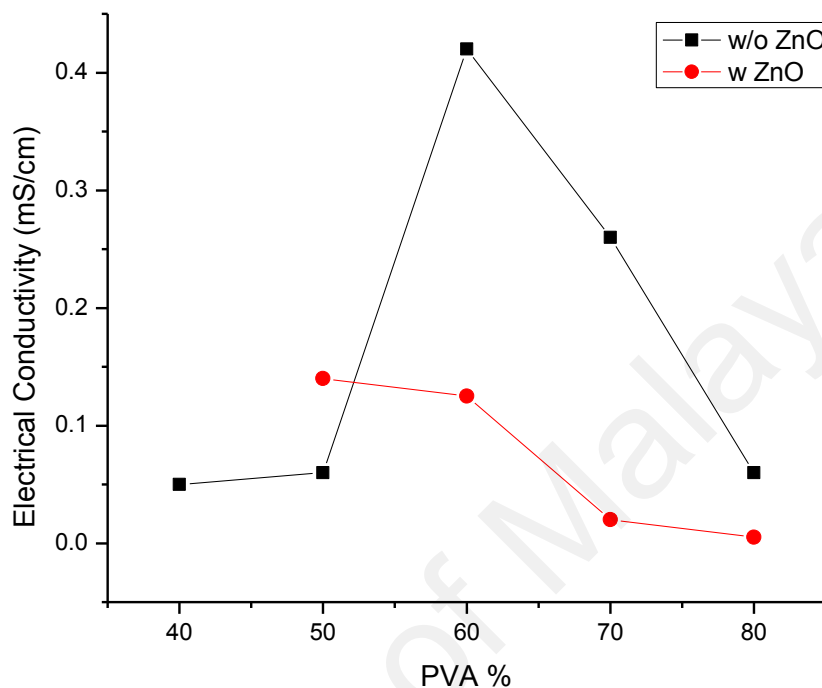


Figure 4.14: Electrical conductivity measurement of PVA polymer-KI electrolyte with and without ZnO as additive

It has been observed that the addition of ZnO powder has suppressed the electrical conductivity polymer electrolyte systems. The electrical conductivity of the PVA-KI-ZnO mixtures have been found lower than the electrical conductivity of PVA-KI mixtures except at 50% PVA and 50% KI concentration. A softer conduction mechanism through thermotropic nematic liquid crystals addition is suggested and its performance is demonstrated in the next section.

4.2.3 Polymer Electrolyte Liquid Crystals System (PVA+KI+5CB)

The function of 4-Cyano-4'-pentylbiphenyl (5CB) as a plasticizer in polyvinyl alcohol (PVA) as the polymer matrix is studied in DSC analysis, electrical and thermal conductivities, and Seebeck coefficient measurements. The 5CB was selected due to its

function as a plasticizer, typically, favoured to be a highly polar molecule. The polarization within the 5CB can induce electron-hole pairs in the PVA close to the 5CB, and electron and/or hole carriers may transport in the PELC mixture. Below the crystalline transition temperature of 18 °C, the 5CB acts like a normal crystalline solid. It only possesses one liquid crystal subphase, which is the nematic phase between 18 °C and 35 °C. In the nematic phase, the liquid crystal shows a high degree of orientational order. Above the transition temperature of 35 °C, it enters the isotropic phase and loses its orientational order.

4.2.3.1 Differential Scanning Calorimetry, DSC

Figure 4.15 provides the DSC curves of the 5CB-free and PELC mixtures. The 5CB contents in the PELC mixtures are 0, 5, 10, 15, 20, and 25%. Endothermic dips in the curves marked with arrows corresponded to the nematic-isotropic transition. Overall, it can be seen that the increase of 5CB in the PELC mixture tended to reduce the nematic-isotropic transition temperature of the 5CB, which is a well-established observation when a nematic liquid crystal is mixed with a polymer (Gorkunov et al., 2013). This is because the surface interaction between the 5CB and PVA induced a higher degree of disorder into the liquid crystal, and thus a lower energy/temperature was required for transition from the nematic to isotropic phases.

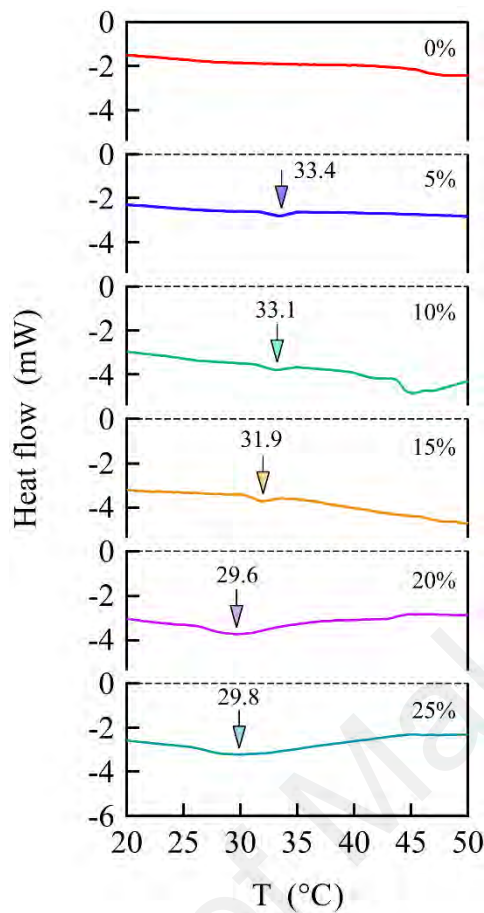


Figure 4.15: DSC curves for the PELC mixtures (5CB contents are 0, 5, 10, 15, 20, and 25%). The nematic-isotropic transition temperature for each PELC mixture is also shown

4.2.3.2 Electrical Conductivity

The electrical conductivity of the PELC mixtures as a function of temperature is shown in Figure 4.16. For comparison, the electrical conductivity of the 5CB-free mixture is also shown. With increasing temperature, the electrical conductivity of the 5CB-free mixture slightly increased. The increasing trend can be explained in terms of a thermally-activated hopping transport model expressed as $\sigma \propto \exp(-\frac{E}{k_B T})$, where E and k are the activation energy and Boltzmann constant, respectively. The nematic-isotropic transition temperature of the PELC mixtures is indicated by arrows. It is noted that the electrical conductivity of the PELC mixtures also exhibited the increasing trend, but transiently decreased around the transition temperature. The thermally-activated carrier transport occurred both in the nematic and isotropic phases. The reason for the transient decrease

around the transition temperature can be attributed to higher carrier scattering due to the loss of ordering of 5CB in the isotropic phase compared to the nematic phase. In other words, the carrier mobility was reduced through the nematic-isotropic phase transition.

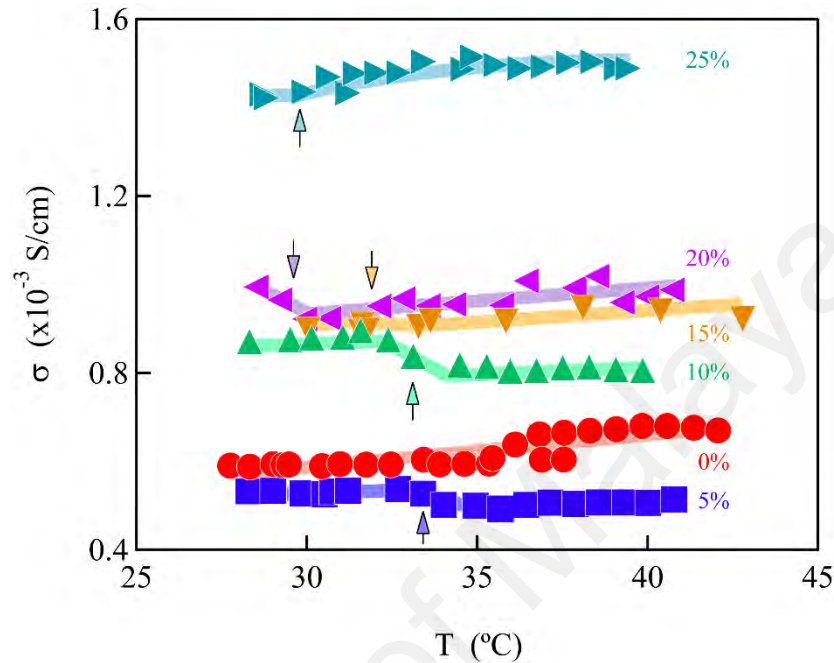


Figure 4.16: Electrical conductivity of the PELC mixtures (5CB contents are 0, 5, 10, 15, 20 and 25%). The nematic-isotropic transition temperatures are also shown in the figure

By cross-referencing the electrical conductivity for each composition, a strong correlation to the 5CB content is observed: the electrical conductivity tended to increase with increasing the 5CB content. This is due to the increase of conduction carrier concentration (the conduction carrier is electrons as discussed later) induced by the polarization of the 5CB. In the case of low 5CB concentration, the dispersion of 5CB in PVA may also prevent the carrier transport, which accounts for the lower electrical conductivity of the 5% 5CB-doped PELC mixture compared to the 5CB-free mixture.

4.2.3.3 Seebeck Coefficient

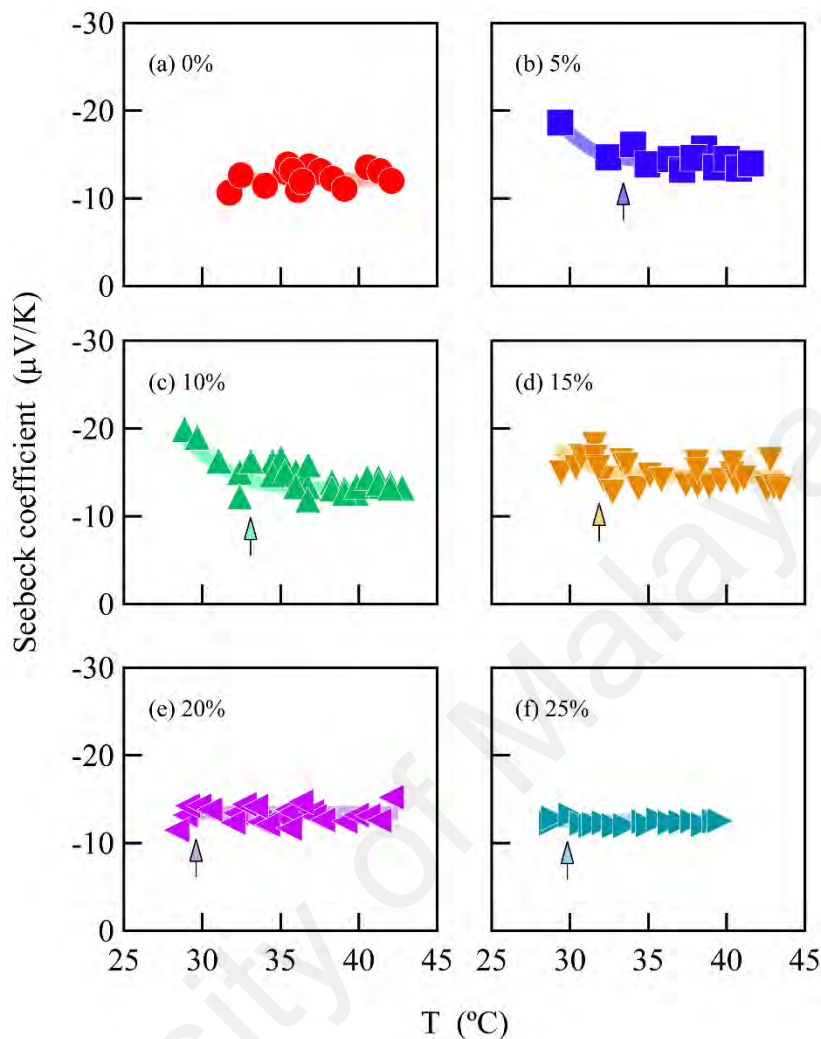


Figure 4.17: Seebeck coefficient vs temperature for the different PELC mixtures (5CB contents are 0, 5, 10, 15, 20 and 25%). The nematic-isotropic transition temperature is also shown in each figure

Figure 4.17 shows the Seebeck coefficient of the 5CB-free and PELC mixtures as a function of temperature. The negative values of the Seebeck coefficient indicate that the electron transport is dominated by the lowest unoccupied molecular orbital (LUMO) of PVA (Baheti et al., 2008; Paulsson & Datta, 2003), i.e., the dominant charge carrier are electrons, which are induced in the PVA through the KI and 5CB doping. Preliminary Hall effect measurements also confirmed that electrons are the conduction carrier. The temperature dependence of Seebeck coefficient is explained by the hopping transport, $S = -(E_C - E_F)/eT$, where E_C , E_F and e are the energy level of LUMO, Fermi energy, and

elementary charge, respectively. Since the temperature range measured was narrow, the Seebeck coefficient of 5CB-free mixture was almost constant independent of temperature. The arrows in Figure 4.16 and Figure 4.17 denote the nematic-isotropic transition temperature of the corresponding PELC mixtures. Similar to the 5CB-free mixture, the PELC mixtures exhibited constant Seebeck coefficient above nematic-isotropic transition temperature. The Seebeck coefficient at the isotropic phase was nearly equal to that of the 5CB-free mixture, indicating that the energy level of LUMO did not change by the 5CB doping.

It is noted that the absolute value of Seebeck coefficient at the nematic phase tended to be higher than that at the isotropic phase for the PELC mixtures. The decrease of Seebeck coefficient from the nematic phase to the isotropic phase can be attributed to the order-disorder transition reported in literatures (Gascoin & Maignan, 2011; Kaltzoglou et al., 2008; Kirkham et al., 2011). For the PELC mixtures, the nematic-isotropic transition corresponds to the order-disorder transition, leading to the decrease of Seebeck coefficient. Since the electrical conductivity also decreased at the nematic-isotropic transition temperature as explained above, the 5CB can be used as a temperature switch.

4.2.3.4 Thermal Conductivity Measurement

To further investigate an effect of 5CB, we estimated dimensionless figure of merit, ZT , using the thermal conductivities at 29 °C as listed in Table 4.2. One can see that the thermal conductivity decreased as a function of 5CB content probably due to the enhanced phonon scattering by the increase of 5CB in the PELC mixtures.

Table 4.2: Thermal conductivity of the 5CB-free and PELC mixtures at 29 °C.

5CB content (%)	0	5	10	15	20	25
1(W/Km)	0.214	0.189	0.164	0.139	0.114	0.089

4.2.3.5 Dimensionless Figure of Merit, ZT

The estimated ZT of the 5CB-free and PELC mixtures at the lowest and highest measurement temperatures are shown in Figure 4.18. The lowest temperature was 28.6-31.7 °C where the 5CB was in the nematic phase. On the other hand, the 5CB was in the isotropic phase at the highest temperature of 39.3-43.4 °C. As for the 5CB-free mixture, ZT at the highest temperature was higher than that at the lowest temperature, mainly reflecting the increase of electrical conductivity with increasing temperature.

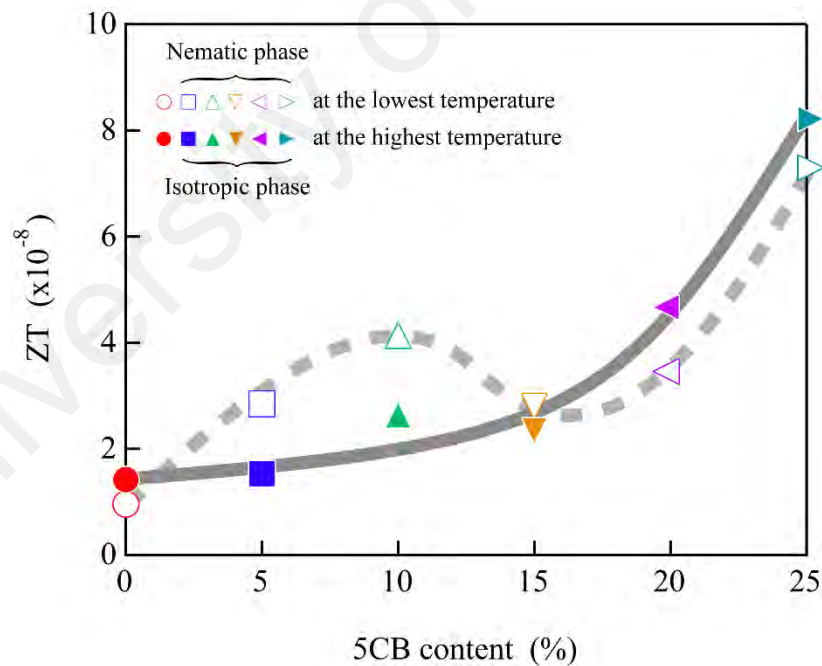


Figure 4.18: ZT value of the PELC mixtures as a function of 5CB content at the lowest and highest temperatures. Gray dotted and solid lines are guide for the eyes to show a trend of ZT at the lowest and highest temperatures, respectively

In contrast, the 5-15% 5CB doped PELC mixtures showed lower ZT at the highest temperature than at the lowest temperature due to the decrease of electrical conductivity

and Seebeck coefficient above the nematic-isotropic transition temperature. This result demonstrated that the 5CB acted as the temperature switch: the magnitude relation between ZT values at the lowest and highest temperatures was inverted through the use of nematic-isotropic transition of 5CB. The PELC mixtures may be used like a thermistor. Although the 20 and 25% 5CB doped PELC mixtures also exhibited the nematic-isotropic transition, the ZT value at the highest temperature was higher than that at the lowest temperature similar to the 5CB-free mixture. This is because the nematic-isotropic transition temperature of these PELC mixtures was near the lowest temperature, i.e., the effect of 5CB was diminished. In this study, the highest ZT of 8.2×10^{-8} was obtained for the 25% 5CB doped PELC mixture. Although this value is considerably low for application to the TEG, the enhancement of ZT relative to the 5CB-free mixture reached about six times. The reason for this enhancement was the increase of electrical conductivity by the 5CB doping. The ZT value of the PELC mixture can be further improved by using another liquid crystal whose nematic-isotropic transition temperature is sufficiently higher than the 5CB. It is expected that the use of liquid crystals is a potential strategy for increasing the thermoelectric potential of a polymer electrolyte mixture.

As a conclusion, it has been observed that the strategy of incorporating self-assembled LC molecules can enhance the performance of conducting polymers. This is potentially suitable in application such as STEG where enhanced thermoelectric properties would be an attractive choice of material. Thus, further studies on self-assembled liquid crystals with efficient charge transport ability will be investigated in the following section. The electrical conductivities of different variations of DLCs mixtures will be studied by using temperature dependent measurement techniques due to the thermotropic properties of DLCs.

4.3 Temperature Dependent Properties of Discotic Liquid Crystal (DLC) Systems

In this section, the temperature dependent electrical conductivity of discotic liquid crystal (DLC) systems are investigated. DLC materials possessed thermotropic and also anisotropic attributes which both governed most of their electronic, optical and mechanical behaviours. Although they have very low intrinsic charge carriers, their ability to transport charge carriers efficiently were described in many studies (Kumar, 2016). Due to the temperature manipulation of the materials, the reorganisation, realignment, orientational and translational orders were observed, as feedback response to the temperature. The reorganisation of the alignment has been found to improve electrical and electronic properties of DLC materials. This ability is found to be useful and very attractive in electronic and opto-electronic applications.

In this work, the thermoelectric properties of HAT10 discotic liquid crystals were measured. The electrical conductivity of HAT6 and HAT10 were compared. The electrical conductivity of HAT6 DLC with addition of various mixtures of different type of liquid crystals were also investigated. The effect of electrodes was highlighted and compared for the investigated mixtures. The ionic dopant AlCl_3 has been added to HAT6 DLC in order to investigate the enhancement in electrical conductivity of HAT6.

4.3.1 HAT10

4.3.1.1 Investigation on Mesomorphic Properties by POM

Generally, DLC materials are optically birefringent and made up of anisotropic fluids which transform into various phases at elevated temperature. Each mesophase shows a typical texture at different transition temperature. From the experiment, it was observed from optical polarizing microscope that HAT10 is in solid crystal state at room temperature as seen in Figure 4.19 (left). Due to the nature of how the HAT10 was

fabricated in this experiment, the columnar phase which is the typical homeotropic alignment in DLC was not expected. The planar alignment is favourable on the air-interfaced substrate. The competing energy affinity of the ‘face on’ surface and ‘side on’ surface determines the kind of arrangement interfacial interaction exist.

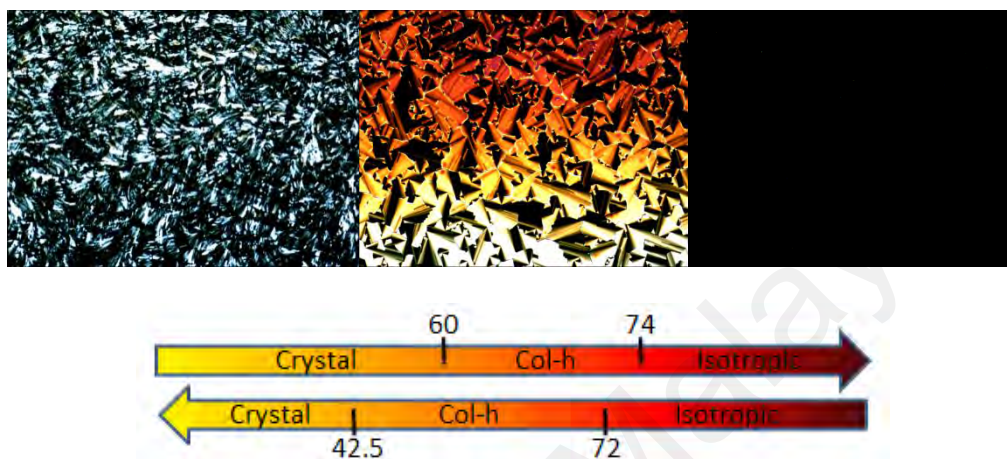


Figure 4.19: Optical textures of HAT10 compound under POM, Cr phase (left), planar alignment in liquid crystalline phase (middle), Iso phase (right).

The transition from crystal structure to planar alignment occurred at 60 °C during heating process. Conic fan-shaped (pseudofocal conic) is the characteristic of a planar alignment has been shown in Figure 4.19 (middle). This has proven that the planar alignment is predominantly achieved in spin coated DLC materials. Isotropization occurred at 74 °C as seen in Figure 4.19 (right) at which the light was blocked from all directions as there was no molecular ordering because the heating process had driven them into conventional liquid phase. The observed textures were resulted from the interlayer movement of the stacking molecules.

4.3.1.2 Differential Scanning Calorimetry, DSC

The phase transitions were studied by differential scanning calorimetry. The transition peak showed quite consistent with the observed transitions trend by using optical polarizing microscope especially during cooling cycle as shown in Figure 4.20. The deviation in heating cycle has been probably caused by air convection on the air interface

on the coating surface. The increased in magnitude of the transition enthalpies upon cooling implies better ordering in liquid crystalline state in materials during phase transition. The alignment of molecular ordering in columnar phase was improved when the discotic liquid crystals were cooled down from high temperature.

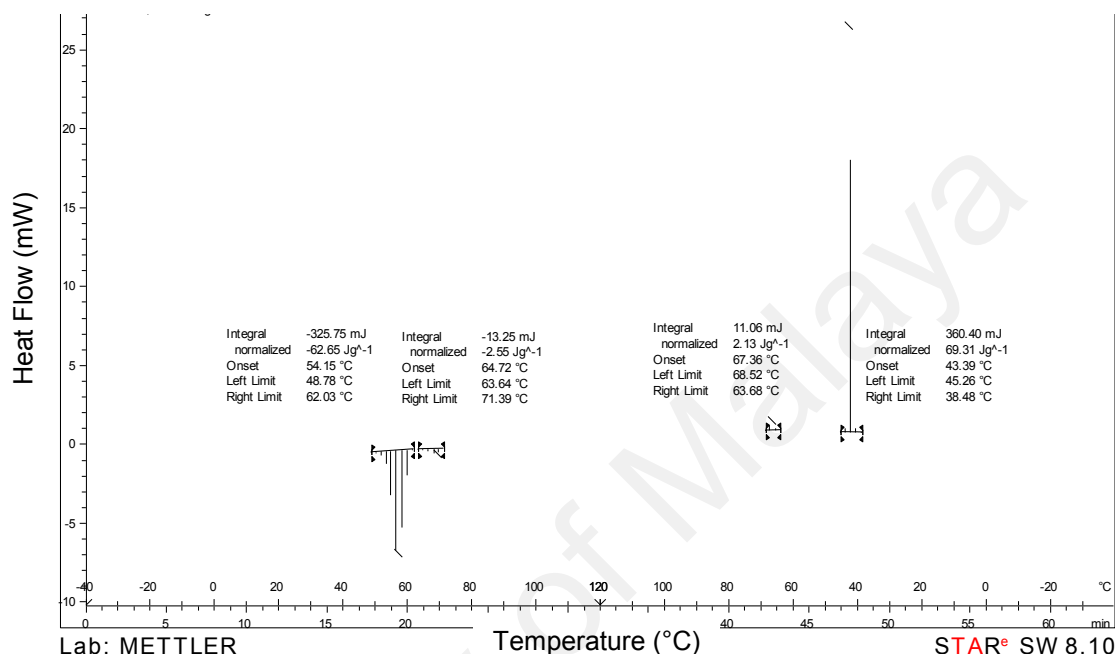


Figure 4.20: DSC thermogram of HAT10 compound

Table 4.3: Summary of transition temperature and enthalpies for HAT10.

Process	Temperature, °C	Phase Transition	ΔH , J/g
Cooling	43.4	LC - Cr	69.3
	67.4	Iso - LC	2.1
Heating	54.2	Cr - LC	62.7
	64.7	LC - Iso	2.6

4.3.1.3 Electrical Conductivity

(a) *Van der Pauw Technique (Laboratory Fabricated Setup)*

Electrical conductivity of the spin coated HAT10 on ITO substrate was measured by using Van der Pauw technique with two different setups. Firstly, laboratory fabricated setup, and secondly Ecopia-HMS 3000 Hall Measurement System. In the first measurement using laboratory fabricated setup, the electrical conductivity was found to

be increased when heated from room temperature until approximately 60 °C, before the electrical conductivity declining steadily as shown in Figure 4.21.

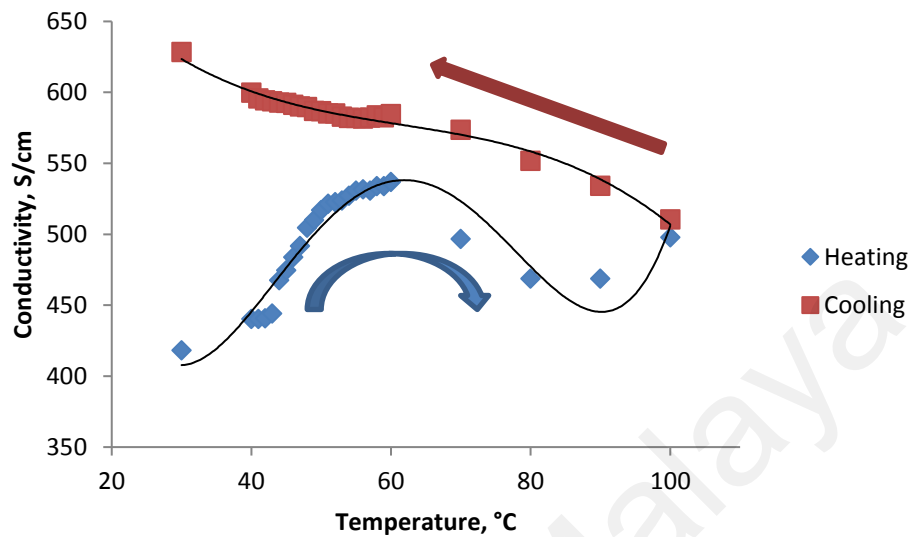


Figure 4.21: The measurement of temperature-dependent electrical conductivity of HAT10 on ITO substrate during heating and cooling cycles using Van der Pauw setup. The arrows indicated the progress sequence of the measurement which goes from room temperature to 100 and back to room temperature again.

The decreased has been observed to occur during melting process from 60 °C until isotropic point. Beyond the isotropic point, the secondary effect due to the fluctuation in ordering has caused the electrical conductivity to be slightly increased. When the sample was cooled down from melting point to room temperature, the electrical conductivity has been observed to be increased steadily. This behaviour can be associated with the thermotropic property of DLCs; during heating, the melting in alkyl chains subsequently has caused the disorder in DLC materials, and has deterred the mobility of the charges. However, upon cooling process, the reorganisation of the DLC molecules in liquid crystalline phase has caused the mobility of the charges to be restored.

(b) Ecopia HMS-3000 Hall Effect Measurement System

The second measurement by using Ecopia-HMS 3000 Hall Effect Measurement System is capable of measuring the electrical conductivity and the mobility of HAT10

DLC materials. However, this setup is only capable of measuring the temperature-dependent property up until 75 °C. In Figure 4.22 and 4.23, the electrical conductivity and the mobility results of bared ITO coated substrate were measured and plotted together with the results of spin coated HAT10 on ITO substrate.

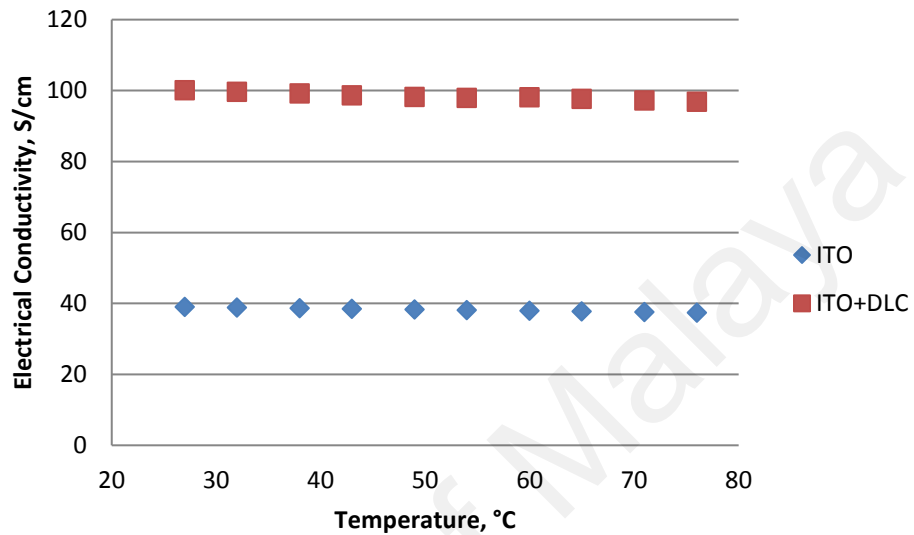


Figure 4.22: Electrical conductivity measurement of spin coated HAT10 on ITO substrate

It has been observed that the electrical conductivity during heating process is steady from room temperature until 75 °C. The magnitude of increment in electrical conductivity and mobility measurement of HAT10 DLC material on ITO substrate was found to be more than twice than that of the bared ITO coated substrate.

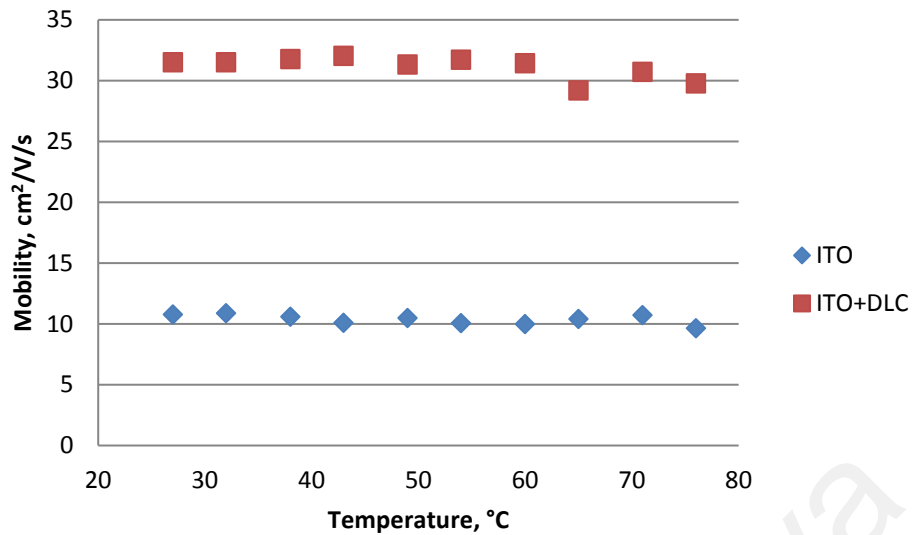


Figure 4.23: Mobility measurement of spin coated HAT10 on ITO substrate

Figure 4.24 shows the result of Seebeck coefficient measurement. The Seebeck coefficient at each temperature point was evaluated from a plot of generated Seebeck voltage against temperature difference as illustrated in Figure 4.24 at the bottom right. The generated potential difference must be sufficiently linear so that the Seebeck coefficient can be derived from the slope of the plot. Normally, only the plot evaluated at linearity of 90% and above is considered acceptable. The temperature recorded in the plot is referred to the absolute temperature or average temperature between hot side and cold side of the sample during measurement.

It has been observed that the Seebeck coefficient rose from room temperature until approximately 40 °C, and dropped beyond that temperature. This trend can be correlated with the role of potential energy in defining Seebeck coefficient from thermodynamic first-principles. It has been shown in Figure 4.21, in the earlier section that the electrical conductivity of the sample in this range of temperature (room temperature to 60 °C) was found to be increasing. The potential energy has been used up to move the carriers from the hot side of the electrode to the cold side. The result of this was the increased in kinetic mobility, at the expense of Seebeck coefficient. The decline in the Seebeck coefficient is learned to be caused by the phase difference of HAT10 at the hot side and the cold side.

At an absolute temperature of 40 °C, the hot side temperature is found to be 55 °C, at which HAT10 was in liquid crystalline phase, and the cold side was well in crystalline state. The mismatch of the phase has caused the Seebeck coefficient to be reduced as the electronic mobilities which was supposed to contribute to the Seebeck coefficient, fluctuated.

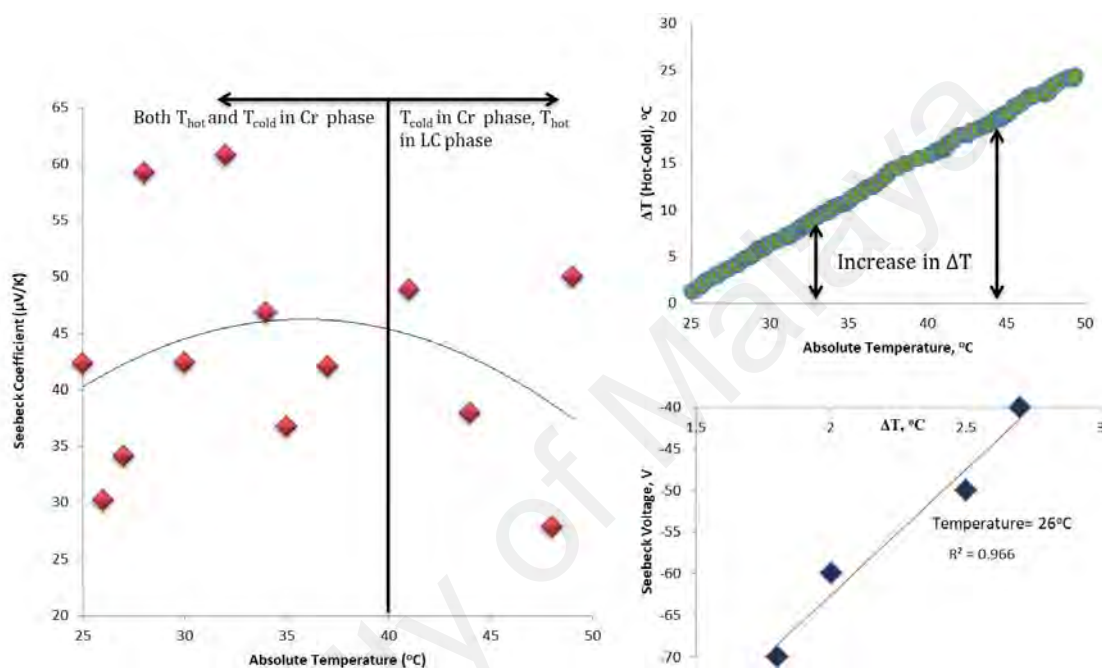


Figure 4.24: (left) Seebeck coefficient measurement of HAT6 coated on ITO substrate. (top right) The plot of absolute temperature calculated by averaging T_{Hot} and T_{Cold} against the temperature difference, ΔT. (bottom right) Determination of Seebeck coefficient from the plot of Seebeck voltage against ΔT, i.e. all the points corresponded to absolute temperature of 26 °C.

4.3.2 HAT6

4.3.2.1 Investigation on Mesomorphic Properties by POM

Figure 4.25 shows the mesomorphic images of the HAT6 as a function of temperature as observed under the polarising optical microscope (POM). It was observed that HAT6 molecules are arranged in amorphous solid crystal at room temperature as seen in Figure 4.25 (left). The transition from Cr structure to *D_h* phase occurred at 70 °C during heating process. The fan-shaped structure is the characteristic of *D_h* mesophase, as shown in Figure 4.25 (middle). In a heating cycle, isotropization occurred at 102.5 °C as seen in

Figure 4.25 (right) where the polarized light is blocked once the DLC enters the Iso state. The observed textures were resulted from the symmetry-dependent elasticity of the liquid-crystalline phase in combination with defects and the surface conditions of the sample.

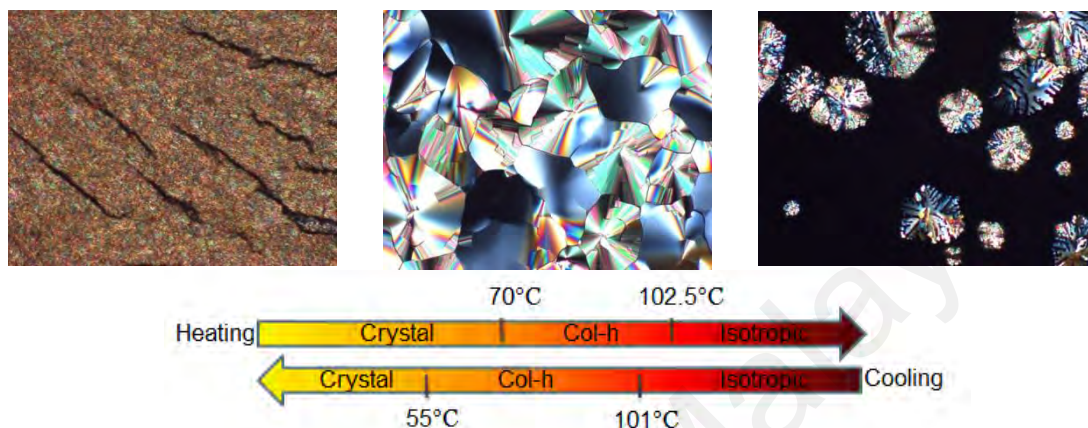


Figure 4.25: Optical textures of HAT6 compound under POM, Cr phase (left), D_h phase (middle), a spur of transition from D_h into Iso phase (right).

4.3.2.2 Differential Scanning Calorimetry, DSC

Additionally, the phase transitions were identified by differential scanning calorimetry (DSC) as shown in Figure 4.26 and the results were summarized in Table 4.4. The two peaks appeared during the cooling DSC scan at 97.9 °C and 54.3 °C which corresponds to transition from Iso phase to D_h phase and from D_h phase to Cr phase respectively. The heating scan resulted the two peaks at 66.7 °C and 97.9 °C which corresponded to transition from Cr phase to D_h phase and from D_h to Iso phase. The transition peak shows consistent results as observed under the polarizing optical microscope.

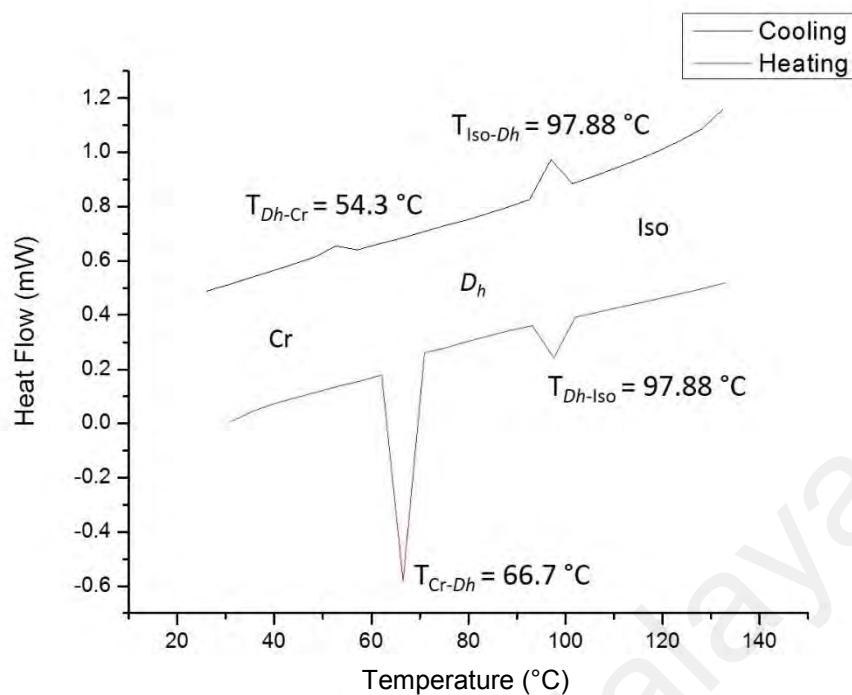


Figure 4.26: DSC thermogram of HAT6 compound

Table 4.4: Summary of transition temperature and enthalpies for HAT6.

Process	Temperature, °C	Phase Transition	ΔH , J/g
Cooling	54.3	D_h -Cr	56.9
	98.0	Iso- D_h	7.0
Heating	66.7	Cr- D_h	52.8
	97.9	D_h -Iso	7.0

4.3.2.3 Electrical Conductivity

The dc-conductivity studies show that the electrical conductivity of discotic liquid crystal materials is enhanced in the discotic columnar liquid crystalline phase as shown in Figure 4.27. Many of organics and liquid crystals polymers are found to be p-type semiconductors. In the p-type semiconductors, efficient holes transport mechanism is very important. The charge transport is enhanced in self-assembly systems such as DLCs, which the stacking of π^* - π^* orbitals in columnar stacks will result in quasi 1D charge transport.

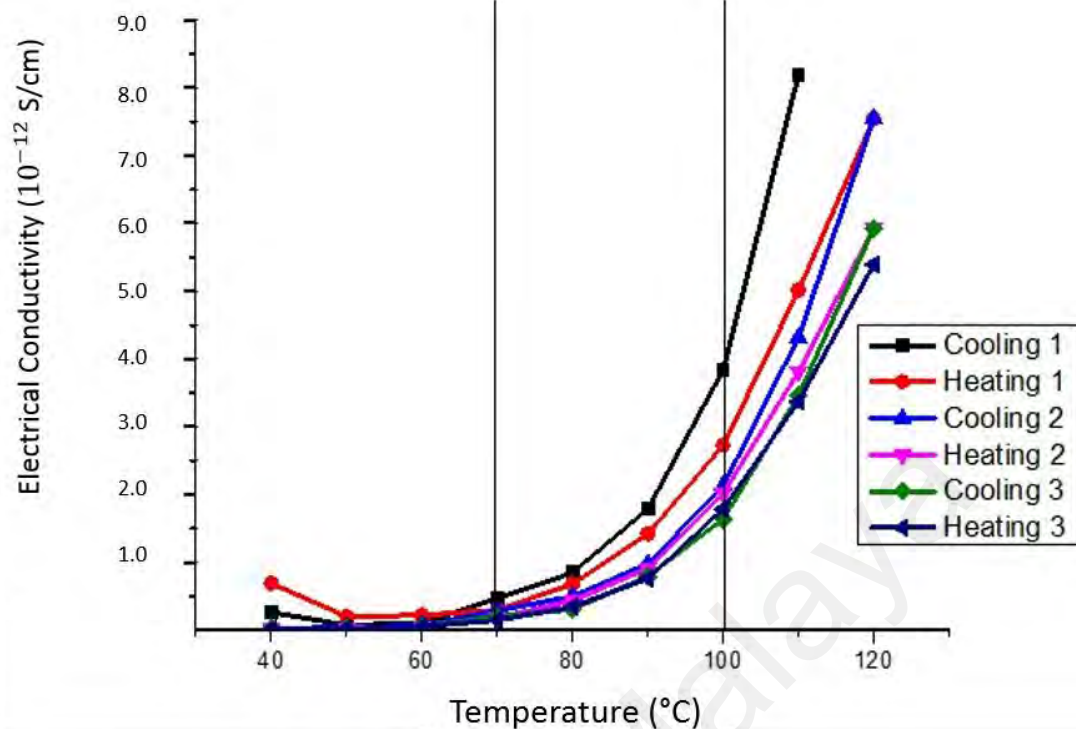


Figure 4.27: Temperature-dependent electrical conductivity of HAT6 during cooling and heating cycles.

4.3.3 HAT6, Smectic and Ferroelectric Ternary Liquid Crystals Mixtures

It was hypothesised that the smectic A (8/2) and ferroelectric (siloxane-based) liquid crystals could stabilise the columnar formation by filling in the space between the disc columns and tessellating over the columnar stacks-ITO substrate interface. This is the nature of any planar molecules which have been used as doping materials in DLC systems. Thus, the stability of the column will be reflected in the electrical conductivity measurement.

4.3.3.1 Investigation on Mesomorphic Properties by POM

The phase transition of ternary LC mixtures has been studied by using POM. At 20% HAT6 content, no specific liquid crystalline pattern has been observed other than the formation of liquid crystalline islands at room temperature as shown in Figure 4.28. The islands disappeared when entering isotropic phase. However, samples with higher percentages of HAT6, i.e. 40%, 60% and 80% have shown higher degree of crystallinity

at room temperature as shown in Figure 4.29, 4.30 and 4.31. The formation of spherulitic shaped (brushes) or maltese cross pattern has been the characteristics of some calamitic and even discotic liquid crystals, due to their elongated shape. The maltese cross pattern as seen in Figure 4.29 was the result of nucleation of the crystals. The size of the spherulites (cross pattern) depends on the cooling rates used. The discotic focal fan shape pattern has not been observed due to the dominant intermolecular forces between the smectic and ferroelectric LCs.

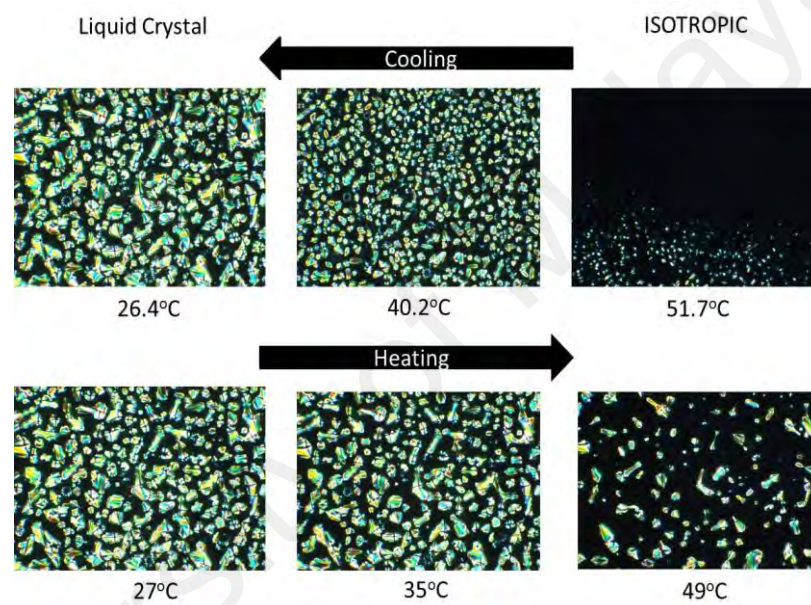


Figure 4.28: POM of sample with 20% of HAT6 content in LC mixtures.

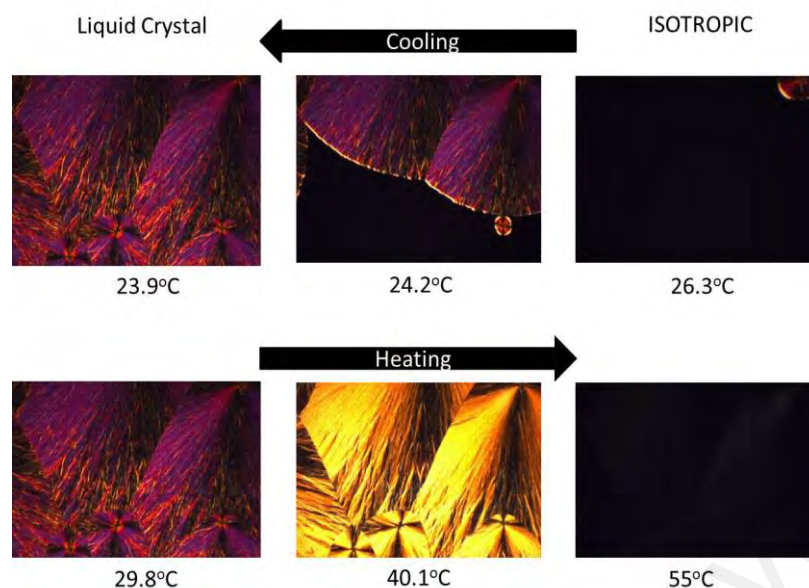


Figure 4.29: POM of sample with 40% of HAT6 in LC mixtures. Maltese cross pattern has been observed due to nucleation of crystal.

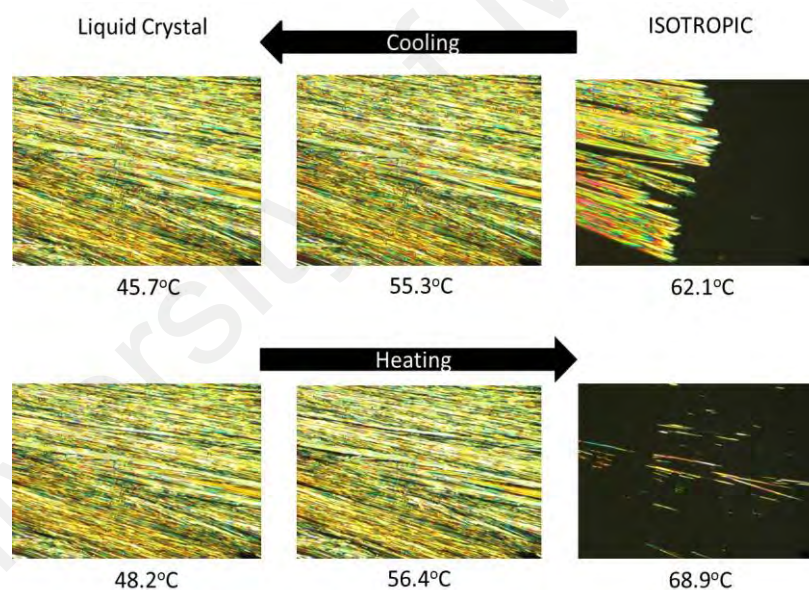


Figure 4.30: POM of sample with 60% of HAT6 in LC mixtures. The brushes have been observed to grow in single direction.

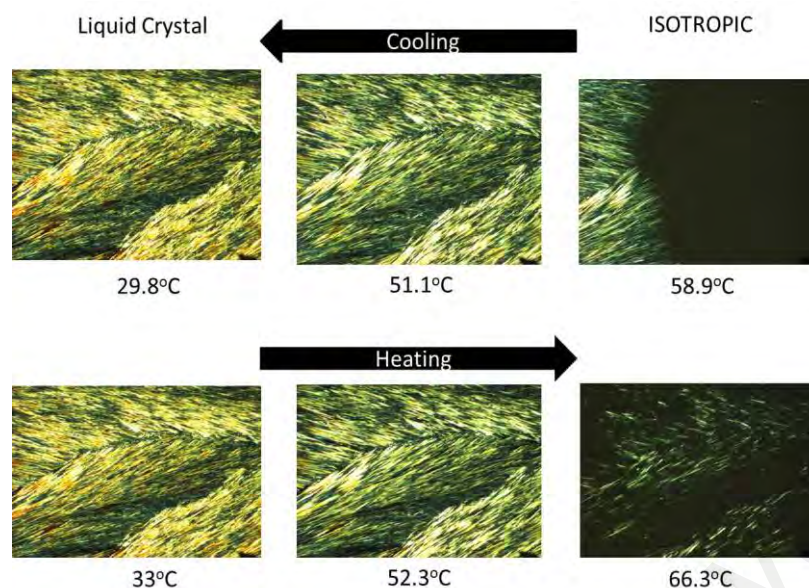


Figure 4.31: POM of sample with 80% of HAT6 in LC mixtures. The brushes have been observed to interwoven each other.

4.3.3.2 Differential Scanning Calorimetry

The phase transition of the ternary LC mixtures has been confirmed by using DSC experiment. From earlier section, it has been established that the liquid crystalline transition of HAT6 DLCs is within the range of 70 to 100 °C. When the smectic and ferroelectric LCs were mixed together, none of the HAT6 DLCs attribute has been observed. The calamitic LCs has the dominant dynamics in the mixtures even at the percentage much lower than the DLCs itself. It has been apparent that the smectic and ferroelectric LCs exhibit the liquid crystalline behaviours well below room temperature. When compared with POM images in the previous section, not all the peaks were very discernible in POM investigations. The stabilities of the compound can be observed clearly from the DSC thermograms for each mixture.

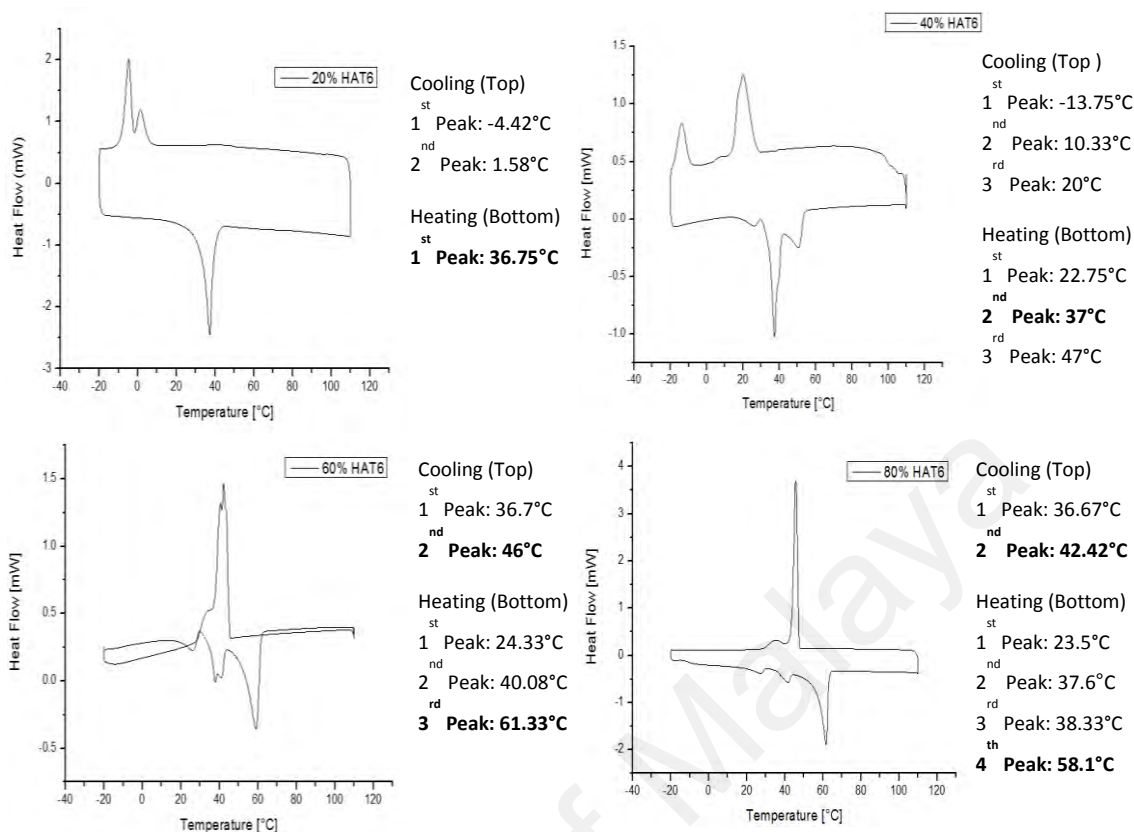


Figure 4.32: DSC thermograms of liquid crystal mixtures.

4.3.3.3 Electrical Conductivity

In Figure 4.33, the temperature dependent electrical conductivity of ternary liquid crystal mixtures has been measured by using AC technique. The electrical conductivity of sample with 40% HAT6 concentration in ternary mixtures is found to be the highest, followed by 60% HAT6 and pure HAT6.

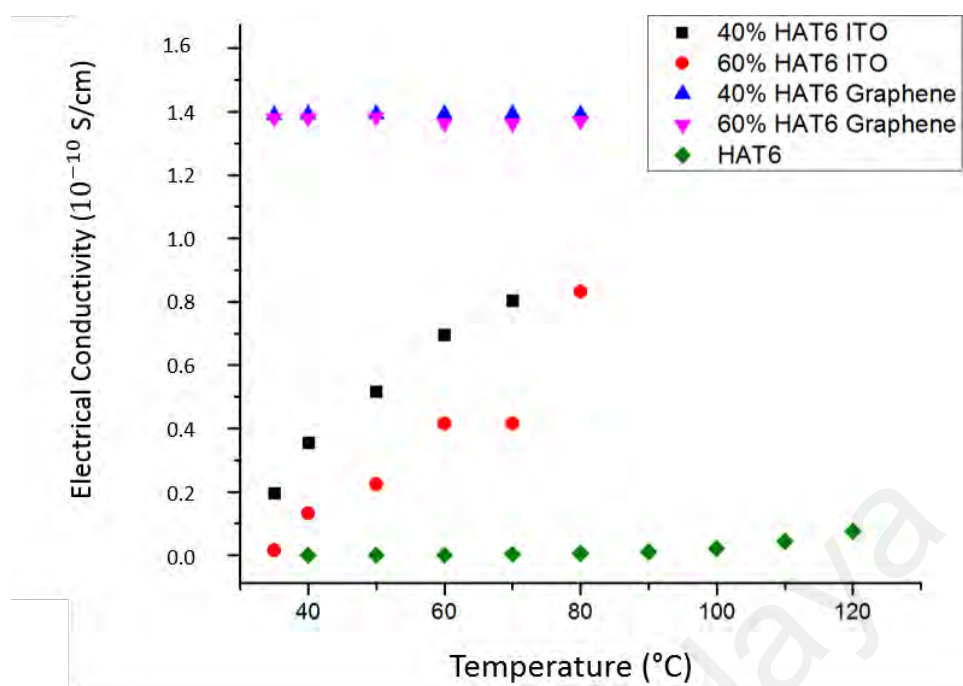


Figure 4.33: Temperature-dependent electrical conductivity of DLC, Smectic A, and Ferroelectric ternary LC mixtures.

Effect of electrodes used for cells fabrication has been investigated as well in Figure 4.34. It has been observed, the electrical conductivity of 40% and 60% ternary liquid crystal mixtures and AlCl_3 doped HAT6 has increased by at least two order of magnitude when sandwiched in graphene coated cells. In ITO coated cells, the electrical conductivity of AlCl_3 doped HAT6 has been found to be the highest, whilst the rest of mixtures was found to be about the same. When similar compounds were sandwiched in graphene coated cells, the electrical conductivity of AlCl_3 doped HAT6 was found to be the lowest, the mixture with highest percentage of HAT6 in the ternary mixtures was found to possess the highest electrical conductivity of the three. This might be probably caused by the mismatched in the graphene honeycombed lattice structure, brought by the disrupted AlCl_3 molecules. The result was unfavorable to the electrical conductivity of the AlCl_3 doped HAT6.

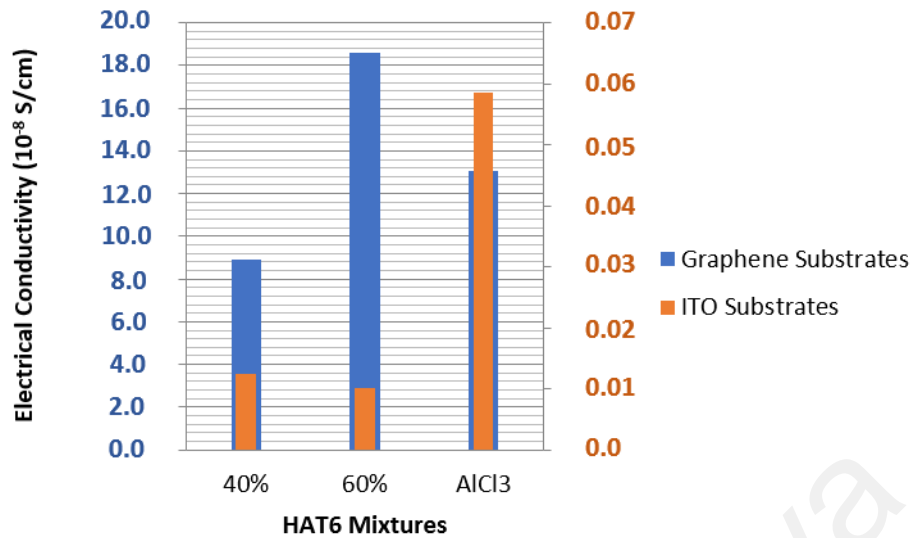


Figure 4.34: Electrical conductivity of different percentages of HAT6 mixtures and AlCl₃ doped HAT6 sandwiched in different substrates.

It is reasonable to believe that, the 60% HAT6 content in the ternary mixture produced more prominent interfacial interaction between honeycombs of the HAT6 and the graphene substrate, due to the least resistance in the lattice mismatch, hence increased its electrical conductivity by one order of magnitude. This result shows that the dependency of structural stability of HAT6 DLC mixtures with electrical conductivity. The control of macroscopic orientation is vital in DLC devices in order to enhance their electrical conductivity and electronic functions; the homeotropic alignment is preferred for this purpose. Homeotropic alignment will allow better mobility and charge transfer between parallel electrodes, where the carriers are moving in perpendicular direction. The chances for homeotropic alignment of DLCs on highly oriented surface such as MoS₂, pyrolytic graphite and graphene is higher due to higher interaction between plane surface of the DLC molecules which lying flat (surface affinity is involved) and the surface of electrodes. As has been described in various literatures, homeotropic alignment is obtained from slow cooling of DLC material from isotropic into columnar phase.

4.3.3.4 UV-VIS Experiment

The UV-Vis spectroscopy technique has been used to investigate the optical band gap of the ternary liquid crystal mixtures as shown in Figure 4.35. The optical band gap of materials can be determined from their absorption curves. The band gap which was calculated from the expression $E_G = \frac{hc}{\lambda}$ was shown in Figure 4.36. In this equation, E_G is the optical band gap, h is the Planck constant, c is the speed of light, and λ is the wavelength. The correlation shows that the optical band gap is highly dependent on the cut-off wavelength of the absorption curve. Tuning the breadth of the curve at the right side of cut-off wavelength is one way to achieve lower optical band gap, possibly improving electrical conductivity of DLC as well. This can be performed by addition of ionic dopants or compounds which are optically active. The room temperature band gap calculated shows very well agreement with electrical conductivity of the mixtures in ITO cells as shown in Figure 4.33. However, the result is not correlated well with samples in graphene cells in Figure 4.34.

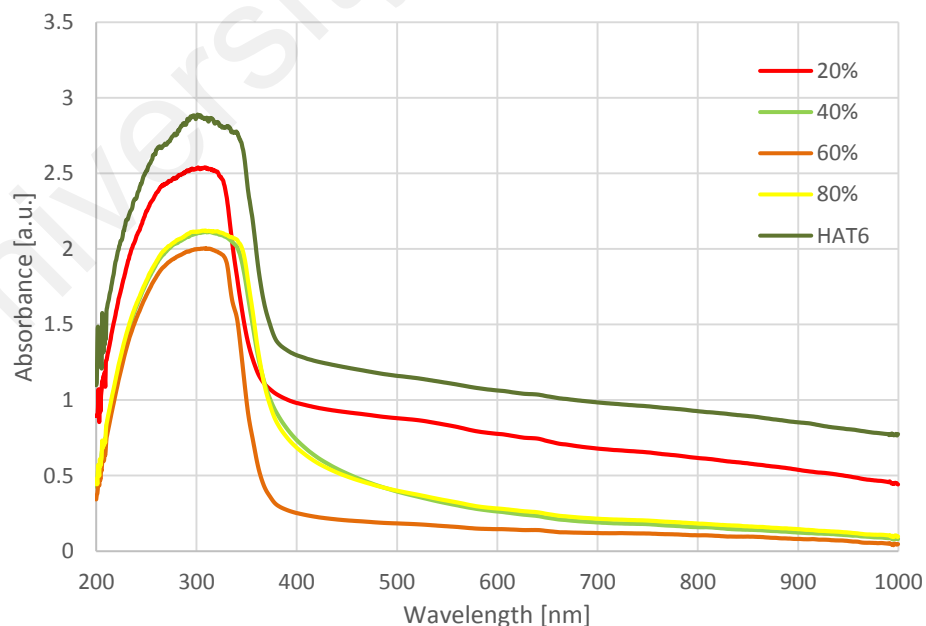


Figure 4.35: UV-Vis absorption results of HAT6 mixtures.

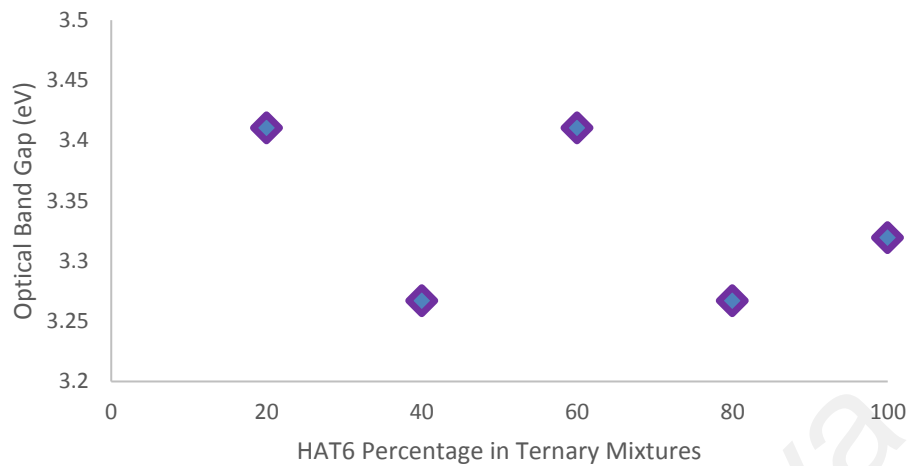


Figure 4.36: Calculated optical band gap of ternary liquid crystal mixtures at room temperature.

4.3.4 HAT6 Doped AlCl_3

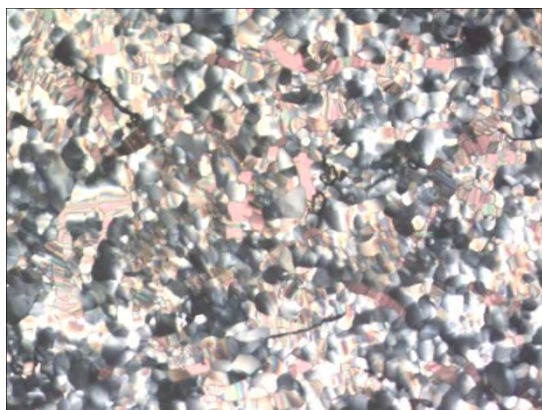
In this section, the effect of added ionic salts dopant to the HAT6 DLC is investigated. It is expected the ionic salts will facilitate the ability of HAT6 DLC to conduct electricity better. In order to improve conductivity of p-type doping, the AlCl_3 will act as electrons acceptor, receiving electrons from HAT6 molecules. The formation of charge transfer complex is expected. However, there is an optimum concentration of dopants amount that makes this enhancement possible. This is due to the structural stability of the columnar stacking that is also one of the main concern in this study. Alignment and columnar stacking are very sensitive and strongly affect the carrier mobility and electrical conductivity of HAT6 DLC. Besides, an improvement in optical band gap is also discussed. The electrochromic nature of charge transfer complex is said to be able to improve optical properties of host materials as they absorb light better.

4.3.4.1 Investigation on Mesomorphic Properties by POM

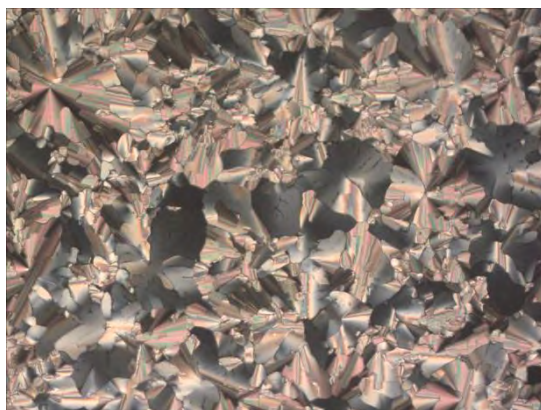
Figure 4.37 shows the POM images of the samples during columnar phase when the samples temperature are brought down to room temperature. The phase transition temperatures of each mixture are tabulated in Table 4.5. The formation of hexagonal columnar mesophase is expected in HAT6 DLC materials even after various concentrations of AlCl_3 dopant have been added. The existence of homeotropic mesophase is vital in many electronic applications exploiting charge transfer along column stacks of DLC discs, it shows a strong indication on the electronic behavior of DLC materials. Although the focal fan shaped characteristic of DLC has been observed in each image from Figure 4.37, their qualities are all different. The spilled of the columnar stacking due to excessive amount of AlCl_3 dopants has caused the focal fan shaped to appear differently, as can be seen in the larger mosaics textures in POM images of 7.5, 12.5 and 15 mol % of AlCl_3 . This was due to the disorder which has been caused by the bulk octahedral structure of AlCl_3 molecules.

Table 4.5: Transition Temperatures of AlCl_3 Doped HAT6 Mixtures

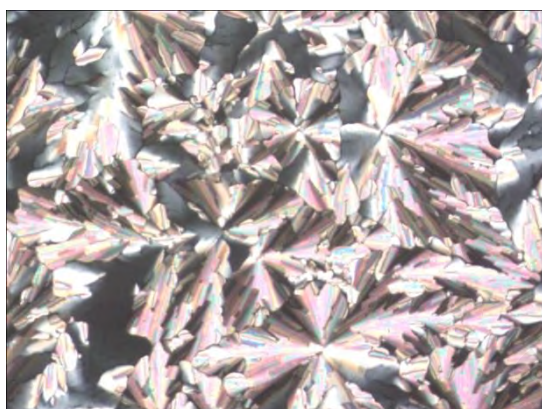
AlCl_3 (%)	Cooling Process		Heating Process	
	Iso-Col _h	Col _h -Cr	Cr-Col _h	Col _h -Iso
0	102.0	59.0	70.3	102.4
2.5	97.0	53.1	68.2	96
5	93.4	53.8	70.0	87.1
7.5	99.0	52.0	70.0	97.9
10	100.3	54.6	69.7	99.3
12.5	97.8	52.2	68.3	96.6
15	97.9	52.6	68.1	96.6



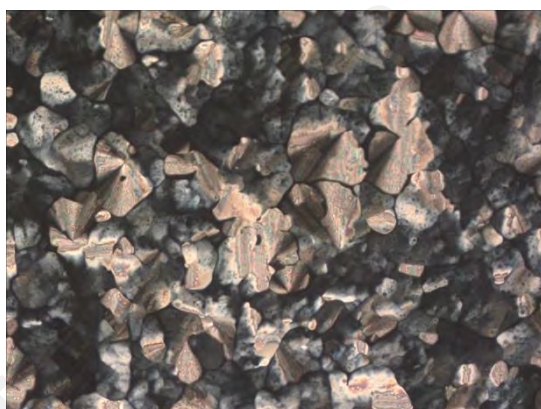
0% AlCl_3



2.5% AlCl_3



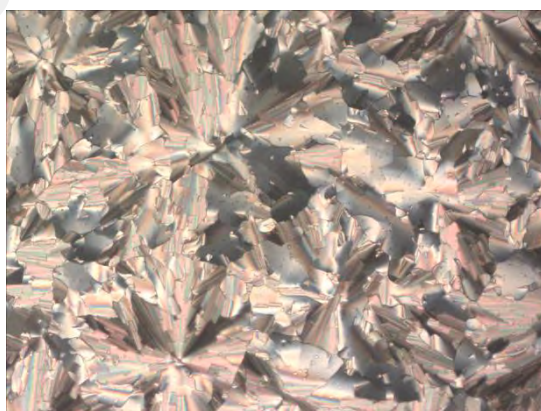
5.0% AlCl_3



7.5% AlCl_3



12.5% AlCl_3



15.0% AlCl_3

Figure 4.37: POM images during columnar phase for each mixture at different AlCl_3 concentrations.

4.3.4.2 Electrical Conductivity

AC and DC-electrical conductivities in HAT6 and AlCl₃ doped HAT6 have been investigated in Figure 4.38. In pure HAT6 compound, the DC electrical conductivity was found to be higher when compared to its AC electrical conductivity. Meanwhile, for the rest of compounds with AlCl₃ content, their AC electrical conductivity was found higher when in comparison with their DC electrical conductivities. The reason for this phenomena is due to the type of conduction possessed by these mixtures. The DC conductivity corresponds to the disorder hopping conductivity as has been observed in CP and OSC materials. Whilst AC conductivity has been observed in many CP-ionic and OSC-ionic mixtures. This was due to the different frequency of each component is vibrating at molecular level. The measurement which is sensitive enough to detect this slight vibrational frequency in individual CP/OSC-ionic mixtures is AC impedance spectroscopy technique.

Thus, from AC and DC electrical conductivity results, AC electrical conductivity was found dominating the compound with addition of ionic salt component into HAT6 DLC, whilst DC electrical conductivity dominates the conduction in pure HAT6 material. This agrees with Boden et al. studies which has described the most efficient conduction transport in ionic doped DLCs is through ionic conduction (Boden et al., 1993).

From figure 4.39, it was found the highest electrical conductivity was found in the mixture composed of 5 mol% AlCl₃. The plot which has been extracted from Figure 4.38 shows the electrical conductivity of the mixtures at 70 °C when the materials are in their columnar phase. The POM investigation concludes that the formation of columnar phase in 5 mol% is the most stable when compared with other mixtures, hence improving its electrical conductivity.

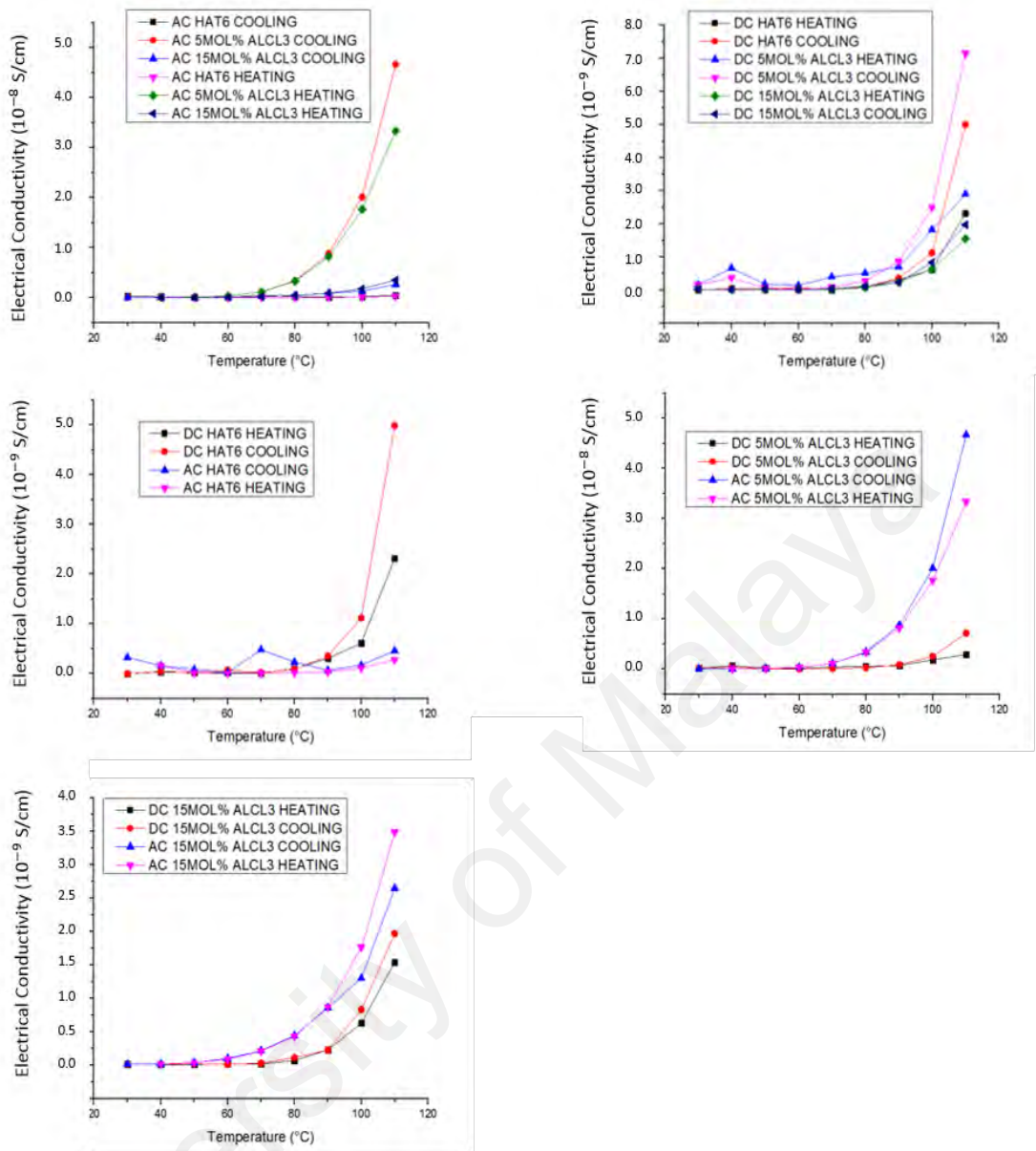


Figure 4.38: AC and DC-electrical conductivities of AlCl₃ doped HAT6 DLC.

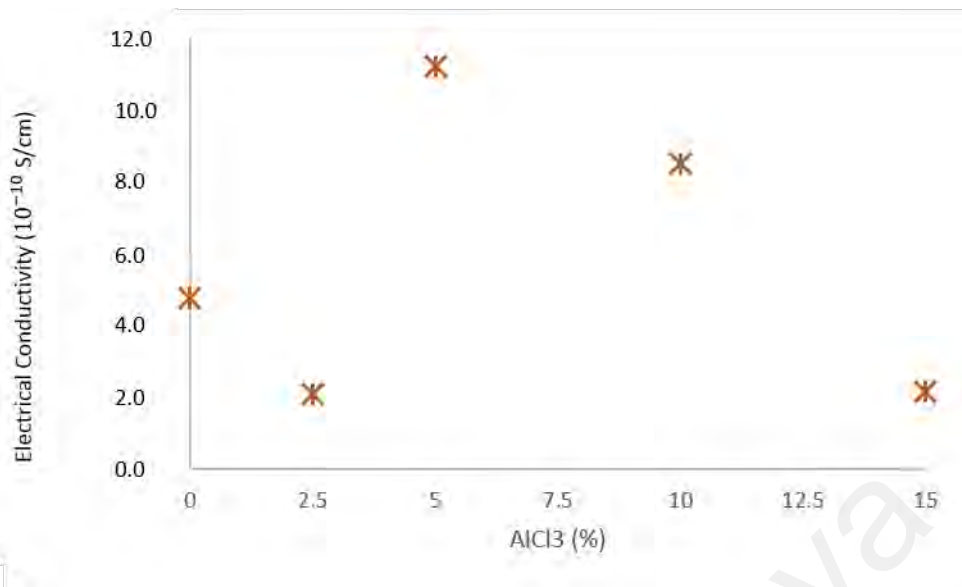


Figure 4.39: AC electrical conductivity of AlCl₃ doped HAT6 DLC in columnar phase at 70 °C

4.3.4.3 Mobility by Space Charge Limited Current (SCLC) Method

The extrinsic hole mobility in the doped HAT6 compound was investigated by using space charge limited current method (SCLC) as shown in Figure 4.40. The dielectric permittivities of the samples were determined from the capacitance data of the empty sandwiched ITO cells (before filling) and occupied sandwiched ITO cells (after filling). The I-V curves of the samples sandwiched in ITO cells were obtained at high magnitude of electric field. Next, the current density was plotted against the square of the electric field. Mott-Gurney equation is applied to fit the almost linear plot of current density against the square of the electric field as below

$$\text{Current density, } J = \frac{9}{8} \epsilon \mu_h \frac{V^2}{L^3} \quad (4.1)$$

where ϵ is the dielectric constant, μ_h is the holes mobilities, V is the applied voltage and L is the cell's thickness. The available hole carrier density is obtained from the following correlation

$$p = \frac{\sigma}{e\mu_h} \quad (4.2)$$

where $e = 1.6 \times 10^{-19} \text{C}$. The calculation resulted with hole concentration of $4.71 \times 10^{27} \text{ cm}^{-3}$, $4.05 \times 10^{27} \text{ cm}^{-3}$ and $1.99 \times 10^{27} \text{ cm}^{-3}$ for pure HAT6, 5 and 10 mol% AlCl_3 doped HAT6 respectively at 80°C . This indicates the extrinsic hole concentration is decreasing with addition of AlCl_3 dopants. However, this does not necessarily mean highest hole concentration is required in order to provide excellent conductivity. The optimum concentration is required in order to provide effective mobility. The bulk ionic salt molecules have been occupying empty spaces between columnar stacking, and will increase the scattering probability of uncontrolled hole carrier concentration. The highest or saturated hole carrier concentration will possibly allow larger carrier scattering magnitude and hence lowering the electrical conductivity.

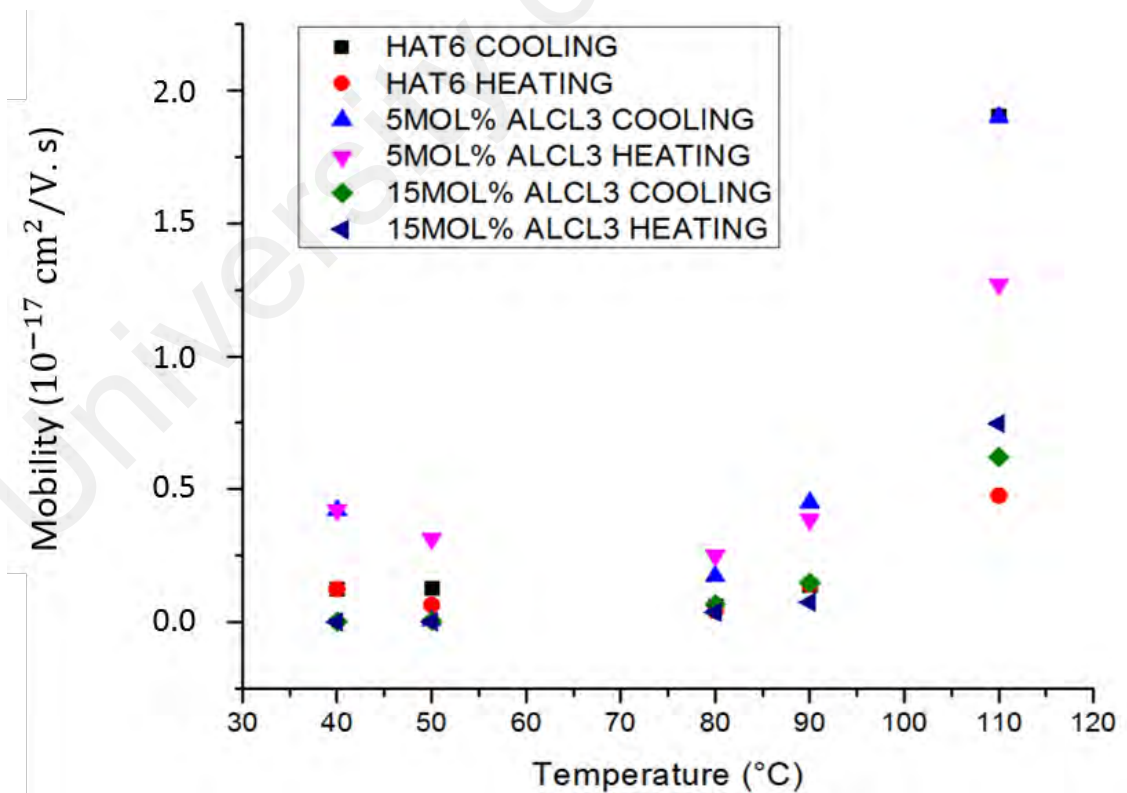


Figure 4.40: Mobility plot of HAT6 mixtures

4.3.4.4 UV-VIS Experiment

The UV-Vis spectroscopy technique has been used to investigate the optical properties of the AlCl_3 doped HAT6 as shown in Figure 4.41. The shoulder that slightly increased between 400 and 500nm in 5 mol% UV-Vis curve has been observed. The satellite peak that appears on the curve of 5 mol% AlCl_3 doped HAT6 has been identified to be the result of ionic interaction: efficient ionic transfer from sp^2 orbitals of HAT6 molecules to AlCl_3 ionic salt molecules, leading to the formation of charge transfer complex. An enhancement in electrical conductivity of the 5 mol% AlCl_3 doped HAT6 has been observed. The formation of the said charge transfer complex is evident by the appearance of the satellite peak, thus improving the electrical conductivity.

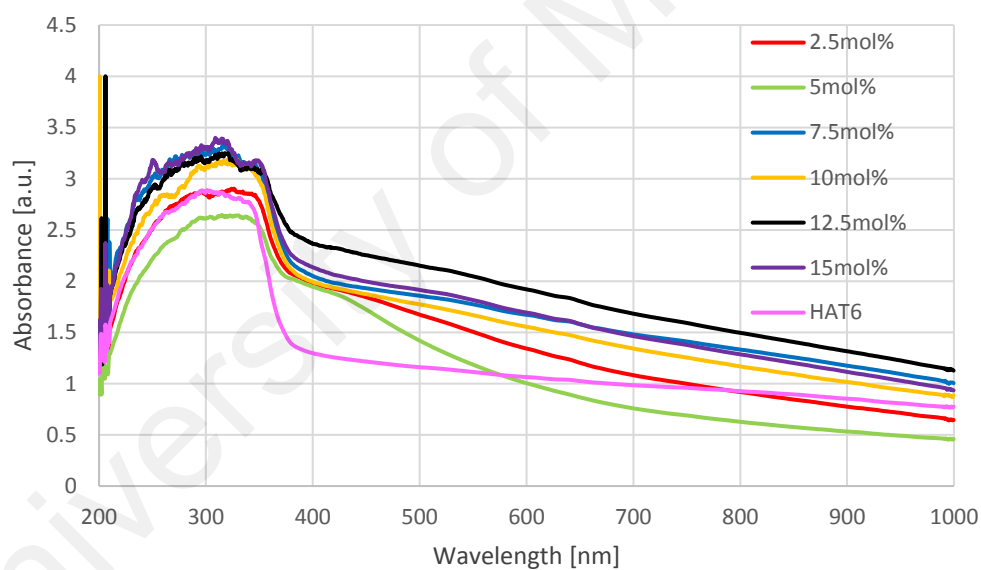


Figure 4.41: UV-Vis absorption results of HAT6 mixtures.

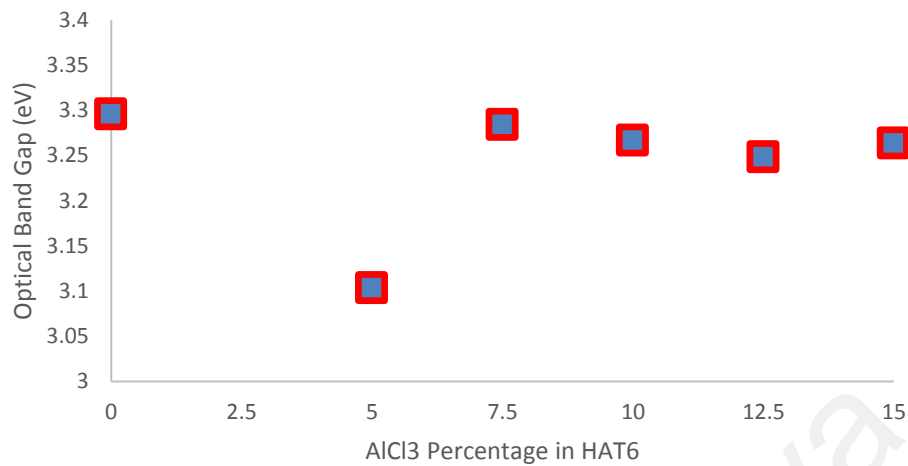


Figure 4.42: Calculated optical band gap of various percentage of AlCl₃ doping concentration in HAT6 at room temperature.

The band gap which was calculated from the expression $E_G = \frac{hc}{\lambda}$ was shown in Figure 4.42. The room temperature band gap correlated well with the measured electrical conductivity as shown in Figure 4.39. The 5 mol% AlCl₃ doping possessed the highest electrical conductivity, and the lowest optical band gap. The absorption spectrum shows that the optical band gap of DLC materials is tunable by addition of dopants at optimum concentrations. From the UV-Vis experiment, it can be concluded that the most efficient charge transfer during ionic conduction process occurred with the presence of 5 mol% AlCl₃ doping in HAT6 DLCs.

4.4 Studies on Structural Relation of Discotic Materials with Electrical, Electronic and Thermal Properties

In this section, further investigation on HAT6 DLC material was conducted by using Raman technique. This was performed by analysing the vibrational properties of HAT6 at elevated temperature during heating and cooling process. The correlation between wavenumbers shift could indicate the dependency of HAT6 electrical and electronic properties with their structural order. Furthermore, from Raman studies, thermal signature

from phonons interaction can also be determined. The idea or prediction of thermal behaviour of DLC at elevated temperature can also be determined by analysing the curves from Raman spectra.

4.4.1 Linewidth Analysis of Raman Spectra

Analysis on Raman profile frequently involves the correlation between changes in the area, the full width at half maximum (FWHM) linewidth and the peak shift of the curve with physical structure and chemistry of the molecules (Haverkate et al., 2014). The area of the peak consists of information such as the concentration of Raman active species with coherent vibrational motions such as in C-C and C-H bonds. The area of the final peak profile will depend on the multitude of similar interaction of all the individual vibrational interactions. Thus, high activity of molecular interactions will give rise to a Raman peak with sharp intensity and large curve area. On the other hand, the FWHM linewidth or broadening of the peak could provide an indicator such as the interaction of the bonds with the impurities present in the materials or disordered structure. Finally, the spectral peak shift will consist of information such as the difference in energy level of the materials before and after irradiation due to spontaneous polarizability, which will cause the radiation to scatter either to higher or lower energy levels. The irradiation by the Raman laser will induce electronic polarisation, which, in turn, will cause the bond to either attract or repel each atom at the either end of the bond. The strength of this attractive or repulsive force will determine the shift of Raman peak to either higher or lower in wavenumber and frequency (Bhattacharjee et al., 2001).

Laser lines of 488 and 514 nm were used in Raman spectroscopy experiments. The difference between these two light sources is their excitation energy. Shorter-wavelength light source has higher energy, and excitation of lone pairs of electrons is easier when compared to the longer-wavelength light source. In Raman spectroscopy technique, the

sensitivity of Raman measurement for shorter-wavelength light source is said to be increased due to wider range of interactions between bonds that is detectable by Raman detector and increased resonance enhancement as the light energy is closer to the excitation energy of the material or its band gap (Haverkate et al., 2014; Schrader, 2008).

The curve usually appears in the form of bell curve from a well-known statistical profile; a mixed of Gaussian and Lorentzian profiles (Bhattacharjee et al., 2001; Haverkate et al., 2014). The curve profiling process was assisted by using Origin software to deconvolute the curve by using suitable functions. A high proportion of symmetrical Gaussian profile was observed in 514 nm excitation wavelength Raman curve of C-C stretching at low temperature and eventually degraded at increased temperature. This indicates the presence of closely packed crystals arrangement in HAT6 at low temperature (Bhattacharjee et al., 2001). At high temperature, Lorentzian profile became more prominent instead as broader curve is observed when the rigidity of the packing loosened due to fluidity of the discotic liquid crystals.

Temperature-dependent Raman spectra for both 488 nm and 514 nm wavelengths are displayed in Figure 4.43 and Figure 4.44, in the range from the Cr phase at 30 °C to the Iso phase at 120 °C, preferentially from a cooling cycle in the first instance in order to attain better ordering of the columnar self-assembly (Bhattacharjee et al., 2001). There are three important segments that will be discussed in this paper: 1) The C-H interactions in the alkyl chains of HAT6 molecule in the range of 1350-1420 cm^{-1} . 2) The symmetrical stretching of C-C of aromatic rings in the range of 1420-1460 cm^{-1} . 3) The quinoidal stretching of C=C in the aromatic rings of HAT6 in the range of 1600-1650 cm^{-1} . From the observation, Raman spectra accumulated for 488 and 514 nm wavelengths in Figure 4.42 and Figure 4.44 are found almost identical except for the peaks in the region of

quinoidal stretching, where a satellite line appears in spectra excited by 488 nm laser.

This phenomenon is called the “photoselective resonance process” (Schrader, 2008).

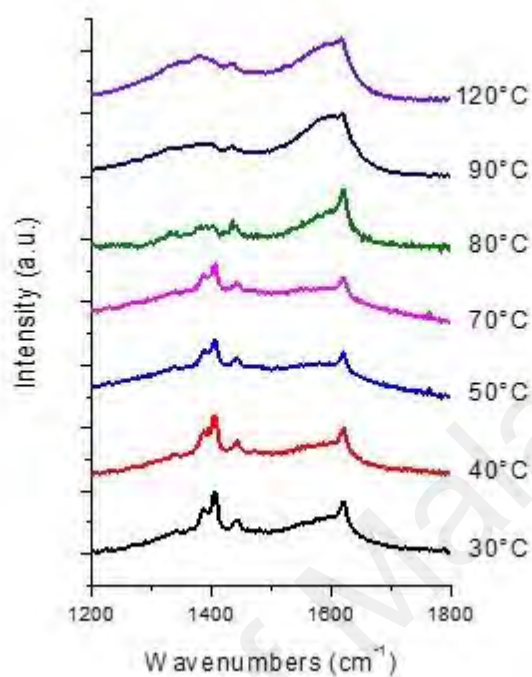


Figure 4.43: Temperature-dependent Raman spectra of HAT6 compound using 488 nm laser.

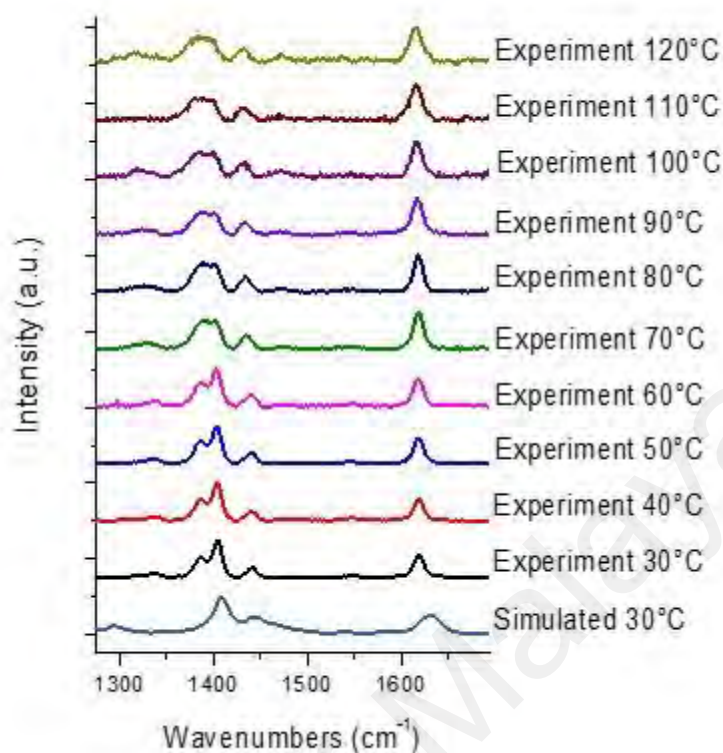


Figure 4.44: Temperature-dependent Raman spectra of HAT6 compound using 514 nm laser.

4.4.1.1 C-H vibrational modes towards aliphatic chains end (1350-1420 cm^{-1})

The Raman spectra in Figure 4.45 were obtained for both excitations at 488nm and 514nm. The dynamics of the alkyl chains of HAT6 was interpreted in terms of the backbones of the alkyl chains $-(\text{CH}_2)_5-$ which formed the aliphatic tails of the DLC molecules as shown in Figure 4.45 (c).

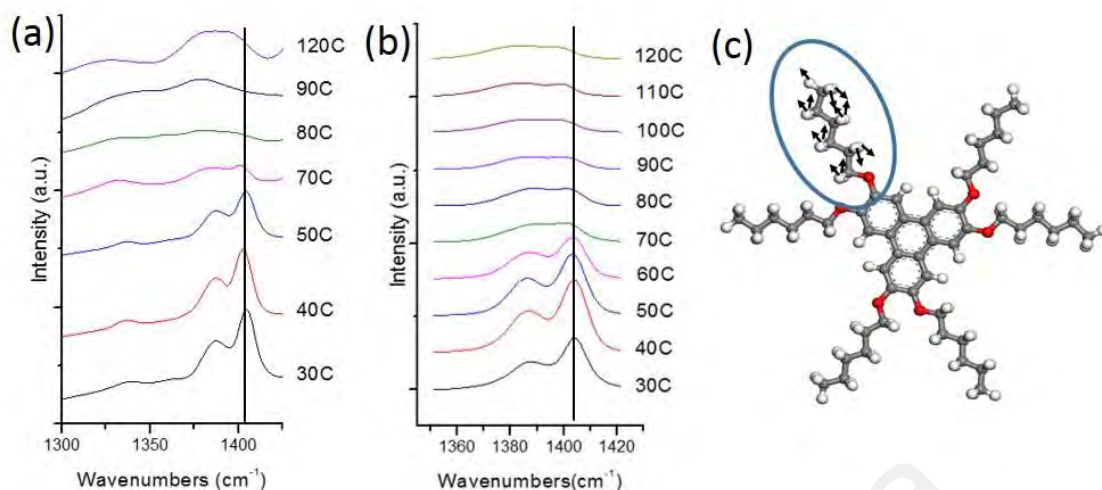


Figure 4.45: Raman spectra of C-H tails for (a) 488 nm and (b) 514 nm laser source. (c) The modes of vibrations of C-H atoms in the alkyl chains of HAT6.

Doublet splitting bands have been observed, the peaks are prominent at 1380 and 1420 cm^{-1} . Specifically, the band at 1380 cm^{-1} correlates to the wagging vibrations of $-\text{CH}_3$ group in the tails, whilst the 1420 cm^{-1} exhibits deformed bending vibrations of both CH_2 and CH_3 located in the tails. The doublet band appeared to be relatively intense at lower temperature as observed on a cooling scan of sample from approximately 70 $^\circ\text{C}$ to room temperature, but the intensity collapsed when the band coalesced together at higher temperature measurement. The sharp Raman profile for this range at lower temperature suggest a high degree of order of discotic molecules in Cr state (Bhattacharjee et al., 2001; Dash, Ranjan, Alapati, & Verma, 1997; Vikram et al., 2009). The profile broadened upon entering the D_h phase at 70 $^\circ\text{C}$. This is consistent with our expectation that the tails of the DLCs are disordered within the D_h phase whilst only the cores are strongly aligned in the D_h phase (Rey-Lafon & Hemida, 1990). Finally, upon transition from the D_h -Iso phase at 100 $^\circ\text{C}$, the bands of the dual peaks at 1380 and 1420 cm^{-1} have further collapsed. This is a result of disordered of the aliphatic chains. This was supported by M. Rey Lafon and A. Tazi Hemida who suggested that the methyl end $-\text{CH}_3$ interaction has weakened and fully disrupts the alignment of the molecules (Rey-Lafon & Hemida, 1990). The same characteristics have been observed for Schiff based liquid crystals in the range of 1160 to

1170 cm^{-1} , which typically are the bands representing the backbone of $-(\text{CH}_2)_n-$ chains of polymers (Bhattacharjee et al., 2001; Schrader, 2008). Furthermore, the transition from high temperature to low temperature i.e. from D_h to Cr phase also shows the shifting of the most intense peak from a lower wavenumber ($\sim 1403.2 \text{ cm}^{-1}$) to a higher wavenumber ($\sim 1404.5 \text{ cm}^{-1}$). This shift from low to high wavenumbers can be explained by its force constant. The force constant can be defined as the proportionality constant which correlates the amount of force which is necessary to move the atoms connected by a bond (Schrader, 2008). Thus the higher force constant in the Cr phase (higher wavenumber) suggests stronger bonding exists between HAT6 atoms in the alkyl tails as they become closer together in the crystalline phase (Bhattacharjee et al., 2001; Garreau, Louarn, Buisson, Froyer, & Lefrant, 1999). Thus, we can conclude that the Raman spectra of the aliphatic tails demonstrates random orientation upon heating the sample in D_h -Iso phase. Conversely, upon cooling, the packing becomes closer as the temperature is lowered.

4.4.1.2 Symmetrical stretching of aromatic cores in HAT6 (1420-1460 cm^{-1})

In this section, the symmetrical stretching of the aromatic cores is interpreted. Raman peaks for both excitations at 488 nm and 514 nm in the wavenumbers ranging from 1420 cm^{-1} to 1460 cm^{-1} are observed as shown in Figure 4.46. A peak shift centered around 1432 cm^{-1} at 120°C in the isotropic phase is shifted to 1440 cm^{-1} at 30°C in crystalline phase have been observed. Raman spectra of 488 nm wavelength excitation in Figure 4.46 (a) appears sharper than the Raman spectra of 514 nm wavelength excitation in Figure 4.46 (b). The incident energy from 488 nm (2.54 eV) light source is apparently more sensitive for DLC molecules as it is nearer to the electronic excitation of HAT6 materials (estimated at 2.85 eV) compared to 514 nm (2.41 eV) light source.

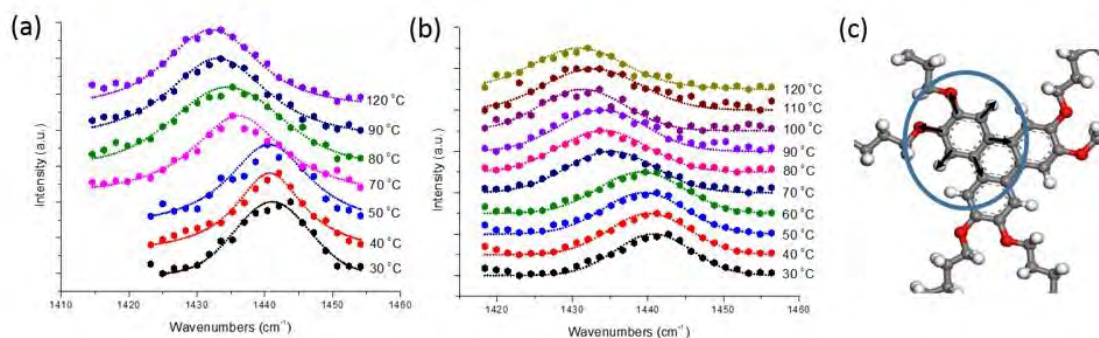


Figure 4.46: Raman spectra in the region between 1410 cm^{-1} to 1450 cm^{-1} for (a) 488 nm and (b) 514 nm laser lines (c) Symmetrical stretching mode of C-C atoms in aromatic rings.

The collective vibration mode of the HAT6 in the different phases are analysed as follows. Figure 4.47 shows the FWHM plot of symmetrical stretching mode of C-C against temperature. Thus, in a highly ordered Cr state, it can be seen that the FWHM is smaller, indicating a highly ordered of collective vibration of the aromatic cores as represented by symmetrical stretching of C-C. In the D_h phase from 70°C to 100°C , a broadening of the FWHM which is induced by the liquid-like flow in the D_h phase was observed. This in turn, results in a perturbation of the columnar stacks compared to the crystalline phase. Interestingly, upon entering the Iso phase at 100°C , we observe a FWHM trend which is similar to that in the columnar phase. The FWHM observed is stable in the Iso phase, implying a ‘memory’ of the columnar order carried over from D_h phase. this is in agreement to QENS study conducted by Mulder et. al, which implied that the order of the DLCs is carried into the Iso phase at the timescale of QENS which is in picosecond (Mulder et al., 2003). This observation of memory effect is expected to hold for the timescale of Raman spectroscopy which is on the femtosecond timescale, shorter than QENS. Additionally, the ordering of the aromatic cores and its collective motion is expected to affect the motion of the alkyl tails (Haverkate et al., 2014).

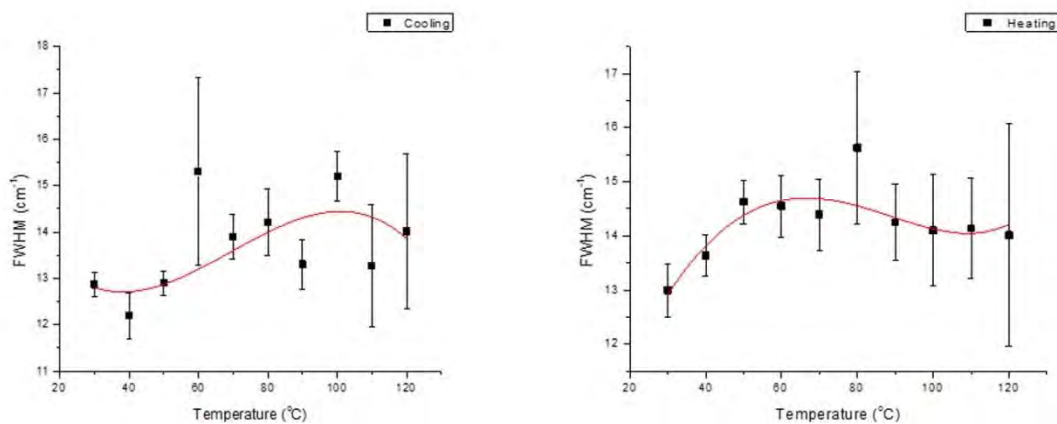


Figure 4.47: FWHM of symmetrical stretching mode of C-C atoms from 514 nm excitation Raman curves in the range of 1440-1460 cm^{-1} .

4.4.1.3 Symmetrical quinoidal vibrations of the aromatic cores of HAT6 (1600 to 1650 cm^{-1})

The Raman spectra centered around 1618 cm^{-1} are identified. This corresponds to the stretching of C=C bonds similar with the one identified in quinoidal mode of benzene ring as shown in Figure 4.48. Figure 4.49 and Figure 4.50 show the temperature dependent Raman spectra in the range of 1500 to 1750 cm^{-1} . Wide asymmetrical curves have been observed in 488 nm Raman spectra. A single and sharp distinct peak has been observed in recorded Raman spectra with 514 nm wavelength excitation. In Figure 4.51, slight broadening in linewidth and increase in area from Cr- D_h -Iso phase describes the increase in disorder within HAT6 materials as the temperature is increasing. This is due to the presence of the flow in the liquid crystalline phase, which results in perturbation of positional and orientational order in the D_h phase. The Cr phase with closed packing system has better positional order compared to D_h .



Figure 4.48: Quinoidal stretching of aromatic rings in HAT6 molecule.

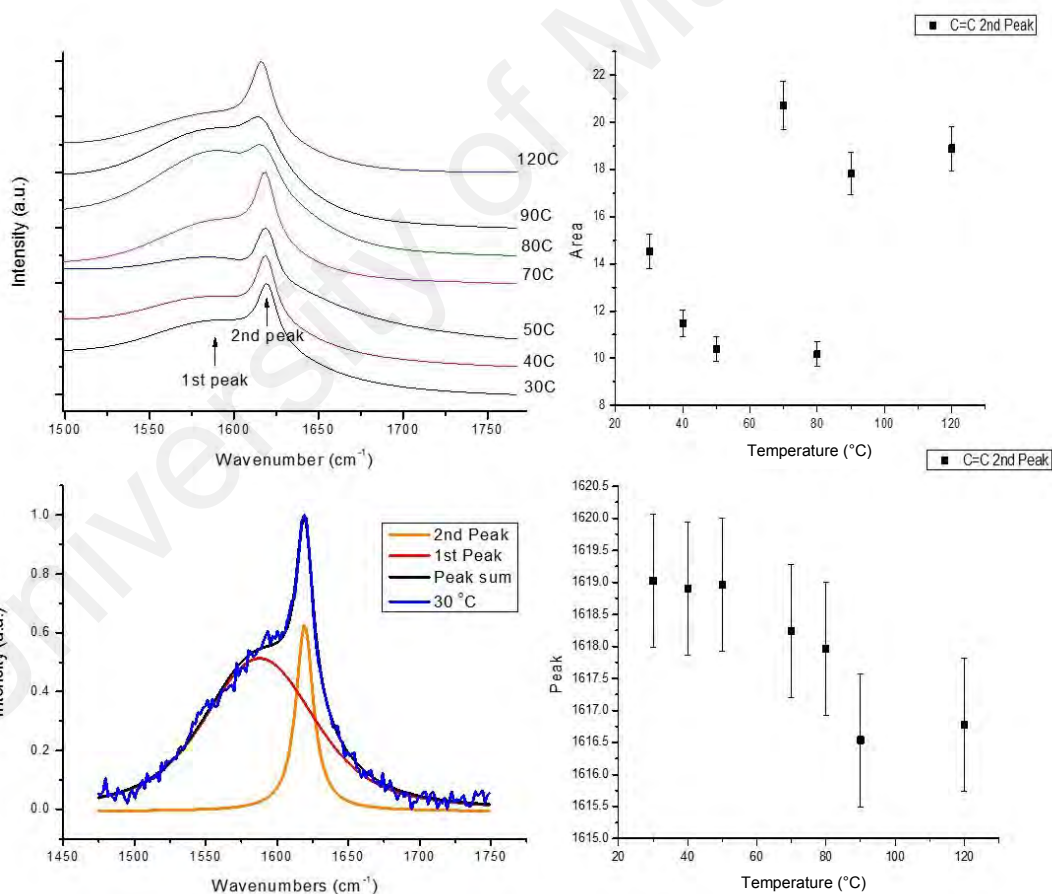


Figure 4.49: Fitted profile for C=C stretching using 488nm laser source (top left), area under the curve for each temperature profile (top right), deconvolution of C=C band of aromatic ring (top left), shifting evolution in the 2nd peak (bottom right).

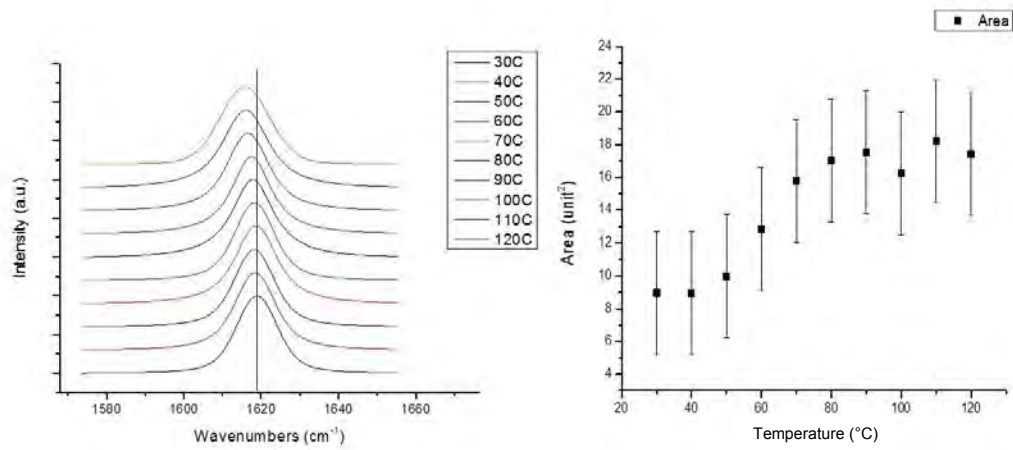


Figure 4.50: Raman spectra bands of C=C bonds of aromatic ring (left), area under the curve for each temperature profile (right) under 514nm light source.

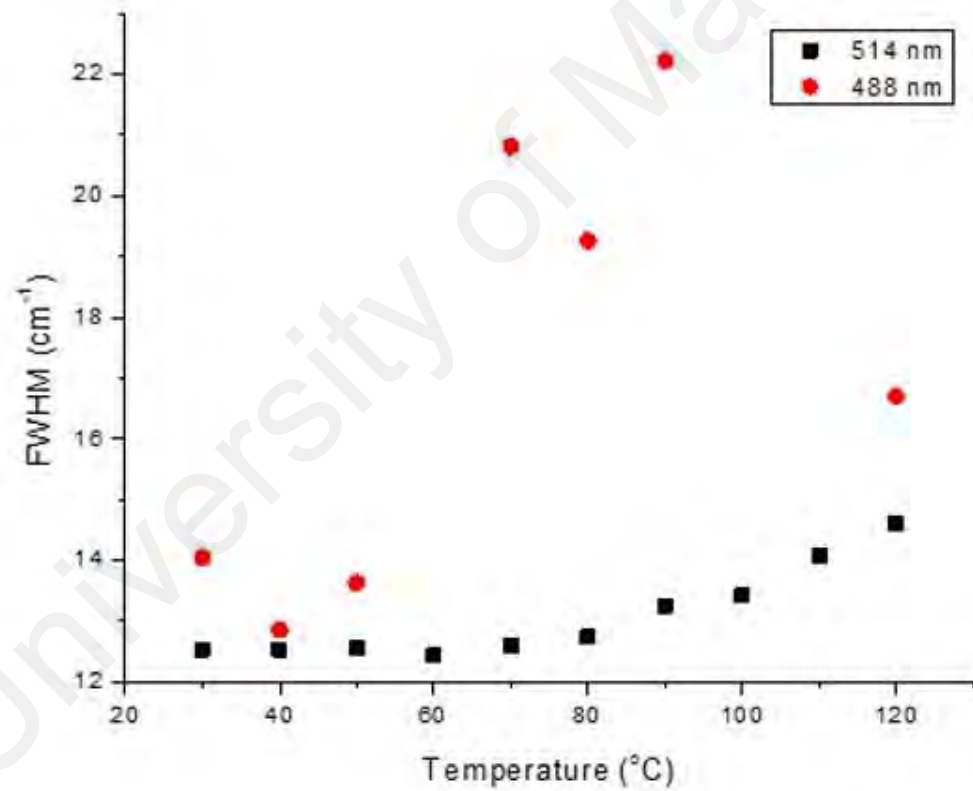


Figure 4.51: FWHM of C=C curves for both 488nm and 514nm excitations.

4.4.2 Energy Shift in Raman Spectroscopy

From Figure 4.49 and Figure 4.50, it is clearly observed that as the temperature is decreased, the peaks of C=C bands were shifted to higher wavenumbers for both excitations at 488nm and 514nm, a blue shift. The blue shifting is recognized by the shift of wavenumbers from a lower wavenumber at high temperature, to a higher wavenumber at lower temperature, as conceptually explained in Figure 4.52. Conversely, the reason for the red shifting in the opposite direction is explained accordingly.

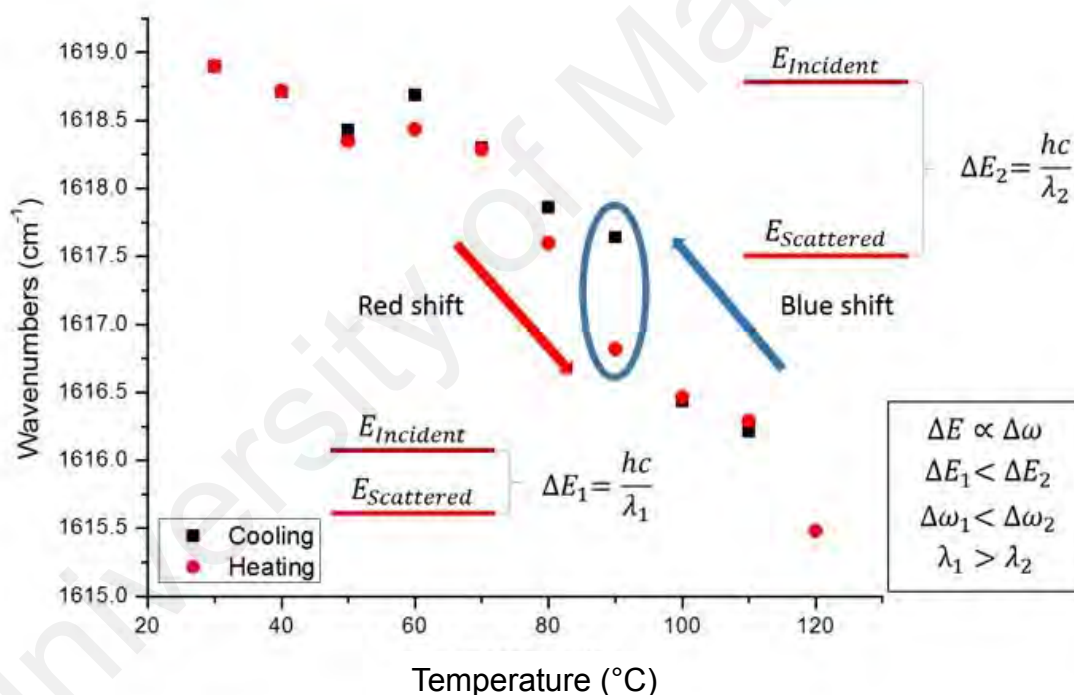


Figure 4.52: The correlation between peak position shifting with temperature for quinoidal stretching mode of C=C bond at 514nm laser source is plotted.

The relationship between ΔE and energy shift as defined by the; **red shift** is observed due to very small absorption (ΔE_1) because most molecules are initially vibrating at high virtual vibrational energy level. Thus, a relatively smaller energy is required to make the jump to excitation level, and shifted the wavenumber to a lower value. On the other hand, the **blue shift** occurs when the $E_{Scattered}$ is very small, indicating most of the $E_{Incident}$

is absorbed. Thus, the vibration energy of the bond needed to jump to the excitation energy is large (ΔE_2), and the wavenumber will be shifted to a higher value due to energy gain.

Relating to the plot of the wavenumber as a function of temperature for the Raman spectra as shown in Figure 4.52, we can see that the blue shift is observed upon cooling the HAT6 from Iso-Cr phase. Conversely, a red shift is observed upon heating from Cr-Iso phase. We can relate this observation to our understanding of order in the different phase. The red shift is observed going from Cr-Iso state; it is easier to go from an ordered to disordered state. Conversely, cooling from Iso-Cr state requires more energy going from the disordered to ordered state-hence blue shift is observed. The outcome of the blue shift upon cooling also implies the ordering and the bond strength are of better magnitude compared to when one heating the discotic materials. This is coherent with normal practice to use the first set of data for any discussion for liquid crystal materials starting with cooling cycle and followed by heating cycle to stabilise the D_h mesophase.

4.4.3 Relaxation time

Linewidth analysis of the mixed profile of Gaussian and Lorentzian curves in Raman spectra could also introduce another function called relaxation time. The relaxation time is interpreted as the time taken for the vibrating molecule to return to its ground state. The vibrational relaxation time of the molecules is calculated based on its directly proportional relationship with FWHM of the Raman band as shown in equation $\tau_{rel} = \hbar/FWHM$, $\hbar = 5.3 \times 10^{-12} \text{ cm}^{-1} \text{ s}$ (Haverkate et al., 2014). In this study we calculated the phonon relaxation time derived from the C=C response of the Raman spectra for 488 and 514 nm lasers as shown in Figure 4.53.

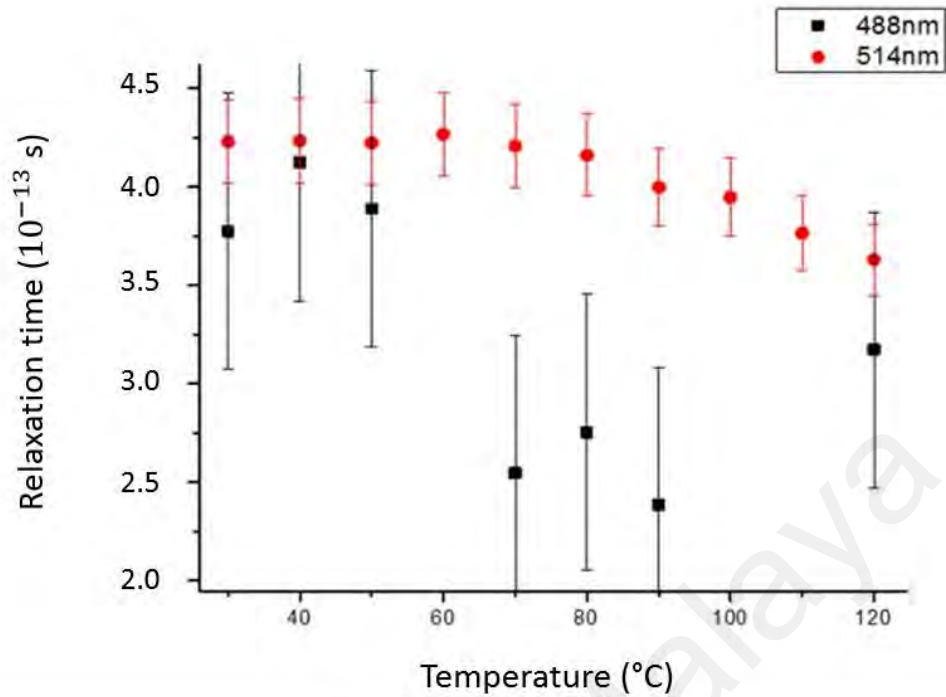


Figure 4.53: Calculated temperature-dependent relaxation time.

The range of relaxation time for DLCs is estimated at 395 fs to 423 fs in Iso and Cr phase respectively which is an order magnitude faster than that of the wurtzite inorganic semiconductor, a nitride based material studied by Leah Bergman et al (Bergman et al., 1998). This means that the vibration is decaying faster in isotropic phase compared to crystalline phase which agrees with the fundamental of heat transfer mechanism.

The phonon relaxation time can be interpreted in term of its relationship with thermal conductivity. In liquid crystals, the relaxation time is reduced as the phonon transport is scattered by crystal anharmonicity. Faster relaxation time should correspond to a reduction in thermal conductivity. Thus, this relaxation time in DLCs indicates that it is a better thermal insulator than most of inorganic semiconductor materials.

This reduction of thermal conductivity is useful in application which requires low thermal conductivity. One such application is thermoelectrics, where high thermoelectric performance requires good electrical conductivity and low thermal conductivity.

4.5 DFT Simulation

In this section, the structural order that was learned from the previous section on Raman studies is confirmed with quantitative charge transport analysis. The band gap of HAT6 was calculated by using DFT technique to provide further understanding between structure and electronic properties. The molecular packing in DLC materials is studied at elevated temperature using two different models, (1) periodic, (2) amorphous, and further correlated with their respective band gap. The HOMO-LUMO studies on DLCs could provide a pathway for rational molecular design for enhanced electronic properties in DLCs. It is critical to find suitable strategy for improvement in electronic properties of DLCs so that they can be used in STEG application.

4.5.1 HOMO-LUMO Energies Calculations

4.5.1.1 Band Gap of HAT6

HOMO and LUMO energy was calculated and the results are tabulated in Table 4.6. The band gap, E_g was estimated from HOMO-LUMO energy difference. The electronic HOMO-LUMO energies of the following system were calculated; single molecule system, two molecules within unspecified boundary model, and a periodically stacked (1D) crystalline model as shown in Figure 4.54.

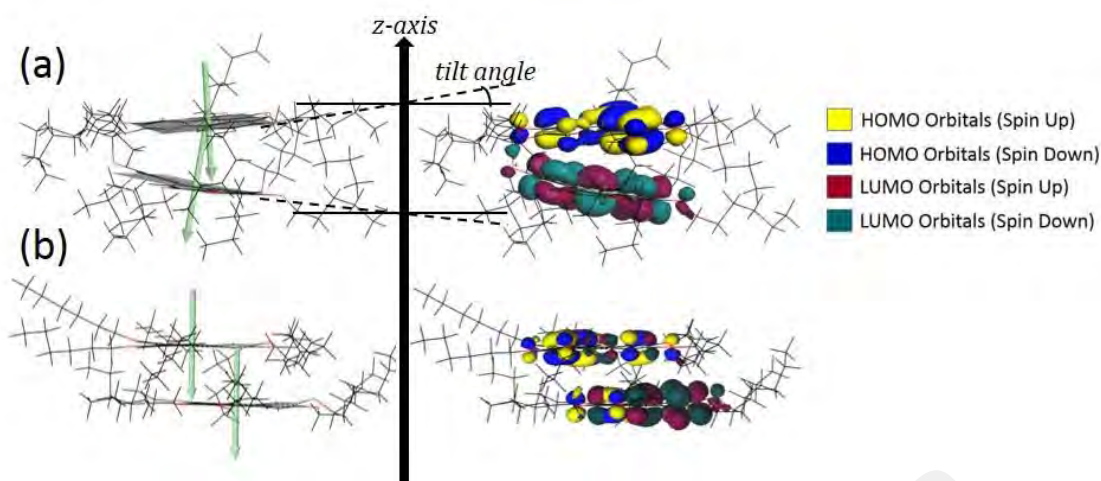


Figure 4.54: In-plane geometrically optimized view of HAT6 molecules in (a) unspecified boundary model, and (b) periodic crystal model at 80°C. Location of HOMO and LUMO orbitals is shown respectively on the right.

Comparison of the single molecule, molecules with unspecified boundary system and 2 molecules periodic crystal system is as follows: (i) It was noted that the lowest calculated band gap was indeed during LC columnar phase in all three configurations. Similar studies with thiophene repeat units showed that simulated matrix with increasing number of molecule narrows the band gap of the materials due to increasing chance of the overlapping in conduction orbitals (Kroon et al., 2016). In this work, it has been identified that some other factors such as movability space around the molecule also able to influence the band gap calculation. (ii) Generally the core to core distance of the molecules within unspecified boundary model is larger than the periodic crystal model (iii) the band gap in the LC columnar phase for the unspecified boundary model is smaller than the band gap for the periodic crystal model, despite the fact that the spacing for the periodic crystal model is smaller (iv) in order to explain this, we then take a closer look at the local geometry of the DLC molecule, particularly the in plane tilt geometry of the cores. In the LC phase, it can be seen that the tilt distribution of the unspecified boundary model is larger (16.916 and 4.011 degrees) compared to the periodic crystal phase, which are almost co-planar and possessed a small tilt angle (3.482 and 1.042 degrees). This ties in with the expectation that the unspecified boundary model has more flexibility and

allows closer geometrical contact in localised region of the molecule, due to the relatively extreme angle of tilt. Further studies on the effect of distance and twist of DLC molecules on the band gap can be found in a related work by S. Mohd Said et al (Said et al., 2016).

Table 4.6: Summary of DFT calculations.

	Temperature (°C)	Phase	HOMO (eV)	LUMO (eV)	Band Gap (eV)	Twist Angle	Tilt Angle	Core Distance (Å)
Single Molecule	27	Cr	-4.449	- 1.349	3.100	-	-	-
	80	D_h	-4.510	- 1.453	3.057	-	-	-
	130	Iso	-4.508	- 1.394	3.114	-	-	-
Unspecified boundary model	27	Cr	-4.177	- 1.197	2.980	30.440	11.973 13.142	4.163
	80	D_h	-4.193	- 1.429	2.764	39.716	16.916 4.011	4.026
(2 stacking molecules)	130	Iso	-4.194	- 1.237	2.957	63.132	5.652 0.536	4.103
Periodic crystal model	27	Cr	-4.087	- 1.223	2.864	-	9.125 2.733	3.388
	80	D_h	-4.056	- 1.211	2.845	-	3.482 1.042	3.553
	130	Iso	-4.067	- 1.158	2.909	-	2.151 0.171	3.808

4.5.1.2 Relative Energy Levels of HAT6 and AlCl₃

The HOMO and LUMO energy levels of individual HAT6 compound and AlCl₃ compounds has been estimated from DFT calculations as shown in Figure 4.55. The strategy which can potentially improve electrical conductivity and optical properties of HAT6 DLC is discovered through the selection of the right doping materials to match with relative energy of host materials i.e. between valence band of electron donor, HAT6 and conduction band of electrons acceptor, AlCl₃. This leads to the transfer of electron from host material to the doping material. The LUMO energy level of the dopant needs to be sufficiently lower than the HOMO energy level of the host material. The width energy gap between HOMO level of HAT6 and LUMO energy level of AlCl₃ controls

the coulombic interaction in the host materials. With sufficiently large gap width, the holes in host material is free to move among the host molecules, instead of recombining with the electrons from the acceptor dopant at LUMO level.

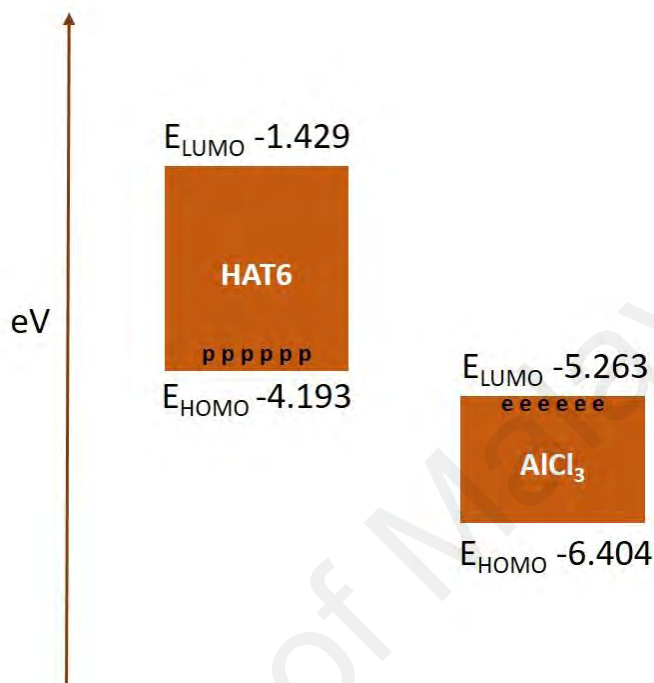


Figure 4.55: Relative energy levels of HAT6 as host material and AlCl₃ dopant in vacuum.

The calculated HOMO energy level of HAT6 at its valence band was -4.193eV, whilst LUMO energy level at conduction band of AlCl₃ was -5.263eV. The slight mismatch of energy levels is an indication that the splitting of the orbitals which govern the coulombic interaction was not very efficient, although minute conductivity enhancement was still observed.

4.5.2 DFT Calculated Raman Spectra

DFT calculation of Raman spectroscopy for 514 nm was performed and the results show satisfactory agreement when comparing the Raman spectra of experimental and simulated works as shown in Figure 4.56 and summarized in Table 4.7.

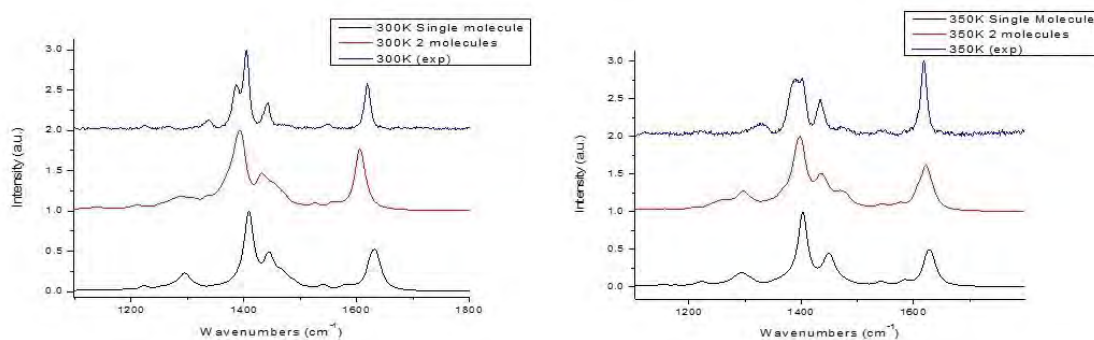


Figure 4.56: Simulated temperature-dependent Raman spectra of HAT6 molecule at 27°C (left) and 80°C (right).

Table 4.7: Summary of the simulated vibration modes.

Molecule		Modes	C-H Tails (1 st Peak)	C-H Tails (2 nd Peak)	Symmetrical CC stretching	Quinoidal CC stretching
		27°C	Experiment		1386.35	1404.67
Simulation	Single Molecule		-	1391.74	1431.81	1605.66
	Periodic Crystal Packing		-	1409.01	1445.12	1631.65
80°C	Experiment		-	-	1433.60	1618.47
	Simulation	Single Molecule	-	1396.64	1434.68	1622.90
		Periodic Crystal Packing	-	1402.71	1448.81	1628.16

Prior to DFT calculations, the molecule temperature was stabilized based on MD simulations as described earlier in the methodology section. The results show that the centered peak positions were mostly overestimated especially in C=C quinoidal stretching region. The doublet splitting of the C-H atoms vibrations in the alkyl chains disappeared in the DFT calculation.

The applied linear combination of atomic orbitals, LCAO method in MD calculation is served as an approximation when compared with DFT calculation such as Density

Functional Perturbation Theory (DFPT). For complex systems i.e. liquid crystals, LCAO is unable to describe their electronic configurations and minimal basis set properly. Weaker bonding is neglected and only single geometry configuration is considered. This is inadequate, in liquid crystals system where the resonance energy resulting from the stacking of the molecules is important in order to reflect many of the measured properties, for example charge transfer response and molecular spectroscopy analysis.

The difference between the experimental and simulated Raman spectra lies in the fact that no appreciable trend for the spectral shift as a function of temperature was observed. This can be traced to the LCAO method we used in the MD simulations. The DFPT method may be explored in the future for a more accurate representation of the LCs system. It is, however, computationally more expensive.

CHAPTER 5: CONCLUSION AND RECOMMENDATION

The following conclusions have been summarised from the respective study in the discussion chapter which was based on the objectives that have been stated earlier.

5.1 To define the specifications for an “solar funnel” based device architecture using finite element analysis modelling

The first initiative to simulate a unique solar heat funneled thermoelectric device has been completed by using ANSYS modeling software. The conducting polymer was incorporated in the simulated model. In the studies, each important aspect such as the effect of heat losses through convection and radiation, the optical properties and the length of the thermoelectric leg has been covered. All these aspects were correlated with their abilities to retain heat in the thermoelectric structure. It was found that the model which was exposed to highest diffused radiation was able to retain the highest temperature between the hot side and the cold side of STEG. This is due to the proportional relationship between heat absorbed and the radiation intensity. Looking into the emissivity of the electrodes of STEG, the highest heat retainment ability has been demonstrated by the model with lowest emissivity. Higher absorptivity in active materials has been found to be secondary as the transmissivity property was the primary effect which leads to higher heat storage capability in STEG device. Design of STEG with longer legs and lower thermal conductivity will also improve the heat retainment due to the slowing down of the heat conduction rate escaping the STEG device. These parameters are important in order to design a thermal bank that can keep high temperature difference across the thermoelectric legs.

Further optimization of the power output for this STEG, which currently stands at 5.5 $\mu\text{W}/\text{cm}^2$ is warranted, for it to be viable in applications such as STEG and other ambient

temperature energy harvesting applications (in comparison with studies from Table 2.2). This simulation illustrates the current limitations in utilizing polymer based TEGs, due to its relatively low Seebeck coefficient and electrical conductivity. However, the advantages of using organic materials thermoelectrics, such as cost effectiveness, solution processability and ease of fabrication, has provided continuous motivation for further work in materials exploration and device design for future development.

5.2 To investigate the electrical properties and Seebeck coefficient of PELC systems

A polymer material was investigated for potential application in STEG. Novel polymer, PVA-based PELC mixtures were prepared to investigate the effect of 5CB liquid crystal on the thermoelectric properties. The 5CB exhibited nematic-isotropic transition in the PELC mixtures and their concentration corresponded to the thermoelectric properties of the PELC. The PELC mixtures obey the hopping transport model except in the near nematic transition temperature. The transient decrease around the transition temperature was caused by the reduction of carrier mobility associated with the nematic-isotropic phase transition of 5CB. The absolute value of Seebeck coefficient decreased as the temperature increased and became constant above the transition temperature, originated from the order-disorder transition. From the studies, it has been found that the 5-15% 5CB doped PELC mixtures showed lower ZT value at the highest temperature. The 25% 5CB doped PELC mixture showed the highest ZT of 8.2×10^{-8} , which was six times higher than 5CB-free mixture. The use of liquid crystal in the polymer-based thermoelectric is promising to enhance the ZT value.

5.3 To characterise the electrical and optical properties of DLCs

Discotic liquid crystals have been studied in order to understand the mechanism of enhancement in their electrical and electronic properties for potential use in STEG. It was

found that the HAT10 DLC materials possess moderate thermoelectric properties with Seebeck coefficient in the range of 30 to 60 $\mu\text{V/K}$. The electrical conductivity of DLCs has been shown to correspond well with the temperatures. In the first study, the surface/sheet electrical conductivity of planar discotic liquid crystals HAT10 was measured. Upon heating, the electrical conductivity of $\sim 540 \text{ S/cm}$ and mobility of $\sim 98.1 \text{ cm}^2/\text{V-s}$ were found across the gold electrodes contact on top of HAT10-ITO substrate layer. In the following studies, in which the DLCs were observed to behave in a manner that nanowire conductors would, in homeotropic device, the magnitude of the intrinsic conductivity of HAT6 was found to be in the order of 10^{-12} . The significant increase was phenomenally observed in discotic liquid crystals columnar phase.

It was also found that the realignment of columnar phase during cooling process has improved the ordering of the molecules as reflected in the observed electrical conductivity measurement. The magnitude of electrical conductivity has been found to be greater during cooling process. UV-Vis experiment has also been conducted and the calculated band gap has shown positive correlation with the electrical conductivity. The formation of charge transfer complex in HAT6- AlCl_3 compounds has been verified by using UV-Vis experiment. Due to efficient ionic transport in AHT6- AlCl_3 compounds, their electrical conductivity especially during columnar phase has been found to be enhanced by at least 5 orders. The calculated band gap in HAT6- AlCl_3 compound also has been found to be the lowest. Further exploration on this work, such as the use of larger and metallic incorporated DLCs could probably show discotic liquid crystals materials as commercially viable thermoelectric devices for STEG application.

5.4 To understand the electronic charge transport in self-assembled HAT6 discotic liquid crystals through structural and molecular vibration studies

The discussion centred on the columnar order in DLCs was exposed in Raman studies. The behaviour of HAT6 DLC which can be described as a quasi 1D charge conductor was scrutinised in Raman studies. In the studies, Raman spectroscopy was the main tool of analysis, to quantify the positional correlation between stacks of the cores and alkyl chains of the molecules. The Raman spectroscopy results indicated that the alkyl chains were disordered throughout the D_h and Iso phases. Core-core stacking was highly correlated in the D_h phase during transition. ‘Memory’ of columnar stacking extends into the Iso phase at femtosecond timescale has been observed. Collective motion of core is expected to impact its alkyl chain motion. The blue shift of Raman peak indicates stabilization of core to core ordering in cooling.

Given the indication of order from Raman spectroscopy, we correlated the 1-D charge conduction ability of the columnar stacks in the liquid crystalline phase with its electrical conductivity. We also calculated the phonon relaxation time for the DLC phase, which indicated that it is a good thermal insulator.

5.5 To investigate the structural-electronic correlation of DLCs using molecular modelling

The final discussion topic opens up on possibility of engineering the organic molecules at molecular level. The structural conformation of the HAT6 molecule was also used to calculate its band gap using Density Functional Theory (DFT). Thus, we have tried to build a picture relating columnar order with electrical conductivity, using Raman scattering technique. We have shown that in the hexagonal columnar liquid crystalline (D_h) phase, an enhancement of electrical conductivity is coupled with reduction in thermal conductivity. Such properties may be valuable for use as a thermoelectric material, where

a high electrical conductivity and low thermal conductivity is desirable for good performance.

An interesting outcome of the DFT simulations of the band gap for the HAT6 molecules indicates that when comparing an amorphous model versus a periodic crystal model for the HAT6 stacking, a smaller band gap was achieved in the LC phase for the amorphous model which lowered the energy barrier through local geometrical proximity. This may be a useful strategy to help decrease band gap in DLCs in future DLC molecules design.

5.6 Recommendations for future works

From this work, properties of discotic liquid crystals have been explored and fascinating findings have been discovered. However, there are plenty of rooms that there can be improved.

- To conduct experimental studies on STEG by fabricating STEG device using low cost printing techniques.
- To explore different strategies of doping and mixture combination of DLC such as CPI, and also explore larger aromatic core DLC materials, in experimental studies and simulation work.
- To fabricate polymer-liquid crystals-electrolyte (gel) as a potential active material for STEG.
- To conduct non-contact (optical) technique for thermal conductivity measurement using spectroscopic equipment for DLCs in cells.
- To correlate properties from the measurement to develop a fundamental model or correlation, i.e. regression model between electrical conductivities and temperatures.

REFERENCES

- Alam, H., & Ramakrishna, S. (2013). A review on the enhancement of figure of merit from bulk to nano-thermoelectric materials. *Nano Energy*, 2(2), 190-212.
- Baheti, K., Malen, J. A., Doak, P., Reddy, P., Jang, S.-Y., Tilley, T. D., . . . Segalman, R. A. (2008). Probing the Chemistry of Molecular Heterojunctions Using Thermoelectricity. *Nano letters*, 8(2), 715-719.
- Balagurusamy, V., Prasad, S. K., Chandrasekhar, S., Kumar, S., Manickam, M., & Yelamaggad, C. (1999). Quasi-one dimensional electrical conductivity and thermoelectric power studies on a discotic liquid crystal. *Pramana*, 53(1), 3-11.
- Balandin, A. A., Ghosh, S., Bao, W., Calizo, I., Teweldebrhan, D., Miao, F., & Lau, C. N. (2008). Superior thermal conductivity of single-layer graphene. *Nano letters*, 8(3), 902-907.
- Bergman, L., Alexson, D., Nemanich, R. J., Dutta, M., Stroscio, M. A., Balkas, C., & Davis, R. F. (1998). *Phonon Dynamics and Lifetimes of AlN and GaN Crystallites*. Paper presented at the MRS Proceedings.
- Bhattacharjee, A., Alapati, P., & Verma, A. (2001). Dynamics of phase transitions in a liquid crystal probed by Raman spectroscopy. *Liquid Crystals*, 28(9), 1315-1320.
- Biswas, K., He, J., Blum, I. D., Wu, C.-I., Hogan, T. P., Seidman, D. N., . . . Kanatzidis, M. G. (2012). High-performance bulk thermoelectrics with all-scale hierarchical architectures. *Nature*, 489(7416).
- Boden, N., Bushby, R., & Clements, J. (1993). Mechanism of quasi-one-dimensional electronic conductivity in discotic liquid crystals. *The Journal of chemical physics*, 98(7), 5920-5931.
- Boden, N., Bushby, R., & Clements, J. (1994). Electron transport along molecular stacks in discotic liquid crystals. *Journal of Materials Science: Materials in Electronics*, 5(2), 83-88.
- Boden, N., Bushby, R., Clements, J., Movaghar, B., Donovan, K., & Kreouzis, T. (1995). Mechanism of charge transport in discotic liquid crystals. *Physical Review B*, 52(18), 13274.
- Boden, N., Bushby, R. J., Cammidge, A. N., Clements, J., Luo, R., & Donovan, K. J. (1995). Transient photoconductivity and dark conductivity in discotic liquid crystals. *Molecular Crystals and Liquid Crystals*, 261(1), 251-257.
- Borup, K. A., De Boer, J., Wang, H., Drymiotis, F., Gascoin, F., Shi, X., . . . Iversen, B. B. (2015). Measuring thermoelectric transport properties of materials. *Energy & Environmental Science*, 8(2), 423-435.
- Bubnova, O., Khan, Z. U., Malti, A., Braun, S., Fahlman, M., Berggren, M., & Crispin, X. (2011). Optimization of the thermoelectric figure of merit in the conducting polymer poly(3,4-ethylenedioxythiophene). *Nat Mater*, 10(6), 429-433.

- Cançado, L. G., Jorio, A., Ferreira, E. M., Stavale, F., Achete, C., Capaz, R., . . . Ferrari, A. (2011). Quantifying defects in graphene via Raman spectroscopy at different excitation energies. *Nano letters*, *11*(8), 3190-3196.
- Chandrasekhar, S., & Balagurusamy, V. (2002). *Discotic liquid crystals as quasi-one-dimensional electrical conductors*. Paper presented at the Proceedings of the Royal Society of London A: Mathematical, Physical and Engineering Sciences.
- Chen, G. (2011). Theoretical efficiency of solar thermoelectric energy generators. *Journal of Applied Physics*, *109*(10), 104908-104908.
- Chen, K. F., Liou, C. H., Lee, C. H., & Chen, F. R. (2010, 20-25 June 2010). *Development of solid polymeric electrolyte for DSSC device*. Paper presented at the Photovoltaic Specialists Conference (PVSC), 2010 35th IEEE.
- Chu, S., & Majumdar, A. (2012). Opportunities and challenges for a sustainable energy future. *Nature*, *488*(7411), 294-303.
- Cinacchi, G., Colle, R., & Tani, A. (2004). Atomistic molecular dynamics simulation of hexakis (pentyloxy) triphenylene: structure and translational dynamics of its columnar state. *The Journal of Physical Chemistry B*, *108*(23), 7969-7977.
- Dash, S. K., Ranjan, K. S., Alapati, P. R., & Verma, A. L. (1997). Dynamics of phase transitions in a liquid crystalline compound (TBDA) probed by Raman spectroscopy. *Journal of Physics: Condensed Matter*, *9*(37), 7809.
- Datta, R., Said, S., Shahrir, S., Abdullah, N., Sabri, M., Balamurugan, S., . . . Habiba, U. (2015). Ionic liquid entrapment by an electrospun polymer nanofiber matrix as a high conductivity polymer electrolyte. *RSC Advances*, *5*(60), 48217-48223.
- Deng, Y.-G., & Liu, J. (2009). Recent advances in direct solar thermal power generation. *Journal of Renewable and Sustainable Energy*, *1*(5), 052701-052723.
- Deng, Y., Zhu, W., Wang, Y., & Shi, Y. (2013). Enhanced performance of solar-driven photovoltaic-thermoelectric hybrid system in an integrated design. *Solar energy*, *88*, 182-191.
- Donald, D. K. C. M. (1962). *Thermoelectricity: An Introduction to the Principles*: John Wiley & Sons.
- Du, Y., Shen, S. Z., Cai, K., & Casey, P. S. (2012). Research progress on polymer-inorganic thermoelectric nanocomposite materials. *Progress in Polymer Science*, *37*(6), 820-841.
- Dubal, D. P., Ayyad, O., Ruiz, V., & Gomez-Romero, P. (2015). Hybrid energy storage: the merging of battery and supercapacitor chemistries. *Chemical Society Reviews*, *44*(7), 1777-1790.
- Dubey, N., & Leclerc, M. (2011). Conducting polymers: Efficient thermoelectric materials. *Journal of Polymer Science Part B: Polymer Physics*, *49*(7), 467-475.

- Fairbanks, J. W. (2011). *Vehicular thermoelectrics: a new green technology*. Paper presented at the Proceedings of the 2nd Thermoelectrics Applications Workshop.
- Ferrari, A. C., & Robertson, J. (2000). Interpretation of Raman spectra of disordered and amorphous carbon. *Physical Review B*, *61*(20), 14095.
- Francioso, L., De Pascali, C., Farella, I., Martucci, C., Creti, x, . . . Perrone, A. (2010, 1-4 Nov. 2010). *Flexible thermoelectric generator for wearable biometric sensors*. Paper presented at the Sensors, 2010 IEEE.
- Garreau, S., Louarn, G., Buisson, J., Froyer, G., & Lefrant, S. (1999). In situ spectroelectrochemical Raman studies of poly (3, 4-ethylenedioxythiophene)(PEDT). *Macromolecules*, *32*(20), 6807-6812.
- Gascoin, F., & Maignan, A. (2011). Order–disorder transition in AgCrSe₂: a new route to efficient thermoelectrics. *Chemistry of Materials*, *23*(10), 2510-2513.
- Giacoletto, L. J. (1959). Electrical System for Home Conversion and Storage of Solar Energy. *Science*, *130*(3380), 915-916.
- Gorkunov, M. V., Shandryuk, G. A., Shatalova, A. M., Kutergina, I. Y., Merekalov, A. S., Kudryavtsev, Y. V., . . . Osipov, M. A. (2013). Phase separation effects and the nematic-isotropic transition in polymer and low molecular weight liquid crystals doped with nanoparticles. *Soft Matter*, *9*(13), 3578-3588.
- Gottesfeld, S., & Zawodzinski, T. A. (2008). Polymer Electrolyte Fuel Cells *Advances in Electrochemical Science and Engineering* (pp. 195-301): Wiley-VCH Verlag GmbH.
- Green, M. A. (2013). K. Emery, Y. Hishikawa, W. Warta, ED Dunlop. *Solar cell efficiency tables (Version 41) Progress in Photovoltaics: Research and Applications*, *21*, 1-11.
- Günes, S., Neugebauer, H., & Sariciftci, N. S. (2007). Conjugated Polymer-Based Organic Solar Cells. *Chemical Reviews*, *107*(4), 1324-1338.
- Harada, K., Sumino, M., Adachi, C., Tanaka, S., & Miyazaki, K. (2010). Improved thermoelectric performance of organic thin-film elements utilizing a bilayer structure of pentacene and 2,3,5,6-tetrafluoro-7,7,8,8-tetracyanoquinodimethane (F4-TCNQ). *Applied Physics Letters*, *96*(25).
- Haverkate, L. A., Zbiri, M., Johnson, M. R., Carter, E., Kotlewski, A., Picken, S., . . . Kearley, G. J. (2014). Electronic and vibronic properties of a discotic liquid-crystal and its charge transfer complex. *The Journal of chemical physics*, *140*(1), 014903.
- Haverkate, L. A., Zbiri, M., Johnson, M. R., Deme, B., Mulder, F. M., & Kearley, G. J. (2011). Conformation, defects, and dynamics of a discotic liquid crystal and their influence on charge transport. *The Journal of Physical Chemistry B*, *115*(47), 13809-13816.

- Hayashi, K., Shinano, T., Miyazaki, Y., & Kajitani, T. (2011). Fabrication of iodine-doped pentacene thin films for organic thermoelectric devices. *Journal of Applied Physics*, 109(2).
- Hayashi, K., Shinano, T., Miyazaki, Y., & Kajitani, T. (2011). Thermoelectric properties of iodine doped pentacene thin films. *physica status solidi (c)*, 8(2), 592-594.
- Heo, J. H., Im, S. H., Noh, J. H., Mandal, T. N., Lim, C.-S., Chang, J. A., . . . Nazeeruddin, M. K. (2013). Efficient inorganic-organic hybrid heterojunction solar cells containing perovskite compound and polymeric hole conductors. *Nature photonics*, 7(6), 486-491.
- Hewitt, C. A., Kaiser, A. B., Craps, M., Czerw, R., Roth, S., & Carroll, D. L. (2013). Temperature dependent thermoelectric properties of freestanding few layer graphene/polyvinylidene fluoride composite thin films. *Synthetic Metals*, 165(0), 56-59.
- Hicks, L. D., & Dresselhaus, M. S. (1993a). Effect of quantum-well structures on the thermoelectric figure of merit. *Physical Review B*, 47(19), 12727-12731.
- Hicks, L. D., & Dresselhaus, M. S. (1993b). Thermoelectric figure of merit of a one-dimensional conductor. *Physical Review B*, 47(24), 16631-16634.
- Hiroshige, Y., Ookawa, M., & Toshima, N. (2006). High thermoelectric performance of poly(2,5-dimethoxyphenylenevinylene) and its derivatives. *Synthetic Metals*, 156(21-24), 1341-1347.
- Hiroshige, Y., Ookawa, M., & Toshima, N. (2007). Thermoelectric figure-of-merit of iodine-doped copolymer of phenylenevinylene with dialkoxyphenylenevinylene. *Synthetic Metals*, 157(10-12), 467-474.
- Hsu, K. F., Loo, S., Guo, F., Chen, W., Dyck, J. S., Uher, C., . . . Kanatzidis, M. G. (2004). Cubic AgPbmSbTe_{2+m}: bulk thermoelectric materials with high figure of merit. *Science*, 303(5659), 818-821.
- Huang, S., Ruan, X., Zou, J., Fu, X., & Yang, H. (2009). Raman Scattering Characterization of Transparent Thin Film for Thermal Conductivity Measurement. *Journal of Thermophysics and Heat Transfer*, 23(3), 616-621.
- Inayat, S. B., Rader, K. R., & Hussain, M. M. (2012). Nano-materials enabled thermoelectricity from window glasses. *Scientific reports*, 2, 841.
- Inayat, S. B., Rader, K. R., & Hussain, M. M. (2012). Nano-materials Enabled Thermoelectricity from Window Glasses. *Sci. Rep.*, 2.
- Jiao, F., Naderi, A., Zhao, D., Schlueter, J., Shahi, M., Sundstrom, J., . . . Crispin, X. (2017). Ionic thermoelectric paper. *Journal of Materials Chemistry A*, 5(32), 16883-16888.
- Jiyang, W., Liu, H., Hu, X., Jiang, H., Shanrong, Z., Qiang, L., . . . Minhua, J. (2001, 2001). *Progress in skutterudite-based thermoelectric materials*. Paper presented

at the Thermoelectrics, 2001. Proceedings ICT 2001. XX International Conference on Thermoelectrics.

- Kaafarani, B. R. (2010). Discotic liquid crystals for opto-electronic applications. *Chemistry of Materials*, 23(3), 378-396.
- Kaltzoglou, A., Fassler, T., Christensen, M., Johnsen, S., Iversen, B., Presniakov, I., . . . Shevelkov, A. (2008). Effects of the order-disorder phase transition on the physical properties of $A_8\text{Sn}_{44}\text{[square]}_2$ ($A = \text{Rb}, \text{Cs}$). *Journal of Materials Chemistry*, 18(46), 5630-5637.
- Kaneko, H., Ishiguro, T., Takahashi, A., & Tsukamoto, J. (1993). Magnetoresistance and thermoelectric power studies of metal-nonmetal transition in iodine-doped polyacetylene. *Synthetic Metals*, 57(2-3), 4900-4905.
- Khan, A. A., Rughoobur, G., Kamarudin, M. A., Sepe, A., Dolan, J. A., Flewitt, A. J., . . . Wilkinson, T. D. (2016). Homologous binary mixtures and improved hole conduction of self-assembled discotic liquid crystals. *Organic Electronics*, 36, 35-44.
- Kim, G., Shao, L., Zhang, K., & Pipe, K. (2013). Engineered doping of organic semiconductors for enhanced thermoelectric efficiency. *Nature materials*, 12(8), 719-723.
- Kim, G. H., Hwang, D. H., & Woo, S. I. (2012). Thermoelectric properties of nanocomposite thin films prepared with poly (3, 4-ethylenedioxythiophene) poly (styrenesulfonate) and graphene. *Physical Chemistry Chemical Physics*, 14(10), 3530-3536.
- Kim, G. H., Shao, L., Zhang, K., & Pipe, K. P. (2013). Engineered doping of organic semiconductors for enhanced thermoelectric efficiency. *Nat Mater*, 12(8), 719-723.
- Kirkham, M., Majsztrik, P., Skoug, E., Morelli, D., Wang, H., Porter, W. D., . . . Lara-Curzio, E. (2011). High-temperature order/disorder transition in the thermoelectric Cu_3SbSe_3 . *Journal of Materials Research*, 26(15), 2001-2005.
- Kline, R. J., McGehee, M. D., Kadnikova, E. N., Liu, J., & Fréchet, J. M. J. (2003). Controlling the Field-Effect Mobility of Regioregular Polythiophene by Changing the Molecular Weight. *Advanced Materials*, 15(18), 1519-1522.
- Knopfmacher, O., Hammock, M. L., Appleton, A. L., Schwartz, G., Mei, J., Lei, T., . . . Bao, Z. (2014). Highly stable organic polymer field-effect transistor sensor for selective detection in the marine environment. *Nature communications*, 5.
- Kraemer, D., Poudel, B., Feng, H.-P., Caylor, J. C., Yu, B., Yan, X., . . . Muto, A. (2011). High-performance flat-panel solar thermoelectric generators with high thermal concentration. *Nature materials*, 10(7), 532.
- Kraemer, D., Poudel, B., Feng, H.-P., Caylor, J. C., Yu, B., Yan, X., . . . Chen, G. (2011). High-performance flat-panel solar thermoelectric generators with high thermal concentration. *Nat Mater*, 10(7), 532-538.

- Kreouzis, T., Scott, K., Donovan, K., Boden, N., Bushby, R., Lozman, O., & Liu, Q. (2000). Enhanced electronic transport properties in complementary binary discotic liquid crystal systems. *Chemical Physics*, 262(2), 489-497.
- Kroon, R., Mengistie, D. A., Kiefer, D., Hynynen, J., Ryan, J. D., Yu, L., & Müller, C. (2016). Thermoelectric plastics: from design to synthesis, processing and structure–property relationships. *Chemical Society Reviews*, 45(22), 6147-6164.
- Kumar, S. (2016). *Chemistry of discotic liquid crystals: from monomers to polymers*: CRC press.
- Lanzani, G. (2014). Materials for bioelectronics: Organic electronics meets biology. *Nat Mater*, 13(8), 775-776.
- Lee, J.-U., Lee, S., Ryoo, J. H., Kang, S., Kim, T. Y., Kim, P., . . . Cheong, H. (2016). Ising-Type Magnetic Ordering in Atomically Thin FePS₃. *Nano letters*, 16(12), 7433-7438.
- Lee, J.-U., Yoon, D., Kim, H., Lee, S. W., & Cheong, H. (2011). Thermal conductivity of suspended pristine graphene measured by Raman spectroscopy. *Physical Review B*, 83(8), 081419.
- Lemaur, V., da Silva Filho, D. A., Coropceanu, V., Lehmann, M., Geerts, Y., Piris, J., . . . Siebbeles, L. D. A. (2004). Charge transport properties in discotic liquid crystals: a quantum-chemical insight into structure– property relationships. *Journal of the American Chemical Society*, 126(10), 3271-3279.
- Leonov, V., Torfs, T., Vullers, R. J. M., Su, J., & Van Hoof, C. (2010, 14-17 March 2010). *Renewable energy microsystems integrated in maintenance-free wearable and textile-based devices: The capabilities and challenges*. Paper presented at the Industrial Technology (ICIT), 2010 IEEE International Conference on.
- Letheby, H. (1862). XXIX.-On the production of a blue substance by the electrolysis of sulphate of aniline. *Journal of the Chemical Society*, 15(0), 161-163.
- Lévesque, I., Bertrand, P.-O., Blouin, N., Leclerc, M., Zecchin, S., Zotti, G., . . . Tse, J. S. (2007). Synthesis and Thermoelectric Properties of Polycarbazole, Polyindolocarbazole, and Polydiindolocarbazole Derivatives. *Chemistry of Materials*, 19(8), 2128-2138.
- Lévesque, I., Gao, X., Klug, D. D., Tse, J. S., Ratcliffe, C. I., & Leclerc, M. (2005). Highly soluble poly(2,7-carbazolenevinylene) for thermoelectrical applications: From theory to experiment. *Reactive and Functional Polymers*, 65(1–2), 23-36.
- Li, J., Tang, X., Li, H., Yan, Y., & Zhang, Q. (2010). Synthesis and thermoelectric properties of hydrochloric acid-doped polyaniline. *Synthetic Metals*, 160(11–12), 1153-1158.
- Liu, C., Xu, J., Lu, B., Yue, R., & Kong, F. (2012). Simultaneous Increases in Electrical Conductivity and Seebeck Coefficient of PEDOT:PSS Films by Adding Ionic Liquids into a Polymer Solution. *Journal of Electronic Materials*, 41(4), 639-645.

- Lu, Y., Song, Y., & Wang, F. (2013). Thermoelectric properties of graphene nanosheets-modified polyaniline hybrid nanocomposites by an in situ chemical polymerization. *Materials Chemistry and Physics*, 138(1), 238-244.
- Maddison, D. S., Unsworth, J., & Roberts, R. B. (1988). Electrical conductivity and thermoelectric power of polypyrrole with different doping levels. *Synthetic Metals*, 26(1), 99-108.
- Manuel Stephan, A. (2006). Review on gel polymer electrolytes for lithium batteries. *European Polymer Journal*, 42(1), 21-42.
- McEnaney, K., Kraemer, D., Ren, Z., & Chen, G. (2011). Modeling of concentrating solar thermoelectric generators. *Journal of Applied Physics*, 110(7), 074502.
- Meincke, O., Kaempfer, D., Weickmann, H., Friedrich, C., Vathauer, M., & Warth, H. (2004). Mechanical properties and electrical conductivity of carbon-nanotube filled polyamide-6 and its blends with acrylonitrile/butadiene/styrene. *Polymer*, 45(3), 739-748.
- Moriarty, G. P., De, S., King, P. J., Khan, U., Via, M., King, J. A., . . . Grunlan, J. C. (2013). Thermoelectric behavior of organic thin film nanocomposites. *Journal of Polymer Science Part B: Polymer Physics*, 51(2), 119-123.
- Mott, N. (1936). The resistance and thermoelectric properties of the transition metals. *Proceedings of the Royal Society of London. Series A-Mathematical and Physical Sciences*, 156(888), 368-382.
- Mulder, F. M., Stride, J., Picken, S. J., Kouwer, P. H., de Haas, M. P., Siebbeles, L. D., & Kearley, G. J. (2003). Dynamics of a triphenylene discotic molecule, HAT6, in the columnar and isotropic liquid phases. *Journal of the American Chemical Society*, 125(13), 3860-3866.
- Nandi, R., Singh, H. K., Singh, S. K., Singh, B., & Singh, R. K. (2013). Synthesis, characterisation, mesomorphic investigation and temperature-dependent Raman study of a novel calamitic liquid crystal: methyl 4-(4'-n-alkoxybenzylideneamino)benzoate. *Liquid Crystals*, 40(7), 884-899.
- Narducci, D., & Lorenzi, B. (2016). Challenges and Perspectives in Tandem Thermoelectric-Photovoltaic Solar Energy Conversion. *IEEE Transactions on Nanotechnology*, 15(3), 348-355.
- Nolas, G. S., Cohn, J. L., Slack, G. A., & Schujman, S. B. (1998). Semiconducting Ge clathrates: Promising candidates for thermoelectric applications. *Applied Physics Letters*, 73(2), 178-180.
- Onsager, L. (1931). Reciprocal relations in irreversible processes. I. *Physical review*, 37(4), 405.
- Paradiso, J. A., & Starner, T. (2005). Energy Scavenging for Mobile and Wireless Electronics. *IEEE Pervasive Computing*, 4(1), 18-27.

- Park, H., Lee, S. H., Kim, F. S., Choi, H. H., Cheong, I. W., & Kim, J. H. (2014). Enhanced thermoelectric properties of PEDOT: PSS nanofilms by a chemical dedoping process. *Journal of Materials Chemistry A*, 2(18), 6532-6539.
- Park, Y. W., Yoon, C. O., Lee, C. H., Shirakawa, H., Suezaki, Y., & Akagi, K. (1989). Conductivity and thermoelectric power of the newly processed polyacetylene. *Synthetic Metals*, 28(3), D27-D34.
- Paulsson, M., & Datta, S. (2003). Thermoelectric effect in molecular electronics. *Physical Review B*, 67(24), 241403.
- Pidwirny, M. (2006). Atmospheric effects on incoming solar radiation. *Fundamentals of Physical Geography*.
- Poudel, B., Hao, Q., Ma, Y., Lan, Y., Minnich, A., Yu, B., . . . Vashaee, D. (2008). High-thermoelectric performance of nanostructured bismuth antimony telluride bulk alloys. *Science*, 320(5876), 634-638.
- Rey-Lafon, M., & Hemida, A. T. (1990). Vibrational Study of the Phase Transitions in Three Triphenylene Hexa n-Alkanoates. *Molecular Crystals and Liquid Crystals Incorporating Nonlinear Optics*, 178(1), 33-51.
- Ritz, F., & Peterson, C. E. (2004). *Multi-mission radioisotope thermoelectric generator (MMRTG) program overview*. Paper presented at the Aerospace Conference, 2004. Proceedings. 2004 IEEE.
- Russ, B., Gludell, A., Urban, J. J., Chabinye, M. L., & Segalman, R. A. (2016). Organic thermoelectric materials for energy harvesting and temperature control. *Nature Reviews Materials*, 1, 16050.
- Said, S. M., Mahmood, M. S., Daud, M. N., Mohd Sabri, M. F., & Sairi, N. A. (2016). Structure-electronics relations of discotic liquid crystals from a molecular modelling perspective. *Liquid Crystals*, 1-22.
- Sato, K., Yamaura, M., Hagiwara, T., Murata, K., & Tokumoto, M. (1991). Study on the electrical conduction mechanism of polypyrrole films. *Synthetic Metals*, 40(1), 35-48.
- Schilinsky, P., Asawapirom, U., Scherf, U., Biele, M., & Brabec, C. J. (2005). Influence of the Molecular Weight of Poly(3-hexylthiophene) on the Performance of Bulk Heterojunction Solar Cells. *Chemistry of Materials*, 17(8), 2175-2180.
- Schmidt-Mende, L., Fechtenkötter, A., Müllen, K., Moons, E., Friend, R. H., & MacKenzie, J. (2001). Self-organized discotic liquid crystals for high-efficiency organic photovoltaics. *Science*, 293(5532), 1119-1122.
- Schrader, B. (2008). *Infrared and Raman spectroscopy: methods and applications*: John Wiley & Sons.
- Seetawan, T., Seetawan, U., Ratchasin, A., Srichai, S., Singsoog, K., Namhongsa, W., . . . Siridejachai, S. (2012). Analysis of thermoelectric generator by finite element method. *Procedia Engineering*, 32, 1006-1011.

- Sergeyev, S., Pisula, W., & Geerts, Y. H. (2007). Discotic liquid crystals: a new generation of organic semiconductors. *Chemical Society Reviews*, 36(12), 1902-1929.
- Sevik, C., & Cagin, T. (2011). Investigation of thermoelectric properties of chalcogenide semiconductors from first principles. *Journal of Applied Physics*, 109(12), 123712-123715.
- Shirakawa, H., McDiarmid, A., & Heeger, A. (2003). Twenty-five years of conducting polymers. *Chemical Communications*, 2003(1), 1-4.
- Shown, I., Ganguly, A., Chen, L. C., & Chen, K. H. (2015). Conducting polymer-based flexible supercapacitor. *Energy Science & Engineering*, 3(1), 2-26.
- Singh, S. (2000). Phase transitions in liquid crystals. *Physics Reports*, 324(2-4), 107-269.
- Soni, A., Yanyuan, Z., Ligen, Y., Aik, M. K. K., Dresselhaus, M. S., & Xiong, Q. (2012). Enhanced Thermoelectric Properties of Solution Grown Bi₂Te_{3-x}Se_x Nanoplatelet Composites. *Nano letters*, 12(3), 1203-1209.
- Sweet, T. K., Rolley, M., Min, G., Knox, A., Gregory, D., Paul, D., . . . Mullen, P. (2016). *Scalable solar thermoelectrics and photovoltaics (SUNTRAP)*. Paper presented at the AIP Conference Proceedings.
- Thirugnanasambandam, M., Iniyar, S., & Goic, R. (2010). A review of solar thermal technologies. *Renewable and Sustainable Energy Reviews*, 14(1), 312-322.
- Vaughan, G., Heiney, P., McCauley Jr, J., & Smith III, A. B. (1992). Conductivity and structure of a liquid-crystalline organic conductor. *Physical Review B*, 46(5), 2787.
- Venkatasubramanian, R., Siivola, E., Colpitts, T., & O'Quinn, B. (2001). Thin-film thermoelectric devices with high room-temperature figures of merit. *Nature*, 413, 597.
- Vikram, K., Srivastava, S. K., Ojha, A. K., Schlücker, S., Kiefer, W., & Singh, R. K. (2009). Dynamics and mechanism of the Crystal II \rightarrow smecticG phase transition in TB7A by a temperature-dependent micro-Raman study and DFT calculations. *Journal of Raman Spectroscopy*, 40(8), 881-886.
- Vining, C. B. (2009). An inconvenient truth about thermoelectrics. *Nature materials*, 8(2), 83.
- Vining, C. B., McCormack, J. A., Zoltan, A., & Zoltan, L. D. (1991). A promising new thermoelectric material: Ruthenium silicide. *AIP Conference Proceedings*, 217(1), 458-463.
- Wang, L., Wang, D., Zhu, G., Li, J., & Pan, F. (2011). Thermoelectric properties of conducting polyaniline/graphite composites. *Materials letters*, 65(7), 1086-1088.
- Wang, M., Pan, X., Fang, X., Guo, L., Zhang, C., Huang, Y., . . . Dai, S. (2011). Liquid crystal based electrolyte with light trapping scheme for enhancing photovoltaic

- performance of quasi-solid-state dye-sensitized solar cells. *Journal of Power Sources*, 196(13), 5784-5791.
- Wang, Z., Leonov, V., Fiorini, P., & Van Hoof, C. (2009). Realization of a wearable miniaturized thermoelectric generator for human body applications. *Sensors and Actuators A: Physical*, 156(1), 95-102.
- Weber, J., Potje-Kamloth, K., Haase, F., Detemple, P., Völklein, F., & Doll, T. (2006). Coin-size coiled-up polymer foil thermoelectric power generator for wearable electronics. *Sensors and Actuators A: Physical*, 132(1), 325-330.
- Xia, Y., Sun, K., & Ouyang, J. (2012). Solution-Processed Metallic Conducting Polymer Films as Transparent Electrode of Optoelectronic Devices. *Advanced Materials*, 24(18), 2436-2440.
- Yang, T., Xiao, J., Li, P., Zhai, P., & Zhang, Q. (2011). Simulation and Optimization for System Integration of a Solar Thermoelectric Device. *Journal of Electronic Materials*, 40(5), 967-973.
- Yoon, C. O., Reghu, M., Moses, D., Cao, Y., & Heeger, A. J. (1995). Thermoelectric power of doped polyaniline near the metal-insulator transition. *Synthetic Metals*, 69(1-3), 273-274.
- Yu, C., Kim, Y. S., Kim, D., & Grunlan, J. C. (2008). Thermoelectric Behavior of Segregated-Network Polymer Nanocomposites. *Nano letters*, 8(12), 4428-4432.
- Yue, R., Chen, S., Liu, C., Lu, B., Xu, J., Wang, J., & Liu, G. (2012). Synthesis, characterization, and thermoelectric properties of a conducting copolymer of 1,12-bis(carbazolyl)dodecane and thieno[3,2-]thiophene. *Journal of Solid State Electrochemistry*, 16(1), 117-126.
- Zhang, K., Zhang, Y., & Wang, S. (2013). Enhancing thermoelectric properties of organic composites through hierarchical nanostructures. *Scientific reports*, 3, 3448.
- Zhao, D., Qian, X., Gu, X., Jajja, S. A., & Yang, R. (2016). Measurement techniques for thermal conductivity and interfacial thermal conductance of bulk and thin film materials. *Journal of Electronic Packaging*, 138(4), 040802.
- Zhao, J., Jiang, J.-W., Wei, N., Zhang, Y., & Rabczuk, T. (2013). Thermal conductivity dependence on chain length in amorphous polymers. *Journal of Applied Physics*, 113(18), 184304-184304.
- Zhao, J., Nagao, S., & Zhang, Z. (2010). Thermomechanical properties dependence on chain length in bulk polyethylene: Coarse-grained molecular dynamics simulations. *Journal of Materials Research*, 25(03), 537-544.
- Zhao, L.-D., Lo, S.-H., Zhang, Y., Sun, H., Tan, G., Uher, C., . . . Kanatzidis, M. G. (2014). Ultralow thermal conductivity and high thermoelectric figure of merit in SnSe crystals. *Nature*, 508(7496), 373-377.

University of Malaya

LIST OF PUBLICATIONS AND PAPERS PRESENTED

1. Datta, R., Said, S., Sahamir, S., Karim, M., Sabri, M., Nakajo, T., . . . Miyazaki, Y. (2014). Thermoelectric Potential of Polymer-Scaffolded Ionic Liquid Membranes. *Journal of Electronic Materials*, 43(6), 1585-1589.
2. Datta, R., Said, S., Shahrir, S., Abdullah, N., Sabri, M., Balamurugan, S., . . . Habiba, U. (2015). Ionic liquid entrapment by an electrospun polymer nanofiber matrix as a high conductivity polymer electrolyte. *RSC Advances*, 5(60), 48217-48223.
3. Kamarudin, M. A., Sahamir, S. R., Datta, R. S., Long, B. D., Sabri, M., Faizul, M., & Mohd Said, S. (2013). A review on the fabrication of polymer-based thermoelectric materials and fabrication methods. *The Scientific World Journal*, 2013.
4. Sahamir, S. R., Said, S. M., Mohd Sabri, M. F., Mahmood, M. S., Bin Kamarudin, M. A., & Moutanabbir, O. (2017). Studies on relation between columnar order and electrical conductivity in HAT6 discotic liquid crystals using temperature-dependent Raman spectroscopy and DFT calculations. *Liquid Crystals*, 1-14.
5. Said, S. M., Sahamir, S. R., Sabri, M. F. M., Kamarudin, M. A., Hayashi, K., Zulkifli, A. Z. S., . . . Miyazaki, Y. (2017). Polymer electrolyte liquid crystal mixtures as phase-dependent thermoelectric materials. *Molecular Crystals and Liquid Crystals*, 642(1), 9-17.